SINGLE MOLECULE FLUORESCENCE SPECTROSCOPY AT AMBIENT TEMPERATURE:

DESIGN AND APPLICATION OF A TIME-RESOLVED CONFOCAL MICROSCOPE WITH SINGLE-MOLECULE SENSITIVITY

DISSERTATION

zur Erlangung des Doktorgrades

der naturwissenschaftlichen Fakultät IV

- Chemie und Pharmazie –

der Universität Regensburg

vorgelegt von

Diplom-Physiker Martin Böhmer

aus Düsseldorf

im Dezember 2001

1. Gutachter: Priv.-Doz. Dr. J. Enderlein

2. Gutachter: Prof. Dr. B. Dick

Die Arbeit wurde angeleitet von: Priv.-Doz. Dr. J. Enderlein

Promotionsgesuch eingereicht am: 17.12.2001

Pfüfungsausschuß:

Vorsitzender	
1. Prüfer	Priv.-Doz. Dr. J. Enderlein
2. Prüfer	Prof. Dr. B. Dick
3. Prüfer	Prof. Dr. H. Krienke

Das Kolloquium fand statt am: 04.02.2002

Contents

1. Introduction

1.1 Single molecule detection at ambient temperatures

The sensitive detection and spectroscopy of minute amounts of substances in solution and on surfaces is an important technique in many fields of fundamental research as well as for chemo- and bioanalytical applications. In recent years, technical improvements in photodetector sensitivity, microscope objective optics, and laser light sources made even the detection of single molecules (SMD) possible [1-5]. For achieving this goal, two detection techniques played an important role: confocal laser scanning microscopy (CLSM) [6-9] and wide-field microscopy with advanced high-sensitive CCD-cameras (WFM) [10-12]. Whereas the latter approach to SMD found widespread applications in many biological studies, CLSM is the method of choice for spectroscopic investigations. Although in WFM, special detection set-ups can provide several spectral detection channels (e.g. for monitoring emission polarization or different emission colors) [13-14], the spectroscopic abilities of WFM are limited. More importantly, due to the rather long detection and read-out times of CCD-cameras, any temporal processes in the sub-millisecond time range are virtually inaccessible. Especially, this is true for measuring the fluorescence lifetime of the detected molecules, itself an important spectroscopic parameter, which can also be used to discriminate between different molecular species. In contrast to WFM, CLSM employs photomultiplier tubes or single-photon avalanche diodes with sufficiently high temporal resolution for fluorescence detection, enabling the monitoring of temporal processes down to the picosecond level. Thus, CLSM is perfectly suited for ultrasensitive lifetime imaging on surfaces. Another potential advantage of CLSM over WFM is its ultimately small detection volume due to confocal imaging, providing a much better signal-to-noise ratio than achievable in WFM. This is important in applications with high background fluorescence as often encountered in studies on biological samples.

Historically, confocal SMD was developed out of fluorescence correlation spectroscopy (FCS, see e.g. [15]). In FCS, the temporal fluctuations of the measured fluorescence signal instead of its average value are exploited for analysis. These fluctuations occur when molecules diffuse in and out of the detection volume which is restricted by the extension of the laser beam focus and the depth of resolution of the confocal detection. Significant fluctuation

amplitudes occur at sufficiently low analyte concentrations, when the number of molecules simultaneously present within the detection volume is small (≤ 10). The first SMD with such a set-up was reported by Rigler et al. [16]. Afterwards, this experimental approach became quite popular due to its relative simplicity. In most experiments using confocal SMD, the diffusion coefficient or the concentration of the fluorescing species is determined. However, the method was also successfully applied for gaining insight into molecular photophysics [17], to monitor conformational changes [18,19], and chemical reactions [20,21,22,23]. An extensive study of Förster resonance energy transfer (FRET) between dyes attached to short DNA fragments was the topic of Ref.[24].

Recently, several publications have dealt with the application of the technique to *in vivo* studies of living cells [25,26], an application that will certainly gain significant importance in the future.

Applications of single molecule sensitive FCS to the important and rapidly evolving field of high-throughput screening are discussed in Refs.[27], and for medical diagnostics in Ref.[28]. A promising variation on this theme is the development of advanced data analysis methods, the so-called fluorescence intensity distribution analysis (FIDA) [29,30] and fluorescence intensity multiple distribution analysis (FIMDA) [31]. These methods allow for the quantification of the fluorescence brightness of molecular species (FIDA, FIMDA), besides assessing their diffusion coefficients (FCS, FIMDA). This information can then be used for classifying and quantifying different sorts of molecules.

One of the latest developments in SMD is the application of a CLSM for imaging surfaces or biological samples with single molecule sensitivity. The set-up is similar to confocal SMD, but now the laser focus is two-dimensionally scanned over a surface for obtaining an image. The first report of detecting single molecules on a surface with a CLSM was given in Ref.[6]. The method was further elaborated and applied to the study of single molecule photophysics (polarization, FRET) [32,33]. First time-resolved measurements with time-correlated single-photon counting (TCSPC) [39] were reported in Ref.[34], where the lifetime information was used to deduce single molecule orientations with respect to the sample surface. In addition the employed compact electronics for time-correlated single-photon counting can be used for photon antibunching experiments. The first photon antibunching experiments on single molecules were performed in Refs.[35,36]. Due to the ability of the CLSM to scan a sample and to locate the position of a single molecule, it can be used to study the photophysics of selected single molecules [37].

A special modification of the CLSM technique is the excitation of fluorescence by two-photon excitation. Due to the quadratic dependence of the excitation rate on the local laser

intensity, the region of effective fluorescence excitation is confined to a very small volume, thus making the usage of a confocal aperture within the detection channel superfluous. A fast CLSM with two-photon excitation and polarization sensitivity is described in Ref.[38].

The central goal of the work described in this thesis was the development of a time-resolved CLSM for ultrasensitive fluorescence detection in solution and fluorescence lifetime-imaging on surfaces, and its application to new and original spectroscopic studies on a single molecule level. In order to realize a CLSM capable of SMD and with high temporal resolution (down to picoseconds) and a fast data acquisition (limited only by the photophysics of the detected molecules), several components of the system had to be developed and built completely new. The realized system is a multichannel fluorescence detection and spectroscopy CLSM, capable of monitoring single molecules in liquids and on surfaces, capable of performing emission and/or polarization spectroscopy, time-resolved spectroscopy with picosecond temporal resolution, and FCS with sub-microsecond temporal resolution. Moreover, it allows ultrafast scanning of surfaces thus allowing wavelength, polarization and lifetime imaging of immobilized molecules and samples (e.g. cells, tissue). With the help of this advanced measurement system, several novel concepts of SMD were experimentally realized and tested (i.a. *ab initio* FCS, TCSPC-FCS, 3d-polarization spectroscopy, see subsequent chapters).

The thesis is organized as follows:

Chapter 2 describes in detail the individual components of the built measurement system as well as its optical design. The system employs compact electronics for TCSPC, allowing for measuring fluorescence lifetime with 40 ps temporal resolution, and for continuously recording photon arrival times with 100 ns resolution. Applying an asynchronous data acquisition concept, minimum data load and maximum versatility in spectroscopic data evaluation is achieved.

In chapter 3, advanced concepts of single molecule spectroscopy in solution are introduced. FCS is an important measurement technique for obtaining information about diffusion coefficients and concentrations of fluorescent analyte molecules in solution. Usually, when evaluating measured fluorescence correlation data, a simplified model is applied which rests on the rather unrealistic assumption of an ellipsoidal detection volume. It is shown that there is no principal difficulty in correctly modeling FCS curves, when exact wave optics calculations of the excitation and detection optics are applied. The presented method of fluorescence correla-

tion data evaluation bears the great potential of providing a way for an *absolute* determination of diffusion coefficients *and* analyte concentrations, without involving any empirical fit parameter or *ad hoc* assumptions.

There is growing demand in the use of fluorescent probes for the detection of biological compounds like proteins. Therefore, the second part of the chapter deals with the photophysical characterization of new flourescent labels belonging to the class of cyanine dyes or to the closely related class of squaraine dyes.

Finally, by combining TCSPC with FCS, a new method for performing TCSPC-FCS measurements on mixtures of fluorescent species like cyanine and squaraine dyes is introduced. It uses time-resolved fluorescence detection for separating the different FCS contributions of the different species. This allows for simultaneously and independently monitoring the diffusion of several molecular species in one sample, or for performing multi-label cross-correlation measurements. In this thesis, the theoretical basis of this new method is introduced, and experimental results are presented.

In chapter 4, the imaging capability of the system is demonstrated on imaging single molecules that are immobilized on glass substrates. In particular, intensity, polarization, and lifetime images of single molecules are presented. It is shown how, by using an advanced illumination technique, three-dimensional polarization measurements of single fluorescent molecules with fixed excitation/emission dipoles can be performed. At the end of chapter 4, an outlook towards the application of the built SMD-CLSM to *in vivo* studies of living cells is given.

The final chapter 5 summarizes the main results and conclusions of this thesis.

1.2 References

1. M.D. Barnes, W.B. Whitten, and J.M. Ramsey, *Anal. Chem.* **67**(1995) 418A.
2. R.A. Keller, W.P. Ambrose, P.M. Goodwin, J.H. Jett, J.C. Martin, and M. Wu, *Appl. Spectr.* **50** (1996) 12A.
3. P.M. Goodwin, W.P. Ambrose, and R.A. Keller, *Acc. Chem. Res.* **29**, 607 (1996).
4. S. Weiss, *Science* **283** (1999) 1676.
5. J. Enderlein, W.P. Ambrose, P.M. Goodwin, and R.A. Keller, " Fluorescence detection of single molecules applicable to small volume assays" in*Microsystem technology: A powerful tool for biomolecular studies*; Eds.: M. Köhler, T. Mejevaia, H.P. Saluz (Birkhäuser, Basel, 1999) 311.
6. J. Dapprich, Ü. Mets, W. Simm, M. Eigen, and R. Rigler, *Exp. Tech. Phys.* **41** (1995) 259-64.
7. T. Ha, D.S. Chemla, T. Enderle, and S. Weiss, *Bioimaging* **5** (1997) 99.
8. T. Ha, T. Enderle, D.S. Chemla, P.R. Selvin, and S. Weiss, *Phys. Rev. Lett.* **77** (1996) 3979.
9. P. Tinnefeld, V. Buschmann, D.P. Herten, K.T. Han, and M. Sauer, *Single Molecules* **1** (2000) 215.
10. M. Ishikawa, K. Hirano, T. Hayakawa, S. Hosoi, and S. Brenner, *Japanese J. Appl. Phys.***33(Pt.1)** (1994) 1571.
11. T. Funatsu, Y. Harada, M. Tokunaga, K. Saito, and T. Yanagida, *Nature* **374** (1995) 555.
12. T. Schmidt, G.J. Schütz, W. Baumgartner, H.J. Gruber, and H. Schindler, *Proc. Nat. Acad. Sci. USA* **93** (1996) 2926.
13. G.S. Harms, M. Sonnleitner, G.J. Schütz, H.J. Gruber, T. Schmidt *Biophys. J.* **77** (1999) 2864.
14. L. Cognet, G.S. Harms, G.A. Blab, P.H.M. Lommerse, T. Schmidt *Appl. Phys. Lett.* **77** (2000) 4052.
15. N.L. Thompson *Fluorescence correlation spectroscopy* in: Topics in Fluorescence Spectroscopy vol. 1; Ed.: J.R. Lakowicz; Plenum Press, New York **1991**, 337-78.
16. R. Rigler; J. Widengren *Bioscience* **3** (1990) 180-3.
17. S.A. Soper; B.L. Legendre; J.P. Huang; *Chem. Phys. Lett.* **237** (1995) 339-345.
18. L. Edman; Ü. Mets; R. Rigler; *Exp. Tech. Phys.* **45** (1995) 157-63.
19. C. Eggeling; J.R. Fries; L. Brand; R. Günther; C.A.M. Seidel; *Proc. Natl. Acad. Sci. USA* **95** (1998) 1556-61.

20. J.J. Laclair *J. Am. Chem. Soc.* **119** (1997) 7676-7684.
21. M. Sauer; K.H. Drexhage; U. Lieberwirth; R. Müller; S. Nord; C. Zander *Chem. Phys. Lett.* **284** (1998) 153-63.
22. J. Widengren; R. Rigler *Cellular Mol. Biol.* **44** (1998) 857-79.
23. D.C. Daniel; M. Thompson; N.W. Woodbury *J. Phys. Chem. B* **104** (2000) 1382-90.
24. L. Ying; M.I. Wallace; S. Balasubramanian; D. Klenerman *J. Phys. Chem. B* **104** (2000) 5171-8.
25. P. Schwille; J. Korlach; W.W. Webb *Cytometry* **36** (1999) 176-82.
26. P. Schwille; U. Haupts; S. Maiti; W.W. Webb *Biophys. J.* **77** (1999) 2251-65.
27. M. Eigen; R. Rigler *Proc. Natl. Acad. Sci. USA* **91** (1994) 5740-7.
28. M. Sauer; C. Zander; R. Müller; B. Ullrich; K.H. Drexhage; S. Kaul; J. Wolfrum *Appl. Phys. B* **65**(1997) 427-431.
29. J.D. Müller; Y. Chen; E. Gratton *Biophys. J.* **78** (2000) 474-86.
30. P. Kask, K. Palo, D. Ullmann and K. Gall, *Proc. Natl. Acad. Sci. USA*, **96** (November 23, 1999) 13756-61.
31. K. Palo; Ü. Mets; S. Jager; P. Kask; K. Gall *Biophys. J.* **79** (2000) 2858-66.
32. T. Ha; T. Enderle; D.F. Ogletree; D.S. Chemla; P.R. Selvin; S. Weiss *Proc. Natl. Acad. Sci. USA* **93** (1996) 6264-8.
33. T. Ha; T. Enderle; D.S. Chemla; P.R. Selvin; S. Weiss *Phys. Rev. Lett.* **77** (1996) 3979-82.
34. J.J. Macklin; J.K. Trautman; T.D. Harris; L.E. Brus *Science* **272** (1996) 255-8.
35. W.P. Ambrose; P.M. Goodwin; J. Enderlein; D.J. Semin; J.C. Martin; R.A. Keller *Chem. Phys. Lett.* **269** (1997) 365-70.
36. L. Fleury; J.-M. Segura; G. Zumofen; B. Hecht; U.P. Wild *Phys. Rev. Lett.* **84** (2000) 1148-51.
37. W.E. Moerner *Science* **277** (1997) 1059-1060.
38. R.A. Farrer; M.J.R. Previte; C.E. Olson; L.A. Peyser; J.T. Fourkas; P.T.C. So *Opt. Lett.* **24** (1999) 1832-4.
39. D. V. O'Connor and D. Phillips *Time-correlated single photon counting* (Academic Press, London, 1984).

2. Design of a Time-Resolved Confocal Microscope

For many applications, a basic setup of a confocal scanning system is sufficient for quantifying and imaging the fluorescence from singly labeled molecules, fluorescent beads or fluorescent stained samples. Such a system includes a continuous wave (cw) laser source, mirrors, lenses, excitation and emission filters, a confocal aperture, a single-photon sensitive photoelectron detector, data acquisition electronics, and a high precision scanning stage. The major challenge is synchronizing and adjusting all parts.

In recent years, single-molecule fluorescence lifetime analysis has attracted increasing attention [1-5], providing a powerful additional feature for distinguishing and identifying molecules of interest. Fluorescence lifetime measurements require that the system has to be further equipped with a pulsed laser source and a TCSPC electronics. If a high-power pulsed laser source is available, multiphoton-excitation can also be applied.
In any case, a single-molecule sensitive CLSM system needs high mechanical stability, a sufficient stable laser source with a beam of constant intensity and profile, and a photoelectron detector with data acquisition electronics tuned to the time scale of the sample under study.
The next subsections give a step-by step description of all parts of a complete CLSM-SMD set-up.

2.1 Conventional microscope

The first microscope was probably invented by the spectacle maker Zacharias Janssen of Middelburg in 1590. In 1610 also Galileo announced his invention of a microscope. A microscope consists of an objective that makes a magnified image of the object at an image distance L (known as tube length, which is today standardized at 160 mm). This intermediate image is magnified further by an eyepiece. Ernst Abbe introduced the concept of the numerical aperture (NA) of an objective. He showed that the lateral image resolution depends both on the wavelength and the NA of the objective and condenser [6]:

$$d = 1.22\lambda / (NA_{obj} + NA_{cond}) \qquad (2.1)$$

with: $NA = n\sin(\theta)$, d [m] being the minimal lateral distance between two object points that can be resolved in the image (Rayleigh criterion), λ [m] the wavelength of the light, n the refractive index of the medium between object and objective and θ the half of the maximum acceptance angle of the objective. The axial resolution can be estimated for low numerical apertures and equal NA of objective and condensor by the following equation [7]:

$$\text{axial resolution} = 2\lambda/(NA)^2 \tag{2.2}$$

2.2 Confocal microscope

In order to detect and to study individual fluorescent molecules, the collection of the single molecule's fluorescence emission has to be maximized while efficiently rejecting any background signal. The most efficient way of achieving that is to use high-quality optical filters, and to minimize the detection volume as much as possible.

A very convenient way of minimizing the detection volume is confocal imaging. In confocal imaging, the sample is illuminated by focusing a laser beam into a diffraction limited spot with an appropriate objective, and fluorescence light collection is done though the same objective (epi-fluorescence setup). Before detecting the collected light with a photoelectric detector, it is send through a so called confocal circular aperture. The diffraction limited focusing of the excitation laser assures minimum lateral extension of the detection volume (perpendicular to the optical axis), whereas the confocal aperture minimizes its axial extension (along the optical axis) by rejecting any light emerging from above or below the in-focus plane (see Fig.2 A,B). This results in a detection volume of roughly 0.5 μm diameter and 2 μm elongation.

The minimal lateral distance between two points which just can be distinguished according to the Rayleigh criterion is given by [8]:

$$d_{\text{lateral}} = 0.56\lambda/NA \tag{2.3}$$

which is by 8 % better than in a conventional microscope. The depth of resolution (FWHM) for a fluorescent plane reflector and an infinitesimal small pinhole is given by [8]:

$$d_{\text{axial}} = \frac{0.67\lambda}{n(1-\cos\theta)} \tag{2.4}$$

where θ is again the half of the maximum acceptance angle of the objective. In practical applications the depth of resolution will be worse due to the finite size of actual pinholes. For studying molecules that are immobilized on a surface, the focused laser has to be scanned over the surface, either to record the fluorescence signal along single lines on the surface, or to record a complete fluorescence image of the surface by scanning in two directions. Confocal imaging and scanning constitute the basic ingredients of a CLSM. Scanning can also be extended into the third spatial dimension by scanning planes at different locations along the optical axis (so called *z*-scanning), resulting in a thee-dimensional fluorescence image of a sample (e.g. a dye-tagged cell, or a transparent substrate with embedded fluorescent molecules).

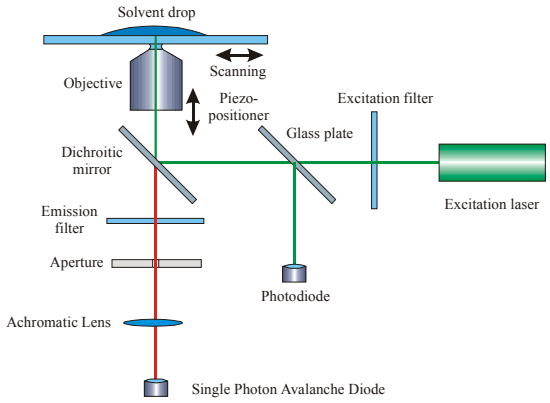

Fig. 1: General scheme of a CLSM-SMD setup: supported with the appropriate filter set (636DF9, e.g. 636+/-4.5 nm, for excitation, 650DRLP as the dichroic mirror and two 670DF40 emission filters, Omega Optical Inc.) for fluorescence microscopy observations in the red spectral region employing a diode laser as the excitation source (HDL 800, 635 nm, PicoQuant GmbH, Berlin) and a Single-Photon Avalanche Diode (SPCM-AQR-14, Perkin Elmer Lifescience, Canada) as the detection unit.

The basic scheme of the simplest CLSM-SMD set-up is depicted in Fig.1. The light of an excitation laser passes through an excitation filter (and possibly a polarizer and/or λ/4-plate), and is, after reflection at a dichroic mirror, send into a microscope objective with high NA. The light emission generated within the specimen is collected by the same objective and focused, after passing the dichroic mirror, onto the confocal aperture. Behind the aperture, the light is refocused onto a single-photon sensitive point detector. Sample scanning can be performed in several ways, in Fig.1 it is realized by a xy-piezo stage. *Z*-scanning is done by moving the objective with a piezo-actuator along the optical axis.

Compared with SMD by highly sensitive CCD systems, the CLSM offers several advantages. Firstly, due to the small detection volume, the CLSM has an exceptionally high signal-to-background ratio. Secondly, uniform scanning provided, the CLSM assures a homogeneous sample illumination, which may be a challenge in conventional WFM. Thirdly, the CLSM uses single point detectors for light detection, thus offering the possibility to study extremely fast processes down to the picosecond time scale. This is especially interesting for sensitive fluorescence lifetime imaging, where the florescence decay time characteristics are measured for every point on the scanned surface. Also, the splitting of the detected light into several channels for measuring other spectral characteristics such as polarization or emission wavelength is straightforward in CLSM. The main limitation of CLSM, when compared with CCD imaging, is the limited scan speed with which an image can be recorded. This scan speed is mainly determined by the maximum number of photons per time interval that can be extracted from a single molecule (optical saturation limit). Typically, if one assumes that a single molecule occupies an image area of ca. 1 μm^2 (determined by the diameter of the exciting laser focus), and that a realistic detectable photon count intensity of a single molecule's fluorescence is of the order of 1 Mcps, an imaging speed of 0.1 μm^2/msec will yield ca. 100 photons per detected molecule. This is a reasonable number for detecting and studying individual molecules. Thus, for imaging an area of e.g. $100 \times 100 \mu m^2$, it takes a minimum of 1 sec, by ca. three magnitudes of order longer than what is achievable with fast CCD systems [9].

2.3 Excitation sources

The choice of the laser source depends on the required excitation wavelengths, the necessary laser power, laser beam stability, and beam mode quality. One has also to consider practical considerations such as necessary power supply and cooling. For example, older lamp-pumped laser systems require a three-phase high voltage electrical supply. They are usually cooled by water or air circulation, which may generate vibrations in the optical setup. The newly available diode laser packages are an interesting and remarkably low-cost alternative.
When selecting the excitation wavelength, one has to take into account that scattering background and auto-fluorescence significantly decrease with longer wavelengths, and that biological tissue is more transparent at longer wavelengths. Therefore, using dyes that absorb in the red or near-infrared wavelength region results in much better signal-to-noise ratios than when using dyes in the blue spectral region, see e.g. [10-13]. To achieve diffraction limited

focusing, the excitation laser should provide a noise-free and intensity-stable beam with perfect Gaussian intensity profile (TEM_{00} mode).

The applied laser system is the low-power but inexpensive single-mode diode laser. In a diode laser, a forward-biased *pn*-junction emits photons into a planar cavity. The photons are confined within the cavity by a planar wave-guide. The generated emission has an elliptical divergence with an astigmatism (within different axial planes, focal points are at different positions), but can be circularized and collimated with an aspheric lens and prism optics. Complete cw-diode-laser packages with a single-mode collimated laser beam and integrated thermoelectric cooling are readily available (e.g. APM modules form PTI, Inc.). They show stable performance and long lifetime.

Additionally, gain switched diode lasers (e.g. PDL 800, PicoQuant GmbH) can deliver pulses of duration down to 50 ps full width at half maximum (FWHM) at a repetition rate of up to 100 MHz. Their output power of ca. 1 mW cw is totally sufficient for CLSM-SMD measurements. The currently available pulsed diode lasers deliver light at 635 nm (GaAs diodes) and above, and at around 400 nm (blue GaN diodes). These diode systems are ideally suited for TCSPC applications.

2.4 Excitation filter

Especially for diode lasers, spectral filtering of the excitation is crucial due to the rather broad spectral width of the laser light. As excitation filters, high-quality interference bandpass filters are preferable. Compared to simple color glass filters, interference filters have much higher fidelity in their rejection and transmission characteristics, and much sharper transmission band edges. The main characteristics of a bandpass filter are its center wavelength, maximum transmission, and bandwidth (usually given by the FWHM in nanometers). Special excitation filters with a FWHM bandwidth of 3 nm or even smaller are available today. The excitation filters are blocking light from the UV to the near IR, keeping unwanted light out of the optical system and preventing unwanted heating of the specimen.

In order to provide perfect blocking of light outside the pass band, most interference filters incorporate absorptive elements as well as dielectric layers. Usually, an interference filter should be placed with the most reflective, metallic looking surface towards the light source. The other surface can be distinguished by its more colored or opaque appearance. This orientation reduces the thermal stress on the absorbing media of the filter. Typically, filters show an arrow sign at their edge indicating the direction of the light path. However, spectral per-

formance is unaffected by filter orientation as long as the light rays pass perpendicularly to the surface and filter heating is avoided. The performance of an interference filter changes with temperature due to the expansion and contraction of the coating materials, and depends upon the design of the coating. Most manufacturers design their filters for an optimal operating temperature of 20° C, and recommend an operating temperature range between - 60° C and + 60° C. Within the spectral band between 600 and 700 nm, a typical value of the thermal spectral shift coefficient of a dielectric coating is 0.019 nm per 1° C.

Interference filters have a finite lifetime. Perhaps the most severe cause of filter deterioration is humidity, which affects the coating. Manufacturers take care to seal the filter edges with moisture-rejecting layers. However, for extending the filters' lifetime, filters should be stored in an environment with low to moderate relative humidity. Additionally, interference filters, particularly those with narrow bands, are subject to a slight blue shift with increasing age. The transmission and reflectance characteristics of filters can be measured easily by using a spectrophotometer and a spectrofluorometer. The details can be found in Ref.[14]. However, many spectrophotometers do not reliably measure transmission values below 1 %. In this case, it is impossible to be certain whether a filter blocks indeed 0.01% outside its passband. This problem can be solved if a laser power-meter is available. Using, for example, the red line of a HeNe laser or a diode laser with an output of a few mW, and a power-meter which can detect a few tenths of a microwatt, the transmission of a filter can be determined below 0.01 % at the HeNe or diode laser wavelengths.

2.5 Dichroic mirror and emission filter

While most filters are used at normal incidence of light, it is possible to design and use an interference-coated substrate at angles of incidence as great as 50°. In the normal-incidence configuration, it is only possible to isolate the transmitted radiation. However, if a filter is tilted away from the axis of the incoming light, the reflected as well as the transmitted light can be used. Such a filter then works as a dichroic mirror, reflecting at one wavelength and transmitting at another wavelength.

In a CLSM-setup, a dichroic mirror is used for reflecting the excitation laser light into the optical path of the microscope. The spectral characteristics of the mirror are chosen in such a way that it reflects at the excitation wavelength and transmits the fluorescence wavelengths. In most fluorescence applications, dichroic mirrors are used in combination with conventional dye-specific fluorescence bandpass filters or equivalent longpass and shortpass filters. A typi-

cal filter combination includes a bandpass excitation filter, a bandpass emission filter, and a dichroic mirror. Longpass, shortpass, and bandpass dichroics are available at all wavelengths. Sometimes a wide-bandpass dichroic filter can be used as a longpass or shortpass filter. The ideal longpass or shortpass dichroic mirror will simultaneously exhibit all three of the following spectral characteristics: A very sharp transmission band edge, an infinite region of transmission, and a wide region of reflection. In reality, the reflectivity typically reaches values larger than 98 %, and transmission typically exceeds 85 %. Custom dichroic mirrors are available for a broad region of the visible spectrum from several companies (e.g. Chroma Technology Corp., or Omega Optical Inc., both Brattleborro, VT) and can be placed directly into a conventional fluorescence dichroic holder. Because the dichroics show some variability in their performance, it is useful to obtain the reflectance and transmission characteristics for the actual dichroic that is purchased. In order to avoid losses of the exciting laser light, the wavelength of maximum reflectance should match the main wavelength of the laser light. More important, the wavelength dependency of the dichroic transmission should be carefully taken into account to avoid losses of the transmitted fluorescence signals.
Standard stock dichroic mirrors are designed for a fixed angle of incidence. Usually, the dichroic mirror is oriented in such a way that the reflected light comes off by an angle of 90° with respect to the incident light. In the case of linearly polarized light, the reflectance values of dielectric coatings can vary significantly with changing polarization. Manufacturers usually provide *p*-polarization and *s*- polarization reflectivity spectra. For most applications, it is desirable that the dichroic's reflectivity does not depend on polarization. Thus, most manufacturers have developed special coating designs for minimizing polarization effects.

2.6 Microscope objective and tube lens

A standard objective lens forms an inverted image at the intermediate image plane of the microscope. The distance of the intermediate image plane from the back focal plane of the objective is called the tube length. To determine the resolution of a microscope, the numerical aperture (NA) of the objective must be known. The NA can be determined via the relation $NA = n \sin\theta$ from the refractive index n of the medium between lens and sample, and the half-angle θ subtended by the lens at its focus. The numerical aperture is a measure of both the optical resolution and the light collecting ability of the lens. It is usually specified by the manufacturer and engraved along with the magnification on the objective's body.

The concept of the numerical aperture is closely related to the concept of the focal ratio or *f*-number. In the case of a simple lens, the *f*-number is the ratio of the lens' focal length to its clear aperture $\varnothing$ (effective diameter) *f*-number $= f/\varnothing$. The *f*-number of a simple lens equals the angle of the light cone that exits the lens when illuminated with collimated light. The connection between *f*-number and NA is given by $\mathrm{NA} = \sin\theta = \varnothing/2f$.

To understand the importance of the NA, consider how it relates to magnification. The numerical aperture on the object side (NA) and that on the image side (NA') are related by

$$m = \frac{\sin\theta}{\sin\theta'} = \frac{\mathrm{NA}}{\mathrm{NA}'}, \tag{2.5}$$

where *m* is the magnification of the system. Thus, *m* is equal to the ratio of the numerical apertures on the object and image side. This is a very general result, which is independent on the specifics of the optical system.

Undoubtedly, the most important component of a CLSM is the objective lens. Since the objective lens is used both for illumination and light collection, its quality is of crucial importance for the overall performance of the CLSM-system. Optical aberrations of the objective lens must therefore be kept to an absolute minimum. It is well known that a simple lens as well as a more complex designed lens systems form images with aberrations. The most common aberrations are *spherical aberrations*, *coma*, *flatness of field criterion*, *distortion*, *longitudinal chromatic aberration*, *and lateral chromatic aberration or chromatic magnification difference*.

High-quality microscope objectives consist of large number of lenses that are assembled and aligned manually. As a result, even the best objectives from the same manufacturer may exhibit large differences in performance. Thus, rigorous selection of the objective used is essential for achieving optimum performance in a CLSM.

The above mentioned aberrations are all interconnected, and it is impossible to eliminate them completely within a single objective. Optical manufacturer classify their objectives into five different groups: *Achromat, apochromat, fluorite objectives, planachromat and planapochromat*. The most commonly used objective is the achromat. It is inexpensive and chromatically well corrected within the green and yellow spectral region. Additionally, its design obeys Abbe's sine condition [15] for one colour for generating images that are spectrally adjusted to the sensitivity of the human eye (Abbe's sine condition states that the ratio of the sines of the angles of the incident and refracted rays to the axis must be constant; this constant is equal to the inverse of the magnification of the image). Nevertheless, achromats show red

and blue colourings at the edges of the image field. Moreover, the image looses in sharpness and shows increased blurring from centre to edge.

In an *apochromat* objective, the chromatic aberration is eliminated for three different colours, and the sine condition is obeyed for two colours. As a result, red and blue colouring effects of the image edges disappear. Compared to an achromatic objective, an apochromat has usually a higher numerical aperture with a correspondingly smaller working distance.

The degree of optical correction of a *fluorite objective* lies between that of an achromat and an apochromat. However, as the typical fluorite objective consists of fewer lenses, its use is preferred in applications where strong image contrast is necessary. They are commonly used in fluorescence microscopy, because producing a bright fluorescence image is usually limited by the ability of the objective lens to transmit the collected fluorescence without losses.

The chromatic correction of the *planachromat* is comparable to that of an achromat. Additionally, it is flat field corrected.

The most advanced objective is the *planapochromat*. However, its brilliant optical performance is counterweighted by an extremely small depth of focus, so that only extremely thin samples can be imaged.

In recent years, manufacturers introduced several new types of objective lenses. Nikon, for example, developed the *CF-objectives* (color-free). CF-objectives are planachromats or planapochromats which produce intermediate images without chromatic magnification differences over the image field. They have to be used with eyepieces that are not designed to correct such chromatic magnification difference. For simplifying video and photographic imaging in the ultraviolet spectral region, Zeiss introduced the *ultrafluor* objectives with chromatic correction in the visible and ultraviolet spectral range.

Currently, most objectives used in CLSM are infinity corrected, meaning that the lens aberrations are minimized for an infinite tube length, i.e. when plane waves incident from infinity are focused to a diffraction limited spot within the sample plane. In contrast, finite designed objectives are optimised for point sources located at a fixed distance behind the objective, usually at 160 mm from the objective's turret mount.

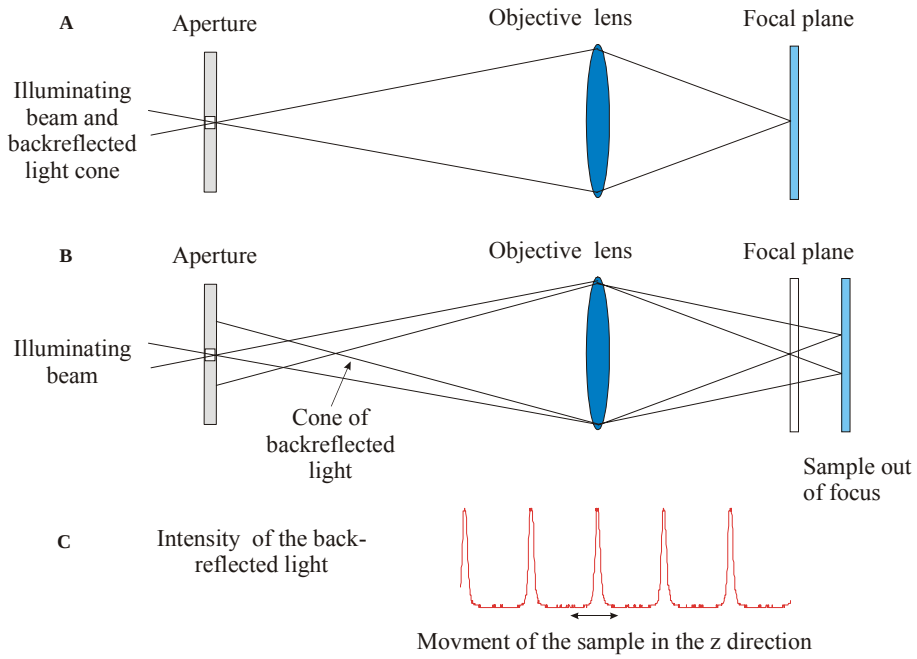

Fig. 2: Simplified schematic of a CLSM showing the sample (A) in the focal plane of the objective and (B) out of the focal plane. For the sake of simplicity, the excitation and emission ray paths are the same in Part A and B. (C) The form of the signal output from the detector as a function of the sample defocus monitored with a Photodiode (UDT Pindiode UDT-PIN 10DP 9412-1, UDT Inc.). The signal is recorded by repeatedly defocusing the sample.

An *infinity corrected objective* transforms light emitted form a point source in the sample plane into a collimated light beam. This beam is refocused into an image by the tube lens. The magnification *m* of the complete setup is determined by the focal length of the objective f_O and the focal length of the tube lens f_T through $m = f_T / f_O$. The intrinsic design advantage of an infinity system is its relative insensitivity to optical components (such as filters, analyzers, compensators, DIC prisms and reflectors) in the optical path between objective and tube lens. Infinity or parallel beams are not affected by the thickness or refractive index of such components as long as they are perpendicular to the optical axis. The location of the image point remains constant, both axially and laterally, as does the alignment between the objective and the tube lens. Another advantage of infinity corrected objectives is that focusing can be done by moving the objective rather than moving the stage. When selecting the appropriate objective lens it should be taken into account that objectives from different manufacturers require tube lenses with greatly differing focal lengths (e.g. Zeiss 160 mm, Olympus 180 mm and Nikon 200 mm). A long focal length of the tube lens enables one to use a large pinhole, which is easier to align.

Individual objectives, even of the same type, differ significantly in their optical characteristics and aberrations. Therefore, testing both the *depth response* and *transverse resolution* is advisable. Depth response can be determined by scanning a mirror axially through the focal plane of the lens and measuring the output of the detector as a function of mirror position (Fig.2 C). The transverse resolution of an objective cannot be measured as easily as depth response. It can be obtained indirectly by measuring the back-reflected light from several different submicron structures of known dimensions such as the pattern of an integrated circuit. The distance between the focal plane and the nearest structural element of the objective is called the *working distance* (WD). In a confocal inverted microscope, the WD sets an upper limit to the distance between focal plane and cover slip surface. In the design process of oil-immersion lenses with high numerical aperture (~ 1.4), the WD is usually set to 0.13 mm. In general, WD becomes shorter with higher NA and with better optical correction. Moreover, with increasing NA, changes of the refractive index between the focal plane and the objective become more critical: For oil-immersion objectives, spherical aberration is corrected optimally only when imaging directly at the water/glass or air/glass interface. Focusing only 0.01 mm above the glass surface causes already considerable spherical aberration (see section 3.3). This limits the usage of oil-immersion objectives for 3D-scanning confocal microscopy. Indeed, the lack of objective lenses with long WD and proper optical correction was, in the early days of CLSM, the most challenging task to be solved. As a result, water-immersion objectives specifically designed for the needs of CLSM have been developed. However, when detecting the fluorescence of surface-immobilized molecules, oil-immersion objectives are advantageous compared with water-immersion objectives. Due to their larger NA, they provide tighter focusing of the exciting laser beam, and yield a larger overall light collection efficiency.

2.7 Pinhole

The pinhole is an important component which has impact both on axial and on lateral resolution of the microscope. In SMD, the pinhole serves mainly for minimizing the detection volume for increasing the signal-to-background ratio (SNR). A smaller pinhole results in a smaller detection volume and consequently lower background, but transmits less signal to the detector. In practice, the pinhole should have approximately the same diameter as the full width at half maximum of the Airy diffraction pattern generated by the tube lens at the pinhole's position (intermediate image plane). For example, assuming diffraction limited focus-

ing and a magnification of 100, then the pinhole diameter should be about 50 to 100 μm, resulting in an overall detection volume of ca. 1 fl.

Precision pinholes are offered in a wide range of different sizes, and of different materials. Precision pinholes are made by laser drilling of stainless steel or gold coated copper substrates. Complete sets of pinholes are offered by different opto-mechanical manufacturers. In these sets, each pinhole is individually mounted and marked with its diameter. To reduce light reflection, blackened pinholes are also available. For allowing comfortable positioning with micrometer resolution, the pinhole should be mounted on a precision xy-stage. However, for obtaining excellent long term stability, the stage must be properly fixed to the microscope's body.

2.8 Refocusing

After passing the pinhole, the light has to be recollected onto the active area of the photoelectric detector. In the case of a single-photon avalanche photodiode (SPAD), the active area has a circular shape, and its sensitivity is position dependent, being highest in the center and falling off towards the edges. Thus, it is recommended to refocus the collected light to the center of the active area. For example, consider a pinhole with 200 μm diameter, which should be imaged into a spot of 20 μm on the active area of a SPAD 120 mm away. For a magnification $m = 10$ and a total distance $(s + s')$ of 120 mm, one finds from the standard thin lens equation a focal length of $f = m(s + s')/(m+1)^2$ or $f = 9.92$ mm .The conjugated distances, s and s' can be found via $m = s'/s$ which yields $s = 109.1$ mm and $s' = 10.9$ mm. Finally, to find the optimum clear aperture or effective diameter $\varnothing$ of the refocusing lens, the relationship between magnification and numerical aperture can be applied. For a numerical aperture of the objective lens of 1.4 and objective/tube lens magnification of 100, on finds

$$\mathrm{NA}_{lens} = \frac{\varnothing}{2s} = \frac{\mathrm{NA}_{Obj.}}{100} = \frac{1.4}{100} \tag{2.6}$$

giving an effective lens diameter of 3.05 mm. Thus, an achromatic lens with a focal length of 10 mm and an effective Diameter of 6 mm should be sufficient for refocusing.

2.9 Photoelectron detector

The three most common photoelectric detectors are the *photomultiplier tube*, the *photodiode* and the *avalanche photodiode*.

The *photomultiplier tube* (PMT) is a vacuum tube device that uses the photoelectric effect to convert optical photons into electrons. A cascade of secondary electron-emitting surfaces – called dynodes – amplifies these photoelectrons. The dynodes generate a virtually noise-free gain in excess of 10^6 with a bandwidth greater than 1 GHz. Because of this gain, PMTs can operate at light levels as low as a few photons per second or as high as about a billion photons per second. They are particularly useful for measurements that must be made in a short time or at high frequency, and for weak optical signals, where external amplifiers cannot be used; or where a very wide dynamic range ($\sim 10^5$) is required. The photocathode determines the PMT's spectral response; commercial photocathodes are available from 100 nm to 1700 nm. Quantum efficiencies range typically between 10 and 20 %, although some newer semiconductor photocathodes can achieve more than 40 % efficiency. The photosensitive surface can be very large – in excess of 500 mm^2: PMT manufacturers provide tabulated values of the properties of their tubes. However, cathode sensitivity as well as gain can vary over a 2:1 range. Additionally, it is possible that the spectral response curve of a special tube can vary due to individual variations of the photocathode composition. Thus, it is recommended to ask the manufacturer for the specific sensitivity values of the individual PMT to be acquired.

The *photodiode* is a solid-state semiconductor device. A photon with energy greater than the semiconductor's bandgap excites an electron into the conduction band and creates a hole in the valance band. An applied voltage shifts this electron hole pair in opposite directions, generating a measurable electric current. The photodiode has no internal gain, and its signal is usually so small that it needs an external amplifier. Because the amplifier introduces some noise, photodiodes are used for measurements at relatively high light levels, where the detector's photon shot noise is greater than the noise of the external amplifiers. Consequently, they reach their highest signal-to-noise ratio when operating in high light levels. Photodiodes are also used at frequencies much lower than photomultiplier tubes for reducing amplifier noise. An advantage of photodiodes is that they can operate at light levels many times higher than allowable for photomultiplier tubes. They are very robust and considerably less expensive. Photodiodes are available for the spectral range between 180 nm and 2600 nm, depending on the semiconductor material. The peak sensitivity of silicon photodiodes is near 900 nm. For this wavelength, the *responsivity* of the device – the generated current per unit of incident

radiation power – is about 0.5 A/W. The photon sensitivity of the diode is defined through its *quantum efficiency* Φ,

$$\Phi[\%] = 100 \frac{\text{photoelectrons}}{\text{incident photons}} \tag{2.7}$$

When relating responsivity to quantum efficiency, one has to bear in mind that, at different wavelengths, different numbers of photons correspond to a given amount of energy. For example, at 500 nm, one has $2.52 \cdot 10^{18}$ photons per Joule, but at 800 nm, there are $4.03 \cdot 10^{18}$ photons per Joule.

The *avalanche photodiode* (APD) is a detector which combines the high quantum efficiency of a photodiode with the high gain of a PMT. Like the photodiode, it is a solid-state semiconductor device that generates electron-hole pairs upon light exposure. However, in contrast to a conventional photodiode, a *reverse* bias of 100 V to 1000 V is applied to the *pn*-junction, creating an internal electric field large enough for electron acceleration. When colliding with the crystal lattice atoms, the accelerated electrons generate new electron-hole pairs, leading to the build-up of an electron avalanche. This leads to a signal amplification with a gain between 50 to 1000. The statistical fluctuations in the number of collisions and the yield of electron-hole pairs create more noise than the dynodes in a PMT but less noise than a photodiode's external amplifier. The resulting gain is considerably less than that of PMT. However, since the quantum efficiency of the APD is roughly an order of magnitude higher, an APD with a gain of 10^3 corresponds to PMT with a gain of 10^4. APD's suffer from relatively high dark currents, and their gain depends strongly on operation temperature. Thus, APDs are usually kept at a fixed temperature.

The most sensitive detection mode of a PMT or an APD is the *single photon counting mode*. In this mode, not the photodetector's current is measured, but single current pulses caused by the incidence of individual photons are counted. Noise discrimination is done by setting a current threshold: only pulses exceeding this threshold are counted as detected photons. Today, *Single Photon Avalanche Diode* (SPAD) modules are offered by Perkin-Elmer Life Science (formerly EG&G) with significantly higher quantum efficiencies than those of PMTs, which makes them competitive with and partially superior to PMTs.

The available *Single Photon Counting Module* (SPCM-AQR) is a self-contained device which detects single photons between 400 nm and 1060 nm. It comes in two versions: The SPCM-AQR-1X utilizes a unique silicon avalanche photodiode with a circular active area of ca. 180 μm diameter and peak quantum efficiency exceeding 70 % at 630 nm. If a larger detec-

tion area is required, the SPCM-AQR-2X provides a quantum efficiency exceeding 35 % at 635 nm within an active area of 475 μm diameter. Both modules are thermoelectrically cooled and temperature controlled.

The SPCM-AQR modules utilize an active quenching circuit allowing count rates exceeding 10^6 counts per second for the SPCM-AQR-1X, and $7 \cdot 10^6$ counts per second for the SPCM-AQR-2X. Single photon arrivals can be timed with an accuracy of 300 ps FWHM. The modules require a $+5$ volt power supply. The generated signals are TTL (Transistor-Transistor-Logic) pulses of 2.5 V amplitude at 50 Ω load, having a width of 25 ps (SPCM-AQR-1X) or 65 ps (SPCM-AQR-2X). To avoid a degradation of the module's linearity and stability, the case temperature should be kept between 5°C and 40°C during operation.

A peculiarity of the SPADs modules is that every detected photon generates a small amount of luminescent light within the diodes crystal, with a broad spectral distribution. This may cause difficulties when employing several SPADs (e.g. for multichannel detection), or if the luminescent light reflects back onto the generating SPAD itself. If the reflected luminescence photons return later than the SPAD's dead time, they may generate false detection events.

2.10 General layout and alignment

Any high-quality inverted microscope with epi-illumination and a photo port can be used as the core mechanical body of the CLSM SMD system. However, there are several topics to be taken into account: (a) the mechanical stability of the body and its mechanical coupling to the external components such as the laser or the detectors are critical; (b) the microscope must possess a filter block for hosting the dichroic mirror and the emission filters; (c) a high N.A. (≥ 1.2) oil-immersion objective has to fit the mechanical and optical layout of the microscope. Care has to be taken to prevent coupling of any vibrations into the whole detection setup. Vibration in the work area may produce relative motion between optical elements, resulting in misalignment and data distortion, and image blurring. Even vibrations with amplitudes in the nanometer range can cause discernible oscillations in the detected optical signal. Thus, it is recommended to mount the complete detection system onto a preferentially actively damped tabletop.

Tabletops have mounting holes for attaching equipment, unless otherwise requested. Custom configurations of these holes, including double densities and cutout shapes in the tabletop itself, are available. Other optional features include laser ports and alternative plate and core materials, e. g., nonmagnetic stainless steel or aluminum. Additionally, smaller, rigid flat sur-

faces – called breadboards – are available, which are ideally suited for laboratory applications that require little space. As with tabletops, they come in a range of different sizes and heights and have the similar thermal characteristics. If no vibration-free optical tabletop is available, the microscope should be set up on a comparably vibration isolating equipment. In order to minimize relative motion between each component of the setup, the microscope, the laser and the detector unit should be placed at mechanically fixed reference points on the tabletop. Likewise, all external mechanical or electrical connections to the vibration-isolated setup should be carefully aligned to avoid vibration flash-over. Finally, working with an inverted microscope is recommended because most of the access ports to the objective side of the optical path are relatively low and close to the table surface. This can help to suppress mechanical vibrations at higher frequencies.

In order to avoid vertical vibration of the microscope relative to the tabletop surface, the microscope body should be mechanically fixed to the tabletop surface, whereby care should be taken to place the microscope in such a way that its access ports are not obstructed. Sufficient place should be left for the incorporation of additional opto-mechanical components.
The best way for the laser beam to enter the microscope body is through the epi-fluorescence port. For directing the laser beam to the port, a two-mirror beam steering device is very convenient. It consists of two mirrors, each mounted on gimbals with angular adjustments. The gimbals, in turn, are mounted on a vibration-resistant post. The mirrors can be adjusted in tandem to change both the lateral placement of the beam in the objective back aperture as well as the beam angle into the objective.
The best place for the dichroic mirror is a multiple channel filter block. Such a setup allows for using alternative filter combinations for different dyes. Some filter holders offered by manufacturers have excitation and emission filter ports which are slightly tilted to minimize the effect of internal reflections on the image. This can lead to slight down-shifts of the bandpass of interference filters by ca. 5 to 10 nm, due the non-normal incidence of the light.
The third critical part of the microscope is the objective lens. It is advantageous to use objective lenses with a numerical aperture of 1.2 or greater. Besides better light collection and laser beam focusing properties, the laser beam can be focused more easily, because the back apertures of such objectives are comparatively large. To achieve diffraction limited focusing, the back aperture or the entrance aperture must be uniformly filled by a nearly planar wave front. Failing to do so results in a smaller effective numerical aperture and hence in a larger focus and lower image resolution. In general, the diameter of an objective's back focal aperture is closely related to its resolution. The higher the resolution and the lower the magnification, the

larger is the diameter of the back focal aperture. The diameter of all optical elements along the detection and excitation path must be large enough for not to obscure any light transmission.

To obtain a rough estimation of the optical alignment, a collimated laser is coupled into the objective lens and focused onto a cover slip surface. The focused laser light will be partially reflected at the coverslip's surface, resulting in a bright circular image at the intermediate image plane, which can be seen when placing a sheet of nearly transparent paper at the video port of the microscope. The focus size at the coverslip's surface can roughly be estimated by dividing the diameter of the back reflected light spot by the objective lens magnification.

Objective lenses of many modern research microscopes are infinity corrected. As already discussed in section 2.6, an infinity corrected objective lens forms a diffraction limited spot on the sample's surface under plane wave illumination. To emulate such a plane wave illumination, a well collimated laser beam can be coupled into the back aperture of the objective lens with its diameter matching the objective lens back-aperture diameter. This can be achieved with a laser beam expander. Beam expanders are commercially available in different magnifications with fixed entrance and exit aperture diameters. Many beam expanders have an adjustable focus control. Adjusting the focus will change the beam divergence and can be convenient for roughly adjusting the laser focus in the object plane. For a more precise adjustment, an external lens can be used which should be placed at the entry point of the laser beam into the microscope. To minimize stray laser light in the system, it is helpful if both the beam expander and additional lenses are antireflection coated at the laser wavelength.

An alternative to a beam expander is a laser system possessing a single mode fiber exit. A laser beam exiting a single mode fiber can be considered to be a point source. It can be collimated by means of a low magnification, infinity corrected objective lens. For alignment, the single mode fiber exit has to be mounted on a xyz-stage so that it can be properly shifted with respect to the collimating lens. The result will be an extraordinarily well collimated laser beam and the possibility to change its divergence angle by changing the distance between fiber and lens.

To obtain a rough estimation of the optical alignment, the laser is coupled into the objective lens as described above, and focused onto a cover slip surface. The focused laser light will be partially reflected at the coverslip's surface, resulting in a bright circular image at the intermediate image plane, which can be seen when placing a sheet of nearly transparent paper at the video port of the microscope. The focus size at the coverslip's surface can roughly be estimated by dividing the diameter of the back reflected light spot by the objective lens magnification.

For safety reasons, it is recommended to implement a shutter for turning off the laser illumination. A black shutter, or a reflective shutter that reflects the beam into a beam stop, are easily available. Alternatively, the laser power can be changed directly. Laser diode intensity is easily changed by changing its operating current. If the laser beam is polarized, the beam can also be attenuated with a Glan-Thompson laser prism. Laser power and beam quality monitoring is performed by reflecting a small percentage of the beam, with an appropriate beam splitter, onto a photodiode or small CCD detector.

2.11 Data acquisition electronics

Here, only digital counting electronics will be considered, which are able to register and process the signals generated by PMTs and SPADs in the single photon counting mode. This is the relevant detection mode in all SMD applications. There are several modes of count registrations. Counts can be sampled within subsequent time bins of equal temporal width (*time binning mode*). A typical electronics capable of such photon count binning is the multifunction PC card PCI-MIO-16E-4 from National Instruments Inc. It is a complete data acquisition board with two 24-bit counter/timer channels and two 12-bit analog input and eight 12-bit analog output channels. It offers PCI bus-mastering and a high speed direct memory access (DMA) controllers for continuous, scatter-gather DMA without demanding resources form the host computer. In order to use the PCI-MIO-16E-4 for single photon counting, the photoelectron pulses from the detector have to be converted to TTL pulses corresponding to the input specifications of the board. The time binning mode is realized by using both on-board counters. The first counter is used to generate a square wave signal for gating the second counter. When the gate of the second counter is active, it counts the number of pulses arriving at the signal input. When the polarity of the gate signal changes, it saves the counter value in the save register. Counting continues uninterrupted since the data is transferred into the computer memory by a DMA channel. In addition, the analog channels of the board can be used to control other processes like scanning.

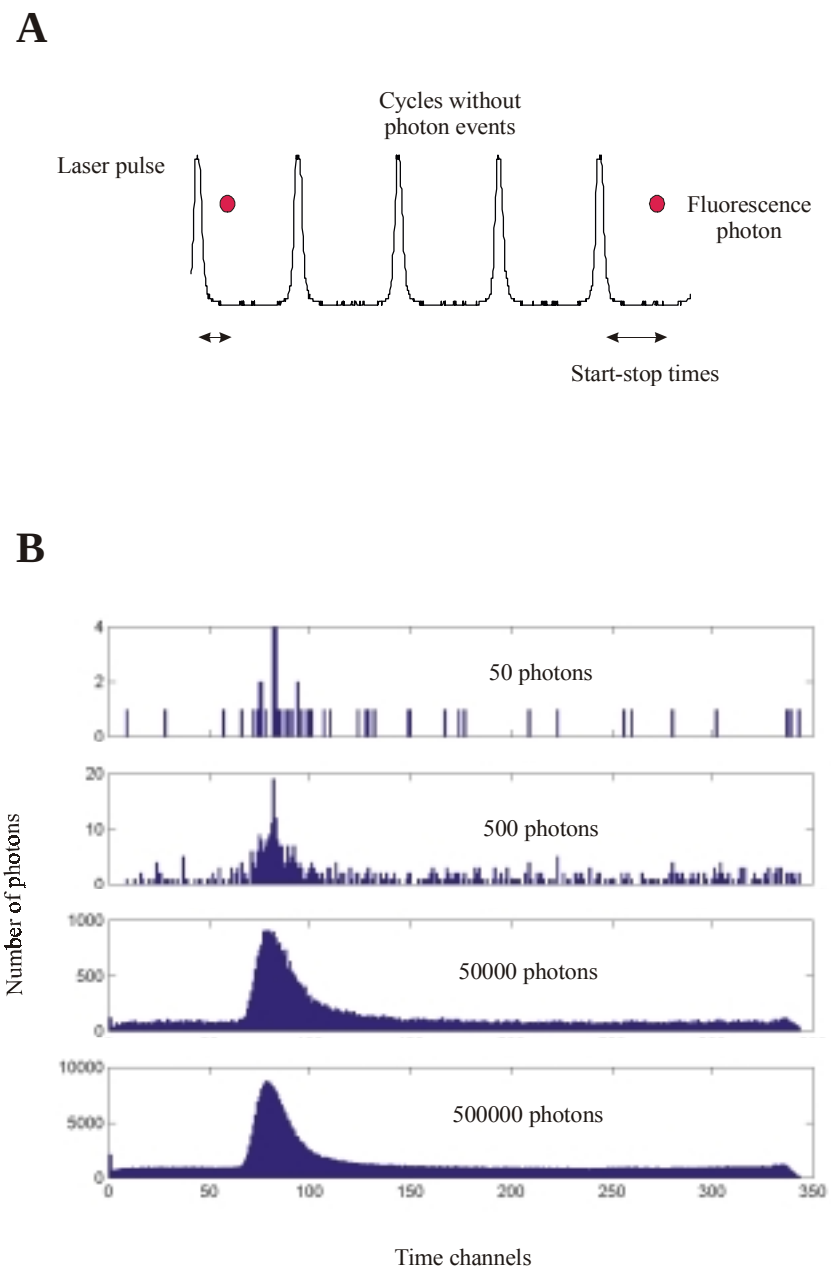

Fig.3: The principle of TCSPC: The first part (A) shows schematically the measurement principle of TCSPC: The time between the excitation pulse and each detected fluorescent photon is recorded. In the panels of the second part (B) TCSPC histograms are presented: The y-axis represents the fluorescence intensity and the x-axis the delay time form the excitation pulse. Each histogram panel shows a histogram with a distinct number of photons. The statistical nature of the TCSPC technique is clearly revealed.

The PCI-MIO-16E-4 allows also the direct recording of individual photoelectron events to the PC's hard disk without onboard counting and bin sorting. The timing of recorded events, with respect to an independent onboard clock, is given by a special time-tag attached to each event (*time-tagged mode*). The onboard digital counter/timer of the PCI-MIO-16E-4 has a resolution of 50 ns. The time-tagged mode has to major advantages over the time-binned mode: (i)

data flow is only generated when a photon detection event occurs, and (ii) the temporal resolution is limited only by the temporal resolution of the on-board counter and the photo-electron detector dead time.

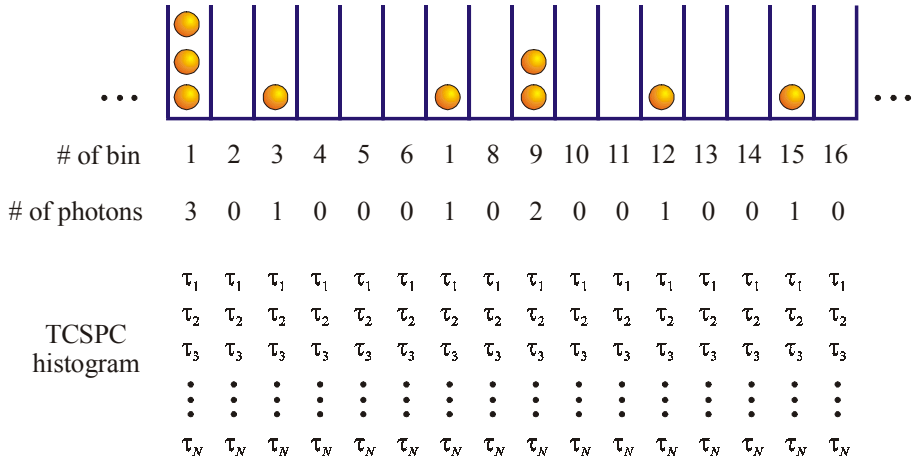

Fig.4a: Synchronous histogram mode of data acquisition: Time is divided into bins of equal width, and for every time bin the number of detected photons together with a complete TCSPC histogram ($\tau_1,\ldots,\tau_N$) is recorded. Thus, for every time bin, $N + 1$ numbers have to be stored, where N is the number of TCSPC channels.

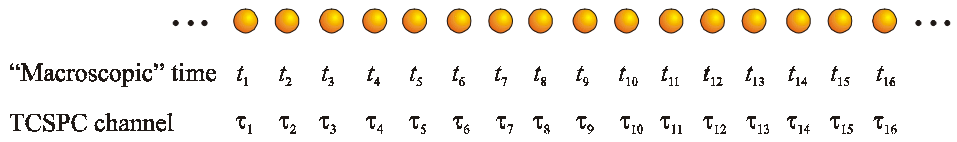

Fig.4b: Asynchronous time-tagged time-resolved (TTTR) mode of data acquisition: Every detected photon is tagged with two numbers: its time of arrival t_j on a "macroscopic" time scale, and its time of arrival after the latest laser pulse τ_j on a picosecond time scale. Data flow is directly proportional to the number of detected photons.

For monitoring fluorescence decay on a picosecond time scale, one needs electronics capable of TCSPC [16]. Additionally to registering the arrival time of the detected photons on a "macroscopic" time scale with ≥ 50 ns temporal resolution, the arrival time of each photon with respect to the last exciting laser pulse is also registered on a "microscopic" picosecond time scale. In standard TCSPC applications, these picosecond arrival times are histogrammed by the acquisition electronics for obtaining a fluorescence decay curve of the observed fluorescence (*histogramming mode*). Fig.3 illustrates how a histogram is formed over multiple excitation/detection cycles. However, histogramming deletes any information about the photons'

macroscopic arrival time. A solution to this problem is building a series of histograms within subsequent time slices of sufficiently small duration (analogous to the time binned mode mentioned above). However, even with the fastest available electronics, histogramming can not be repeated faster than ca. 1 histogram/ms, thus giving a rather coarse macroscopic temporal resolution. Moreover, for weak fluorescence signals, such a data acquisition mode generates huge numbers of histograms containing mostly zeros (only a few photons will be detected during one macroscopic time bin). The alternative to histogramming is the *time-tagged time-resolved mode* (TTTR). In TTTR, every detected photon is tagged with two times, the macroscopic arrival time (with a temporal resolution of ca. 50 – 100 ns) and the picosecond TCSPC time. Both times are directly stored on the PC's hard disc. As in the time-tagged mode, TTTR mode preserves the complete macroscopic temporal resolution of the data acquisition board, and generates data flow only when a photon is detected. Comparison between Histogram mode and TTTR is visualized in Fig. 4a,b. There are two major commercial providers of such TCSPC-electronics: PicoQuant (Berlin, Germany), and Becker & Hickl (Berlin, Germany). The standard block scheme of a TCSPC data acquisition electronics with TTTR capability is shown in Fig.5.

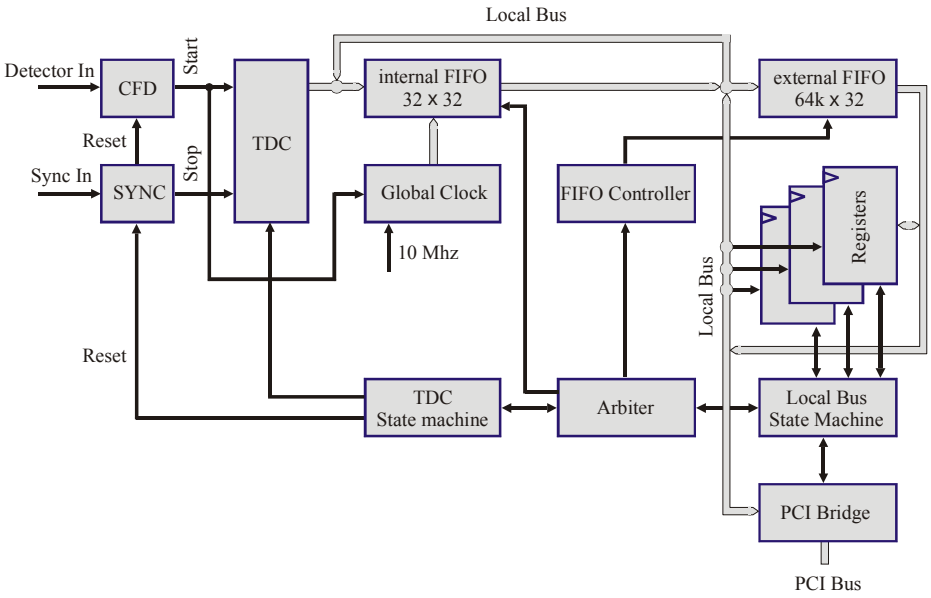

Fig. 5: TCSPC schematic

When considering the maximum achievable rate of data acquisition (photon counting), several topics have to be considered. Firstly, all detectors working in single-photon counting mode have a finite dead time: After the detection of a photon, the detector has to recover before being able to detect the next photon. PMTs can handle count rates of up to 10^6 counts per sec-

ond (cps), standard passively quenched SPADs saturate at a few hundred kcps. Actively quenched SPADs achieve count rates of ca. $5 \cdot 10^6$ cps. Secondly, the acquisition electronics has its own dead time. State-of-the-art TCSPC-electronics reach count rates of up to 16 Mcps, with a macroscopic time resolution down to 50 ns. Thirdly, to prevent statistical distortion of the measured fluorescence decay characteristics (pile-up, see Ref.[16]), photon counting rates should not exceed ca. 1/100 of the laser excitation rate. Usual high-repetition pulsed laser systems provide repetition rates of ca. 100 MHz. Thus, count rates around 1 MHz will be reasonable in most cases, which are easily handled by existing detectors and electronics.

2.12 Scanning instrumentation

For obtaining a complete two-dimensional image of the sample, either the sample or the illuminating beam must be scanned. Several techniques have been developed: *Sample scanning*, *objective scanning*, and *beam scanning*. *Sample scanning* is a good choice for many research applications, because it allows easy modifications of the optical system. For example, sample scanning makes the introduction of phase plates or other optical elements relatively simple because the illumination beam remains stationary. Since in a sample scanning microscope, excitation and imaging is done only near the optical axis, aberration effects have reduced impact on performance, in contrast to beam scanning where the entire field of view of the objective is used. Additionally, in sample scanning image size is solely limited by the scan range of the mechanical sample moving device. However, due to physical limitations of the speed of mechanically moving the sample, sample scanning results in relatively slow scan rates (ca. 10 s and more for a 500 by 500 pixel image with 25 by 25 nm pixel size). High accuracy and vibration stability are required for scanning stages. Typically, the stage should have a spatial resolution of better than 100 nm. Additionally, a sufficient large scan range is desirable for being able to image large samples. A very convenient scan stage is the PI P-527.2CL (Physik Instrumente, Waldbronn, Germany), providing a scan range of 200×200 μm^2. It has a 66×66 mm clear aperture ideally suited for fitting in a scanning microscope. Low voltage piezoelectric transducers (PZT, 0 to 100 V) and flexures are employed as drive and guiding system. The flexures provide zero striction/friction, ultra-high resolution and a high degree of guiding precision. Integrated capacitive position feedback sensors provide sub-nm positioning resolution and stability in closed loop operation.

In *objective scanning*, the objective lens is moved with respect to the fixed sample can be scanned. However, this technique is rarely used because it is difficult to maintain uniform illumination across the field of view.

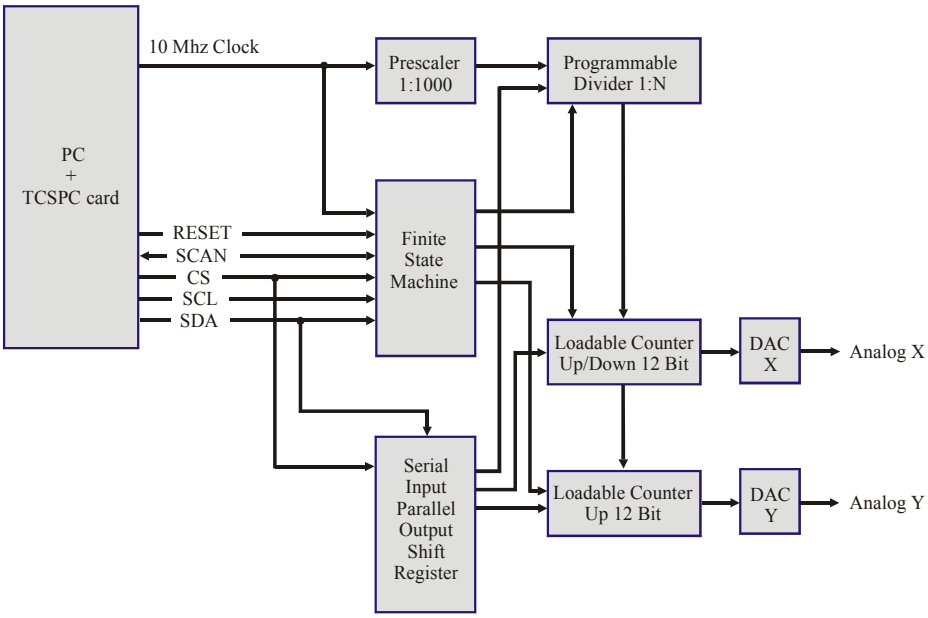

Fig.6: Block diagram of the scanner driver. The driver receives the time tag-clock (10 MHz) to allow pixel-aligned data collection. Thus allowing perfect synchronization with the TTTR mode of the TCSPC electronics. The initial scanner settings and scan range as well as the time per pixel are downloaded via a serial protocol (Serial Input parallel Output Shift Register). The scanner driver consists of a Field Programmable Gate Array that is configured to communicate with the TCSPC board and to drive a Digital to Analog Converter that supplies the x-y control voltages for the two scan directions at a resolution of 12 bit each (Loadable Counter).

The majority of commercial CLSMs employ one or another kind of *beam scanning*, which is typically much faster than sample scanning. Because the scan is de-magnified by the objective lens, the mechanical tolerances of beam scanning systems are less critical than those for sample scanning. Beam scanning CLSM usually uses feedback-stabilized vibrating mirrors which can scan at a frequency of up to 1 kHz per scan line. They achieve scan rates of 0.1 to 30 Hz per image. In an epi-illuminaton system, the collected light is ”de-scanned” by passing the same scan mirrors as the excitation light, before being focused on the fixed detector. As in conventional microscopy, the image size of a beam scanning CLSM is limited to field of view of the used objective lens.

A special method of beam scanning is applying an acousto-optical modulator for fast scanning in at least one direction, while using a mirror to scan the beam along the other direction.

However, while this arrangement works well for confocal reflection imaging, it presents problems for confocal fluorescence imaging, since the longer wavelength fluorescence emission cannot be properly de-scanned by the wavelength-specific acousto-optical modulator. All single-beam CLSMs suffer from the limitations inherent to serial data collection, namely the necessity to compromise between the rate of image acquisition, the spatial resolution of the raster scan, and the signal-to-noise ratio. The usefulness of a fast beam scanning system for SMD fluorescence microscopy is thus controversial, since at low fluorescence signal levels, data acquisition may become limited by the achievable photon emission rates per pixel (see also next paragraph).

An important topic is image reconstruction. For high resolution confocal microscopy, lateral scan resolution of ca. 50 to 100 nm, and axial scan resolution of ca. 200 to 400 nm is reasonable (corresponding to the optical resolution of the microscope). Thus, a 2D image of $12.5 \times 12.5\ \mu m^2$ with 50 nm scan step size will already contain 500×500 pixel. Assuming a typical single molecule fluorescence detection rate of 1 Mcps, and a desired peak number of ca. 100 photons/pixel for the center position of a molecule, one arrives at a reasonable scan rate of ca. 100 µs/pixel. As explained in the previous section, detected photons are preferentially registered and stored as time-tagged or time-tagged time-resolved data. An intensity and/or lifetime image is calculated from these stored photon data only after the scan. This means that there has to be perfect synchronization between scan motion and the time tagging of the detected photons (on a µs time scale). This is rather difficult to realize by means of software within a usually non-real time environment such as Windows. Therefore, direct hardware-based synchronization between scanning and data acquisition is recommended, such as the scanner driver for the PI P-527 series [17]. The scanner driver is driven directly from the TCSPC board. It uses the time tag-clock for driving a scan stage/mirror scanner, ensuring perfect synchronization with the TTTR photon data acquisition. The initial scanner settings and scan range as well as the time per pixel are downloaded via a serial protocol. Fig.6 shows a block diagram of the driver hardware.

2.13 Controlling the objective-sample separation

When scanning large sample areas, an important issue may become keeping the depth of focus perfectly at the sample's surface. For example, for an objective lens with 1.2 NA, the focused laser light has a depth of focus of ca. λ / NA^2 (Eq.2.4), lying in the range of several hundred nanometers. Most CLSMs use a piezoelectric transducer (PZT) to move the micro-

scope objective vertically. Such devices with sufficiently free aperture and mounting adapters for microscope objectives are offered by a several companies (e.g. Physik Instrumente, Piezosystem Jena). A PZT has the advantage of being fast and extremely rigid, allowing to keep the sample in a fixed position without shifting over long times. Their disadvantages are that they have a limited range of motion and hysteresis effects.

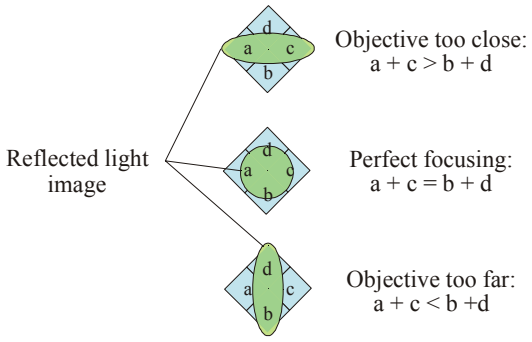

Fig. 7: Functional principal of the autofocus control: a cylindrical lens images light which is back reflected at the sample surface onto a four-quadrant diode. For the correct distance between the oil immersion objective and the sample, the image is circular, but it elongates in two different perpendicular directions for too close or too far a distance.

For keeping the distance between objective and sample surface constant, a feedback mechanism has to be implemented (autofocus). The necessary feedback signal can be derived from the excitation light that is reflected back from the sample's surface (see Fig.7). After passing the objective lens, the reflected light is either convergent or divergent, depending on whether the depth of focus is above of below the sample's surface. At perfect focusing, the reflected light emerges collimated. When sending this light through a cylindrical (astigmatic) lens, the light is focused to a symmetric spot halfway between the two focal planes of the lens. A quadrant diode placed at this position (also called the plane of least confusion) then receives equal intensities of light on its four quadrants. When the sample is out of focus, however, the astigmatism creates an elongated spot on the detector. The orientation of this elongation depends on the sign of defocusing, thus giving information whether the objective is too far away from or too close to the sample's surface (Fig.7). Thus, the ratios of the measured light intensities on the four quadrants give a position error signal (PES), which is then used to drive the PZT for maintaining perfect focus position.

2.14 Summary

In the following chapters, experimental results of single molecule fluorescence detection will be reported, demonstrating the capabilities and performance of the CLSM-SMD system. The schematic of the used system corresponds to that shown in Fig.8.

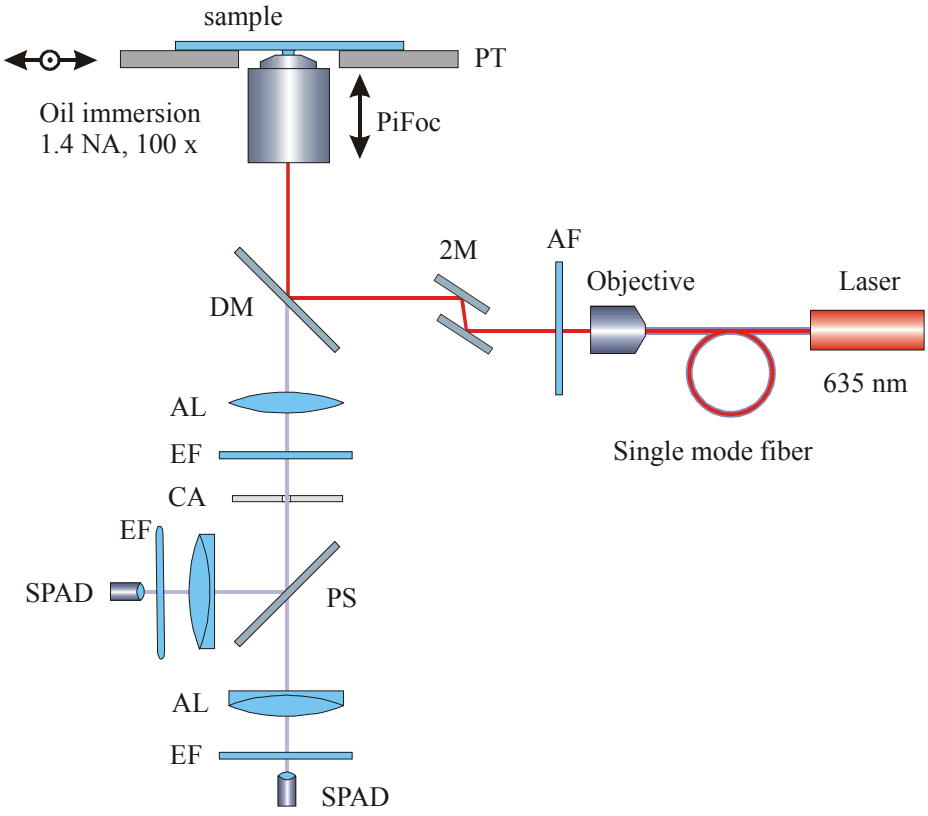

Fig. 8: Schematic of the experimental set-up. Abbreviations: AF – excitation filter; 2M – two-mirror beam steering; PS – polarizing beam splitter; PF + ¼ – polarizer and λ/4-plate; DM – dichroic mirror; EF – emission filter; AL – achromatic lens; CA – confocal aperture; SPAD – single photon avalanche diode; PT – piezo stage; PiFoc – linear piezo actuator; CL – cylindrical lens; QD – quadrant diode. For details, see main text.

The light of a pulsed diode laser (PDL 800, PicoQuant, Berlin) with 635 nm emission wavelength, ~ 80 ps FWHM pulse width, and 40 MHz repetition rate, is coupled to a polarization-maintaining single-mode fiber (core diameter ~ 3 µm). The light exiting the fiber is collimated by an infinity-corrected low magnification microscope objective (Zeiss, 10×, infinity). Fiber alignment is done with mechanical xyz-stage (not shown). The light beam passes an excitation filter (636DF9, Omega Optical) and is directed into a double-mirror beam steering device for laser beam alignment. A polarizer and a λ/4-plate (both Linos Photonics) are used

to change the beam polarization from linear to circular. The dichroic mirror (650DRLP, Omega Optical) reflects the light into a high aperture oil immersion objective (100×, NA 1.4, CFI, Nikon). A tube lens (200 mm focal distance) focuses collected fluorescence light onto a pinhole with 100 μm diameter. An achromatic doublet lens (25 mm focal distance, Linos Photonics) refocuses the light onto the active area (170 μm diameter) of a single-photon avalanche diode (SPAD) (AQR-14, Perkin Elmer, ~ 60 % quantum yield of detection at 670 nm). Two emission band-pass filters (670DF40, Omega Optical), one positioned directly after the tube lens, the other directly in front of the detector, discriminate fluorescence against scattered light. The dark count rate of the single-photon avalanche diode is less than 100 counts per second and thus mostly negligible. For two-channel measurements, a second detection channel is set up by placing a polarizing beam splitter (TSWP 633 nm, Linos Photonics) after the pinhole, and having a second refocusing lens and SPAD in the reflected light path. For the autofocus system, which is implemented as described in Section 2.13, light is reflected with a polarizing beam splitter (TSWP 633 nm, Linos Photonics) onto a cylindrical lens (40 mm focal length), imaging the reflected light onto a quadrant diode (Si PIN photodiode S6242, Hamamatsu). Vertical motion of the objective is realized with a piezo actuator (PIFOC P-721-20, Physik Instrumente). Sample scanning is achieved by mounting the sample onto a xy-nano-positioning system with 200×200 μm^2 scanning range (PI P-527.2CL with additional electronic equipment, Physik Instrumente). Integrated capacitive position sensors provide sub-nanometer positioning resolution and stability in closed loop operation. The stage has a 66×66 mm^2 clear aperture, allowing free access of the oil immersion objective to the mounted sample. The used TCSPC/photon-counting electronics is a TimeHarp 200 PCI-card (PicoQuant). The card can record digital photon detection signals in time-tagged time-resolved (TTTR) mode. TCSPC time is binned into 4096 channels and minimum channel width of < 40 ps. Temporal resolution of time-tagging is 100 ns. Average photon count rate of this card is 2 Mcps. If photon detection rates temporarily exceed this limit, a first-in first-out memory (FIFO) on the card can buffer up to $2^{16} = 65536$ counts for subsequent processing and data transfer to the PC memory.

For synchronization between scan stage and data acquisition, a PI P-527 (PicoQuant) scan stage driver was employed. The driver generates a step-wise periodic-triangular up-down voltage ramp for the x-direction of the piezo stage, and a linearly increasing step-wise voltage ramp for the y-direction. The maximum number of steps in each direction is $2^{12} = 4096$, the step frequency is freely adjustable up to 4 kHz. The voltage of the y-direction is increased by

one increment every time when an up-down ramp of the x-direction is finished. Thus, a rectangular area of the sample surface is scanned with constant scan speed.

2.15 References

1. C.W. Wilkerson, P.M. Goodwin, W.P. Ambrose, J.C. Martin, R.A. Keller, *Appl. Phys. Lett.* **62** (1993) 2030-2.
2. J. Tellinghuisen, P.M. Goodwin, W.P. Ambrose, J.C. Martin, R.A. Keller, *Anal. Chem.* **66** (1994) 64-72.
3. M. Köllner, P. Fischer, J. Arden-Jacob, K.-H. Drexhage, R. Müller, S. Seeger, J. Wolfrum, *Chem. Phys. Lett.* **250** (1996) 355-60.
4. J. Enderlein, P.M. Goodwin, Orden A. Van, W.P. Ambrose, R. Erdmann, R.A. Keller, *Chem. Phys. Lett.* **270** (1997) 464-70.
5. J. Enderlein, M. Sauer, *J. Phys. Chem. A.* **105** (2001) 48-53.
6. E. Abbe, *J. Roy. Micrsoc. Soc.* **(2) 4** (1884) 348-51.
7. M. Born and E. Wolf, *Principles of Optics, Electromagnetic Theory of Propagation, Interference and Diffraction of Light*, 6th ed. (Pergamon Press, Elmsford, NY, 1980).
8. T. R. Corle, G. S. Kino, *Confocal Scanning Optical Micorscopy and Related Imaging Systems* (Academic Press, San Diego, CA, 1996).
9. T. Schmidt, G.J. Schütz, W. Baumgartner, H.J. Gruber, and H. Schindler, *Proc. Nat. Acad. Sci. USA* **93** (1996) 2926.
10. S.A. Soper, Q.L. Mattingly, P. Vegunta, *Anal. Chem.* **65** (1993) 740-7.
11. S.A. Soper, B.L. Legendre, *Appl. Spectrosc.* **52** (1998) 1-6.
12. G. Bachteler, K.-H. Drexhage, J. Arden-Jacob, K.-T. Han, M. Köllner, R. Müller, M. Sauer, S. Seeger, J. Wolfrum, *J. Luminescence* **60&61** (1994) 511-4.
13. M. Sauer, K.H. Drexhage, D. Herten, U. Lieberwirth, R. Müller, M. Neumann, S. Nord, S. Siebert, A. Schulz, C. Zander, J. Wolfrum, in: Near-Infrared Dyes for High Technology Applications (NATO ASI. Ser.3, 52, Kluwer Academics, **1998**) pp. 57-85.
14. K. A. Kelley, J. L. McDowell, *Cytometry* **9** (1988) 277-80.
15. E. Hecht *Optics* (Addison-Wesley, **1987**) p. 239
16. D.V. O' Connor D. and Phillips*Time-correlated single photon counting* (Academic Pess, London, 1984).
17. M. Böhmer, F. Pampaloni, M. Wahl, R. Erdmann, J. Enderlein, *Rev. Sci. Instrum.* **72** (2001) 4145-52.

3. Confocal Single Molecule Detection in Solution

An important special application for confocal fluorescence detection is fluorescence correlation spectroscopy (FCS) and fluorescence intensity distribution analysis (FIDA), which will be the topic of the present chapter. In FCS, fluorescence is not measured directly on the surface of the glass cover slip, but several micrometers above the surface in solution. By evaluating the fluctuations of the measured photon count signal, information about single molecule fluorescence intensity, triplet-state dynamics, rotational and translational diffusivity and other parameters can be extracted. Although no scanning is required, the optical and mechanical requirements for doing FCS measurements are similar to those necessary for imaging surfaces.

3.1 Fluorescence correlation spectroscopy

FCS was first realized in the early 1970 [1,2] and became a very popular spectroscopic technique in the nineties due to significantly improved optics and excitation sources (for overviews see e.g. [3,4]). The molecular parameter which is directly addressed by FCS is the diffusion constant of the fluorescing molecules. Additionally, FCS is a very sensitive method for determining the chemical concentration of a fluorescing species, which made it a promising technique in screening and diagnostics [5-10].

In FCS, the measured fluorescence intensity is correlated with its time-shifted image (autocorrelation) for varying time-shift values, generating the autocorrelation curve $g(t)$. If, for simplicity, any background is neglected, the measured signal $I(t)$ is due completely to the fluorescence of all the molecules within the sample,

$$I(t) = \sum_j I_j(t), \tag{3.1}$$

where the index *j* refers to the *j*th molecule, and the summation runs over all molecule in solution. Thus, the autocorrelation curve $g(t)$ is given by

$$\begin{aligned} g(t) &= \langle I(t_0) I(t_0 + t) \rangle \\ &= \left\langle \left(\sum_j I_j(t_0) \right) \left(\sum_k I_k(t_0 + t) \right) \right\rangle \\ &= \sum_j \langle I_j(t_0) I_j(t_0 + t) \rangle + \sum_{j \neq k} \langle I_j \rangle \langle I_k \rangle \end{aligned} \tag{3.2}$$

where the triangular brackets denote averaging over all possible time values t_0. In the last line it was taken into account that fluorescence photons coming from different molecules are completely uncorrelated (no intermolecular interaction provided). Because all molecules in solution are indistinguishable, the last equation can be simplified further to

$$g(t) = N \langle i(t_0) i(t_0 + t) \rangle + N(N-1) \langle i(t_0) \rangle^2, \tag{3.3}$$

where *i* is the measured fluorescence intensity of *any* molecule, averaged over all start positions of the molecule, and N is the total number of molecules present in the sample. Thus, the task of calculating the function $g(t)$ reduces to calculating $\langle i(t_0) i(t_0 + t) \rangle$, the correlation of the fluorescence signal stemming from the same molecule, and $\langle i \rangle$, the average fluorescence intensity signal of a molecule. In the most general way, the correlation $\langle i(t_0) i(t_0 + t) \rangle$ can be expressed as

$$\begin{aligned} &\langle i(t_0) i(t_0 + t) \rangle = \\ &\quad = V^{-1} \left(\frac{\phi_f}{\tau_f} \right)^2 \int d\Omega_0 \int d\Omega_1 \int d\vec{r}_0 \int d\vec{r}_1 \, U(\vec{r}_1, \Omega_1) K(\vec{r}_1, \Omega_1, t | \vec{r}_0, \Omega_0) U(\vec{r}_0, \Omega_0) s(\vec{r}_0, \Omega_0), \end{aligned} \tag{3.4}$$

where $s(\vec{r}_0, \Omega_0)$ is the probability that the molecule is in its excited state if it has, at some start time t_0, the position $\vec{r}_0$ and orientation Ω_0; $U(\vec{r}, \Omega)$ is the light collection efficiency function (CEF) of the measurement system for detecting a photon from an emitting molecule at position $\vec{r}$ and orientation Ω; $K(\vec{r}_1, \Omega_1, t | \vec{r}_0, \Omega_0) d\vec{r}_1$ is the conditional probability that the molecule, starting in the ground state at position $\vec{r}_0$ and having orientation Ω_0 at some start time t_0, will be in the excited state within the volume element $d\vec{r}_1$ at position $\vec{r}_1$ and having orientation Ω_1 at time $t_0 + t_1$; ϕ_f and τ_f are the fluorescence quantum yield and decay time, re-

spectively; and V is the total volume of the sample solution, over which the spatial integrations are carried out. The integrations over Ω_0 and Ω_1 extend over all possible molecule orientations, and it is assumed that the integration measure is chosen in such a way so that $\int d\Omega = 1$. It should be noted that the start time t_0 does not explicitly occur on the r.h.s. of the last equation, reflecting invariance of an FCS measurement with respect to time translation. This is a correct assumption as long as photobleaching or other processes, leading to irreversible extraction of fluorescing molecules from the sample, can be neglected. Finally, the one-molecule average fluorescence signal is given by

$$\langle i \rangle = V^{-1} \frac{\phi_f}{\tau_f} \int d\Omega \int d\vec{r} U(\vec{r}, \Omega) s(\vec{r}, \Omega). \tag{3.5}$$

Inserting the above expressions into the equation for the autocorrelation function $g(t)$ one finds

$$\begin{aligned} g(t) = \left(\frac{\phi_f}{\tau_f} \right)^2 \Bigg[& c \int d\Omega_0 \int d\Omega_1 \int d\vec{r}_0 \int d\vec{r}_1 \, U(\vec{r}_1, \Omega_1) K(\vec{r}_1, \Omega_1, t | \vec{r}_0, \Omega_{01}) U(\vec{r}_0, \Omega_0) s(\vec{r}_0, \Omega_0) \\ & + c^2 \left[\int d\vec{r} \, U(\vec{r}, \Omega) s(\vec{r}, \Omega) \right]^2 \Bigg], \end{aligned} \tag{3.6}$$

where the molecular concentration $c = N/V$ was introduced and the approximation $N(N-1)/V^2 \approx c^2$ was made. Eq. (3.6) is of very general validity, capable of taking into account molecular effects like triplet state dynamics, multiple state fluorescence behavior, optical saturation, rotational diffusion, and most general molecular transport modes such as complex diffusion and/or fluid flow.

In the following, the assumption is made that the rotational diffusion of the molecules is much faster than their fluorescence lifetime, so that the molecules can be considered to be isotropic emitters. In that case, all dependencies on molecular orientation are disappearing in the above equations, significantly simplifying all subsequent considerations. Furthermore, if the molecules cycle only between the ground and excited state, without intersystem crossing or transitions into other excited state levels, then the probability of finding a molecule in the excited state when it is at position $\vec{r}$ is given by

$$s(\vec{r}) = \frac{\sigma E(\vec{r})}{\tau_f^{-1} + \sigma E(\vec{r})} \approx \tau_f \sigma E(\vec{r}), \tag{3.7}$$

where σ is the absorption cross section, and $E(\vec{r})$ the excitation light intensity at position $\vec{r}$. The last expression on the r.h.s. is a valid approximation for excitation intensities far below optical saturation, $E(\vec{r}) << (\sigma\tau_f)^{-1}$.

For molecules with such simple photophysical behaviour, the "propagator" $K(\vec{r}_1, t|\vec{r}_0)$ splits into a purely photophysical and a pure transport part:

$$K(\vec{r}_1, t|\vec{r}_0) \equiv s(\vec{r}_1) G(\vec{r}_1, t|\vec{r}_0), \tag{3.8}$$

where $G(\vec{r}_1, t|\vec{r}_0)$ is the conditional probability that a molecule will be found at position $\vec{r}_1$ after time t if it was found at position $\vec{r}_0$ at zero time. For a freely diffusing molecule, this function is given by the Green's function of the diffusion equation,

$$G(\vec{r}_1, t|\vec{r}_0) \equiv G(\vec{r}_1 - \vec{r}_0, t) = \frac{1}{(4\pi D t)^{3/2}} \exp\left[-\frac{(\vec{r}_1 - \vec{r}_0)^2}{4Dt} \right], \tag{3.9}$$

where D denotes the diffusion coefficient, and G depends only on the position distance $\vec{r}_1 - \vec{r}_0$. Collecting together all above expressions, one finds

$$g(t) = (\phi_f \sigma)^2 \left[c \int d\vec{r}_1 \int d\vec{r}_0 \, U(\vec{r}_1) E(\vec{r}_1) G(\vec{r}_1 - \vec{r}_0, t_0) U(\vec{r}_0) E(\vec{r}_0) + c^2 \left[\int d\vec{r} \, U(\vec{r}) E(\vec{r}) \right]^2 \right]. \tag{3.10}$$

Already at this point, without any further specification of the functional shape of the functions $E(\vec{r})$ and $U(\vec{r})$, a remarkable property of $g(t)$ can be derived. Taking into account the zero and infinity time properties of G,

$$\begin{aligned} \lim_{t \to 0} G(\vec{r}_1 - \vec{r}_0, t) &= \delta(\vec{r}_1 - \vec{r}_0) \\ \lim_{t \to \infty} G(\vec{r}_1 - \vec{r}_0, t) &= 0 \end{aligned} \tag{3.11}$$

one finds for the corresponding limits of $g(t)$

$$\lim_{t\to 0} g(t) \equiv g_0 = (\phi_f \sigma)^2 \left[c \int d\vec{r} \left[U(\vec{r}) E(\vec{r}) \right]^2 + c^2 \left[\int d\vec{r}\, U(\vec{r}) E(\vec{r}) \right]^2 \right],$$
$$\lim_{t\to \infty} g(t) \equiv g_\infty = (\phi_f \sigma)^2 c^2 \left[\int d\vec{r}\, U(\vec{r}) E(\vec{r}) \right]^2 . \tag{3.12}$$

This leads to the remarkable relation

$$\frac{g_\infty}{g_0 - g_\infty} = c \frac{\left[\int d\vec{r}\, U(\vec{r}) E(\vec{r}) \right]^2}{\int d\vec{r} \left[U(\vec{r}) E(\vec{r}) \right]^2} = c v_{eff} , \tag{3.13}$$

connecting the zero and infinity time limits of the autocorrelation function with the concentration c of the fluorescing molecules. The proportionality factor on the r.h.s. represents the effective detection volume $\int d\Omega$ and depends only on the excitation light distribution and the CEF of the measurement system, but not on *any* molecular parameter such as fluorescence quantum yield, absorption cross section etc. Thus, measuring the fluorescence autocorrelation function allows, in principle, to determine absolute molecular concentrations. The single additional ingredient necessary is the explicit knowledge of the product $U(\vec{r})E(\vec{r})$.

In nearly all papers on FCS, the *ad hoc* assumption

$$U(\vec{r}) E(\vec{r}) = \kappa \exp\left[-2\frac{x^2 + y^2}{a^2} - 2\frac{z^2}{b^2} \right] \tag{3.14}$$

is made, thus assuming a three-dimensional Gaussian distribution for the function $U(\vec{r})E(\vec{r})$ with the three parameters κ, a and b. This leads to a simple algebraic expression of the autocorrelation function,

$$g(t) = a^2 b \sigma^2 \phi_f^2 \kappa^2 \left(\frac{\pi^{3/2}}{8} \right) \left[\frac{c}{\left(1 + 4Dt/a^2\right)\sqrt{1 + 4Dt/b^2}} + \pi^{3/2} c^2 \right], \tag{3.15}$$

and, subsequently, to the relation

$$\frac{g_\infty}{g_0 - g_\infty} = c\pi^{3/2} a^2 b, \tag{3.16}$$

determining the effective detection volume as $v_{eff} = \pi^{3/2} a^2 b$.

3.2 Effect of dead time and afterpulsing on correlation functions

For single-photon counting, a detector with internal gain is essential because of signal-to-noise considerations. In avalanche photodiodes (APDs), an incident photon produces a current avalanche in close analogy to a photomultiplier tube (PMT). This avalanche generates the internal gain not exhibited by ordinary photodiodes as discussed in section 2.9. In the sub-Geiger mode the gain may be approximately 10^2, whereas under *Geiger* conditions where a reversed bias supply voltage is chosen above breakdown, so that a typical gain of 10^6 can be achieved.

In Geiger mode any photon absorbed in the semiconductor will generate an electron-hole pair, which is separated and accelerated in the applied electric field. Its kinetic energy will then generate additional charges, thereby creating a *current avalanche*. This avalanche generates the internal gain not exhibited by ordinary photodiodes. However, in contrast to the PMT, the avalanche current has to be terminated by electronic means. The termination of the current avalanche is achieved by reducing the electric field so that the avalanche current falls below the latch current, whereby an efficient *quench* usually requires a reduction of the electric field below breakdown.

The first single-photon APDs (SPADs) operated as a single-photon counting system were *passive quenched* devices, in which a large load resistor R_L was placed in series with the diode. During avalanche, the voltage drop across the load resistor decreases the voltage across the diode so that the current drops below the latch value. Subsequently, the depletion layer is recharged within the characteristic time $t_r = R_L \cdot C_D$, where C_D is the capacitance of the diode plus any stray capacitance. During the recharging time the SPAD is completely unresponsive until the bias voltage is again above breakdown, which typically lasts 200 ns. Accordingly, a passive quenched SPAD shows no sharply defined *dead time*. In *active quenching*, fast transistors, triggered by the breakdown pulse, are used to quickly lower and then reset the bias voltage, hence producing a shorter dead time of about 40 ns.

The flow of charges associated with every avalanche fills up impurity levels in the semiconductor band gap. Some of the generated charge carriers however are temporarily trapped in the junction depletion layer. When these carriers are released by thermal excitation new free carriers are created that can lead to afterpulses which are correlated with the initial event. This effect can be partly compensated by allowing the trap population to relax during a deep and long lasting quench of the supply voltage. However, this liberation of trapped charges leads to the considerably worse *afterpulsing* behavior observed with SPADs in comparison with PMTs.

According to Ref.[11] the applications of single-photon detectors can be roughly divided into three classes differing in the requirements on the performance of the detector: The first class consists of *simple low level light detection*, which only requires a good sensitivity and a reasonable linearity or simple formulas for nonlinearity corrections. The second class is *single-photon timing* [12], which requires a low timing jitter of the output pulse, but dead time and afterpulsing play only a minor role since only the first photoevent following a start trigger is registered. However, the most stringent requirements on the detector are imposed by the third class of applications encompassing *photon correlation experiments* such as dynamic light scattering or fluorescence correlation. Such experiments are particularly sensitive to dead time and afterpulsing as they strongly distort the temporal photoncount correlation function, which is the fundamental quantity in photon correlation experiments.

The distortion of the photoncount correlation function by dead time and afterpulsing is twofold. Firstly, one observes the *direct effect*, which is due to a violation of the assumption of statistical independence, i.e. the independence of the detection process in two distinct time intervals. This assumption is distorted by the finite dead time of the SPAD: The probability to detect a photon depends on the arrival time of the preceding pulses, resulting in a correlation hole for time lags smaller than the detectors dead time. Additionally, the assumption of statistical independence is distorted by the afterpulsing behavior of the SPAD: The probability to detect an event after the registration of a photon is virtually increased due to afterpulsing, leading to an overshooting of the correlation function.

The second type of distortion due to dead time and afterpulsing are *indirect effects*, which stem form the non-linearity of the expected count rate with the incident light intensity. This effect is particularly severe in experiments were large fluctuations of the signal occur. Nonlinearity due to dead time results in flattening of the signal peaks and thus in server distortions of the correlation function.

If the direct effects are not tolerable, a simple practical approach is employed: by splitting the received light onto two SPADs and performing a cross correlation of the two photoncount

signals, the statistical independence of the detection process in the two distinct channels eliminates any direct effect. However, even when using the cross-correlation scheme, indirect effects remain present in experiments were large fluctuations of the signal occur. Depending on the experimental conditions, this has to be considered for correct data analysis.

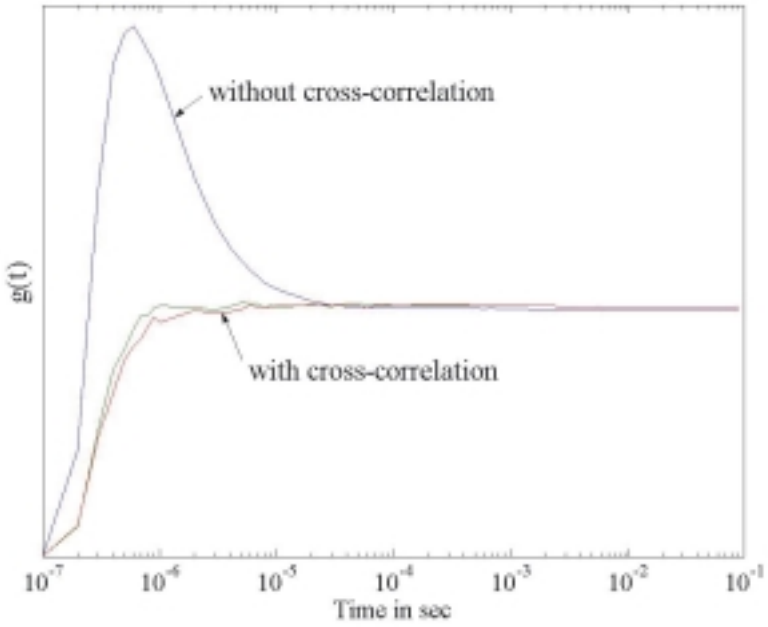

Fig. 9: Auto- and cross correlation of a non-correlated light source.

For the investigation of the direct effects, the photoncount correlation in the auto- and cross correlation scheme was measured with the help of two actively quenched SPADs (SPCM-AQR-14, for details see Part 2.9), using attenuated daylight as a source of non-correlated light. Both detectors supplied standard TTL output pulses, which were directly fed into a router of the TCSPC card (TimeHarp 200 PIC board, PicoQuant). The card can record photon-detection signals in the TTTR mode. In TTTR mode (see section 2.11) the card computes a 32 bit label for every detected photon: 16 bit contain the TCSPC time, 12 bit the time tag, 1 bit indicates overflow of the time tag counter, and 3 bits keep the routing information. From this 32 bit label the time tag and routing information is used to calculate the photon correlation function with 100 ns temporal resolution. Fig.9 shows the corresponding auto- and cross correlation function. The cross correlation function exhibits only small distortions due to the dead time of the TCSPC board, whereas the autocorrelation function displays a huge peak due to afterpulsing.

3.3 Calculation of the light collection efficiency function in fluorescence correlation spectroscopy

For extracting quantitative values of diffusion coefficient and/or the solute concentration from the measured FCS curve, precise knowledge of the fluorescence detection function is required. The fluorescence detection function is defined by the convolution of the excitation intensity distribution and the fluorescence collection efficiency function (CEF). In nearly all publications on FCS, this fluorescence detection function is assumed to have a simple three-dimensional Gaussian shape. This assumption has the advantage of leading to simple algebraic expression for the FCS curves, containing two adjustable parameters (the widths of the Gaussian distribution along the two principal directions along and perpendicular to the optical axis). However, the actual fluorescence detection function has a rather complicated shape, only marginally resembling a three-dimensional Gaussian distribution. It is by lucky chance that the standard model fits so well the experimental FCS curves. The actual physical meaning of the two fit parameters remains rather obscure. Accordingly, no *absolute* values for the diffusion coefficient or solute concentration can be determined (although comparative measurements are still possible).

There is no principal difficulty in modeling FCS curves based on the knowledge of the exact excitation intensity distribution and CEF. When calculating both the excitation intensity distribution and the CEF, one has to take into account possible optical aberrations occurring when a water-immersion objective is not well corrected to the thickness of the cover slide through which the detection is made, or when an oil-immersion objective images deep into a solution having a lower refractive index than that of the immersion oil. Especially the latter is the case when using oil-immersion objectives with high numerical aperture for FCS measurements in solution, which is, from an experimental point of view, very convenient, due to the broad availability and relatively low cost of high quality oil-immersion objectives. How to calculate the electric field distribution (and thus intensity distribution) of a focused laser under such conditions was shown in detail in Ref.[13]. An exact wave-optics approach to the calculation of the dipole-imaging-CEF under similar conditions is still missing. Special attention has to be paid that most fluorescent molecules exhibit the emission characteristics of an electric dipole emitter. When calculating the CEF, this dipolar character of the emission can not be neglected, especially if one aims at modeling fluorescence anisotropy measurements.

The goal of the present section is to present a general approach for calculating the dipole-imaging-CEF for both water and oil-immersion objectives, taking into account aberrational effect, caused either by thickness variations of the used cover slides (water-immersion objec-

tives), or by refractive index mismatch between solution and immersion medium (oil-immersion objective). As will be discussed in the next section knowledge of the exact CEF, together with the excitation intensity distribution, will allow for a complete *ab-initio* modeling of FCS data, opening the way for absolute quantification of diffusion coefficients, solute concentrations, as well as photophysical kinetics or rotational diffusion coefficients.

3.3.1 Theory

Two different imaging setups are considered here: imaging with a cover-slip corrected water immersion objective, and imaging with an oil-immersion objective. The theoretical approach for calculating the CEF in both cases is based on the theory developed by Richards and Wolf in their seminal papers Ref.[14,15]. The core idea of their approach is to represent the electromagnetic field in image space as a superposition of plane waves, and finding a relation between the amplitudes and polarizations of these plane waves and the intensity and polarization distribution of the electromagnetic field in object space. The main assumption made is that the objective is perfectly aplanatic, which means that one has a purely linear relationship between object and image points (points in the sense of centers of spherical wave fronts). For high quality objectives, this is a realistic assumption for object points near the optical axis and with axial position close to the objective's focus (at its working distance) – exactly the region of interest in FCS measurements.

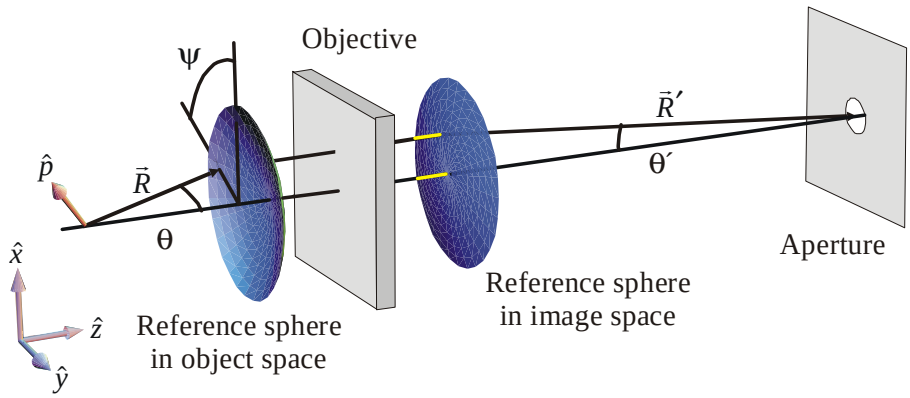

Fig.10: Schematic of imaging a dipole emitter onto a confocal aperture by an apoplanatic objective.

The general imaging geometry is schematically shown in Fig.10. An oscillating dipole (e.g. fluorescing molecule) emits light which has, at distances much larger than the wavelength of light, a nearly spherical wave front. The objective converts this light into a converging, nearly spherical wave front in image space. Here and in the following, the term ”objective” refers to the complete optics which images the object space onto the confocal aperture in image space, and may thus also comprise e.g. a tube lens.

As was shown in Ref.[16], for a dipole emitter located at exactly the objective's focus (on the optical axis at the exact working distance of the objective), the components E_a of the electric field amplitude at a target point near the focal plane in image space are given by

$$E_a(\rho', \phi', z') = 2\pi \frac{e^{ikR+ik'R'}}{R} \int_0^{\theta'_{\max}} d\theta' \sin\theta' \sqrt{\frac{\cos\theta'}{\cos\theta}} G_{ab}^E(\theta', \phi', \rho') p_b \exp[ik'z'\cos\theta'], \qquad (3.17)$$

where the subscripts a and b denote Cartesian components x, y, z (z along the optical axis), summation over repeating indices is assumed; R is the distance from the dipole emitter to a point (determined by θ and ψ) on a reference sphere around the object space focus; R' is the radius of the reference sphere around the image space focus, respectively (see Fig.10); k and k' are the wave numbers of the light in object and image space, respectively; ρ' is the distance of the target point from the optical axis; z' is the distance of the target point from the image plane along the optical axis; ϕ' is the angle between the plane containing the target point and the optical axis, and the xz-plane; and the p_b are the Cartesian components of the dipole amplitude. The relation between angles θ and θ' is given by the magnification M of the objective via $\tan\theta = M \tan\theta'$, and the integration limit of θ' is defined through the numerical aperture NA and the refractive index n of the object space by

$$\theta'_{\max} = \arctan\left[\frac{\mathrm{NA}}{M\sqrt{n^2 - \mathrm{NA}^2}}\right]. \qquad (3.18)$$

The components of the tensor G_{ab}^E are given by:

$$
\begin{aligned}
G_{xx}^{E} &= \frac{1}{2}\left(t_s + t_p \cos\theta' \cos\theta\right) J_0 + \frac{1}{2}\left(t_s - t_p \cos\theta' \cos\theta\right) J_2 \cos 2\phi', \\
G_{xy}^{E} &= G_{yx}^{E} = \frac{1}{2}\left(t_s - t_p \cos\theta' \cos\theta\right) J_2 \sin 2\phi', \\
G_{xz}^{E} &= -i t_p \cos\theta' \sin\theta J_1 \cos\phi', \\
G_{yy}^{E} &= \frac{1}{2}\left(t_s + t_p \cos\theta' \cos\theta\right) J_0 - \frac{1}{2}\left(t_s - t_p \cos\theta' \cos\theta\right) J_2 \cos 2\phi', \\
G_{yz}^{E} &= -i t_p \cos\theta' \sin\theta J_1 \sin\phi', \\
G_{zx}^{E} &= i t_p \sin\theta' \cos\theta J_1 \cos\phi', \\
G_{zy}^{E} &= i t_p \sin\theta' \cos\theta J_1 \sin\phi', \\
G_{zz}^{E} &= -t_p \sin\theta' \sin\theta J_0,
\end{aligned}
\tag{3.19}
$$

where the $J_{0,1,2}$ denote Bessel functions of the first kind [17] with argument $k'\rho' \sin\theta'$. In addition to Ref.[16], Fresnel's transmission coefficients for plane *p*- and *s*-waves, $t_{p,s} = t_{p,s}(\theta)$, were introduced for taking into account the polarization dependent reflection losses at the solution/cover slide interface.

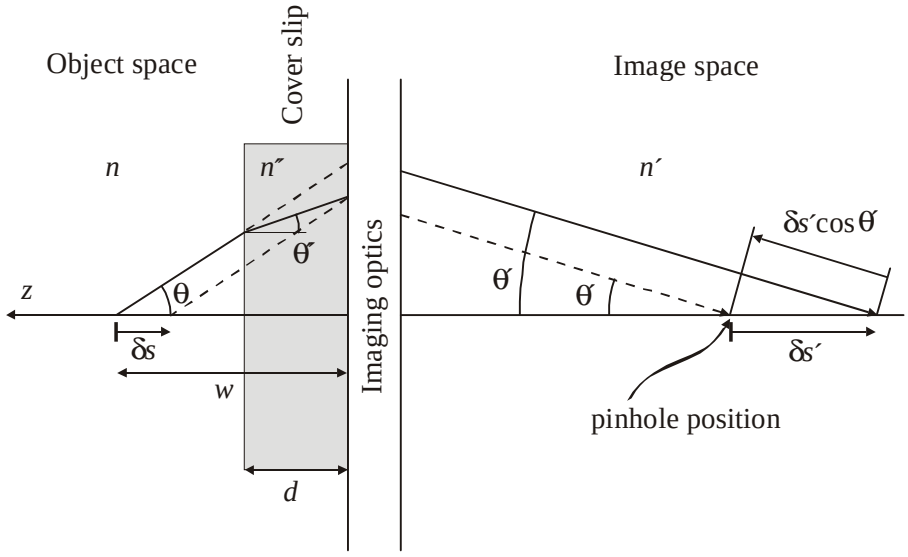

Fig.11: Geometry of imaging through a water immersion objective and a coverslip which is by a value d thicker than the value for perfect imaging. Dashed lines represent light ray propagation in the absence of the coverslip layer of thickness d.

The magnetic field amplitudes, B_a, are given by expressions similar to those of Eq.(3.17) but multiplied with n' (refractive index of image space), and with a different tensor G_{ab}^B:

$$
\begin{aligned}
G_{xx}^B &= -G_{yy}^B = \frac{1}{2}\left(t_p \cos\theta - t_s \cos\theta'\right) J_2 \sin 2\phi', \\
G_{xy}^B &= -\frac{1}{2}\left(t_p \cos\theta + t_s \cos\theta'\right) J_0 - \frac{1}{2}\left(t_p \cos\theta - t_s \cos\theta'\right) J_2 \cos 2\phi', \\
G_{xz}^B &= i t_p J_1 \sin\theta \sin\phi', \\
G_{yx}^B &= \frac{1}{2}\left(t_p \cos\theta + t_s \cos\theta'\right) J_0 - \frac{1}{2}\left(t_p \cos\theta - t_s \cos\theta'\right) J_2 \cos 2\phi', \\
G_{yz}^B &= -i t_p J_1 \sin\theta \cos\phi', \\
G_{zx}^B &= -i t_s J_1 \sin\theta' \sin\phi', \\
G_{zy}^B &= i t_s J_1 \sin\theta' \cos\phi', \\
G_{zz}^B &= 0 .
\end{aligned}
\tag{3.20}
$$

When considering a water-immersion objective, additional aberrational effects may come into play. Usually, water-immersion objectives are corrected for taking into account the presence of a standard glass cover slide between the objective and the sample solution. A deviation of the cover slide's thickness from its standard value introduces optical aberrations. Consider the situation that the cover slide's thickness is too large by some value d (see Fig.11). From a geometrical optics point of view, a light ray emerging from a point source is refracted towards the optical axis at a plane which is a distance d closer towards the source than what would be the case for perfect imaging (Fig.11 shows the situation for an on-axis emitter positioned at the working distance w of the objective). For the objective, such a ray appears as emerging under ideal imaging conditions ($d = 0$) from a point source a distance δs closer towards the objective than the actual source. If the emitter is located on the optical axis a distance $w + \delta z$ away from the objective, then δs is given by

$$
\delta s = w - \frac{\left(w + \delta z - d\right)\tan\theta + d\tan\theta''}{\tan\theta} = \delta z + d\left(1 - \frac{\tan\theta''}{\tan\theta}\right), \tag{3.21}
$$

where θ'' is the angle of propagation after refraction by the water/cover slip interface, and is related to θ by Snellius' law: $n\sin\theta = n''\sin\theta''$, n'' being the refractive index of the cover

slide. For a perfectly aplanatic objective, the refracted light ray will be converted into a light ray crossing the optical axis a distance $\delta s'$ behind the image plane, whereas

$$\delta s' = M^2 \delta s \,. \tag{3.22}$$

From a wave optics point of view this means that, in image space, the plane wave component propagating at an angle θ' has acquired some phase shift Δ with respect to the same plane wave component under perfect imaging conditions ($d = 0$). Simple geometric considerations show that this phase shift is determined by the relation (cf. Fig.11)

$$\frac{\Delta}{k_0} = -n\delta s + n'(1-\cos\theta')\delta s' + d\tan\theta''\left(\frac{n''}{\sin\theta''} - \frac{n}{\sin\theta}\right), \tag{3.23}$$

where k_0 is the vacuum wave number. The first two terms in Eq.(3.23) account for the optical path differences acquired during propagation in object and image space, whereas the last term is the optical path difference acquired during propagation within a slab of the cover slide with thickness d. The field amplitudes in image space are given by expressions similar to those of Eqs.(3.17,3.19,3.20), but with the tensor components $G_{ab}^{E,B}$ multiplied by the additional factor $\exp(i\Delta)$.

A similar line of reasoning can be followed when considering an oil-immersion objective looking into a liquid solution having a refractive index value which is lower than that of glass and the immersion oil. This situation is depicted in Fig.12. Here, w denotes again the working distance of the objective, and d is the distance by which the objective's focus is moved into the solution away from the glass surface. Normally, an oil-immersion objective is perfectly corrected for imaging directly at the glass/solution interface. An emitter which is located on the optical axis a distance d away from that interface appears for the objective as emerging under perfectly matched imaging conditions ($d = 0$) from a source a distance δs *farther away* from the objective than the actual emitter. For an emitter located a distance $w + \delta z$ away from the objective δs is given by

$$\delta s = \frac{(d+\delta z)\tan\theta + (w-d)\tan\theta''}{\tan\theta''} - w = (d+\delta z)\frac{\tan\theta}{\tan\theta''} - d \,. \tag{3.24}$$

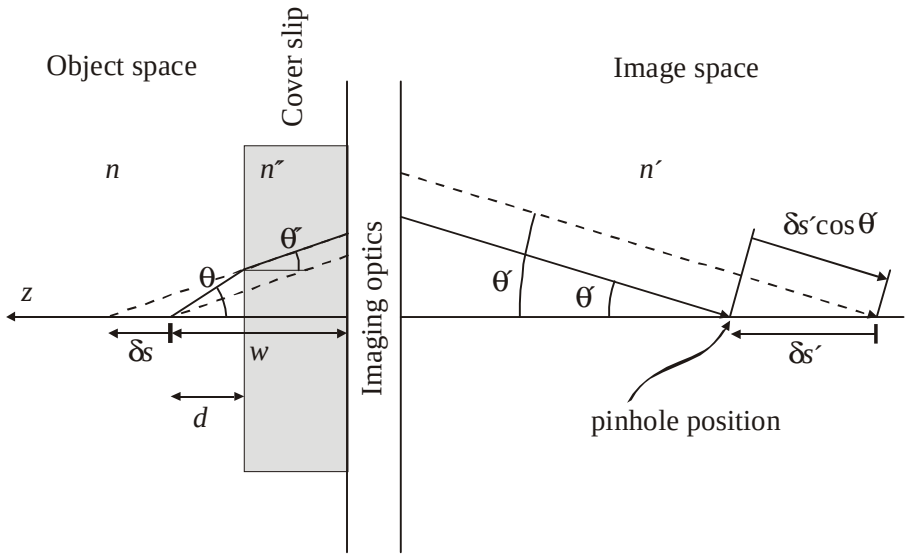

Fig.12: Geometry of imaging through an oil immersion objective which is focused into solution a distance d above the coverslip's surface. Dashed lines represent light ray propagation if the refractive index of the solution would be equal to that of the immersion oil.

The cross-point between optical axis and the corresponding light ray in image space is shifted by a value $\delta s' = M^2 \delta s$ *closer towards* the objective. From a wave optics point of view, this corresponds to a phase shift Δ,

$$\frac{\Delta}{k_0} = n\delta s - n'(1-\cos\theta')\delta s' + (d+\delta z)\left(\frac{n}{\cos\theta} - \frac{n''}{\cos\theta''}\right), \tag{3.25}$$

of the θ'-plane-wave-component with respect to the same component under perfectly matched imaging conditions. Again, the field amplitudes are given by Eqs.(3.17,3.19,3.20) with the tensor components $G_{ab}^{E,B}$ multiplied by the additional factor $\exp(i\Delta)$. However, the integration limit $\theta'_{\max}$ is now determined by the angle of total internal reflection, not by the numerical aperture of the objective:

$$\theta'_{\max} = \arctan\left[\frac{n}{M\sqrt{n''^2 - n^2}}\right]. \tag{3.26}$$

Until now, only emitters located exactly on the optical axis were considered. To obtain the field amplitudes for a dipole located off the optical axis, one uses again the aplanatic property of the objective. The field amplitudes in image space for a dipole shifted away from the opti-

cal axis by a vector $\vec{\rho}$ are given by the field distributions for the on-axis dipole, but shifted by the vector $\vec{\rho}' = -M\vec{\rho}$. Thus, Eqs.(3.17,3.19,3.20) together with Eq.(3.23) or Eq.(3.25), respectively, contain full information about the electric and magnetic field amplitudes in image space for an arbitrary dipole position in object space. Finally, the light detected by a detector behind the confocal aperture is proportional to the integral of the Poynting vector, $\vec{S} = (c/8\pi)(\vec{E} \times \vec{B}^*)$, over the aperture opening.

It should be noted that the considerations concerning imaging through the oil immersion objective are valid only for dipoles located in solution far away (several wavelengths) from the solution/glass interface, where the dipole emission can be considered to be that of a free dipole within a homogeneous environment. If the dipole comes into wavelength distance with the interface, coupling of evanescent modes into the glass start to play an important role, significantly changing the imaging conditions (for a detailed discussion of that case, see Ref.[18]). However, in FCS applications, fluorescence is usually detected several micrometers above the glass surface.

3.3.2 Numerical results and discussion

Numerical calculations were performed for two different objectives: a water immersion objective with 1.2 NA and $66\frac{2}{3}$ magnification, and an oil immersion objective with 1.4 NA and 100 times magnification. In both cases, an emission wavelength of 670 nm was assumed, corresponding to the emission maximum of standard dyes that are excitable by diode lasers or HeNe lasers at 633-35 nm. The circular confocal aperture was assumed to have a diameter of 100 μm, being positioned in the image plane of the objective.

A remarkable feature of the dipole-imaging-CEF is that, for a perfectly centered circular confocal aperture, it is independent on the dipole's orientation within the *xy*-plane (see Fig.10). Thus, one has only to distinguish between dipole orientations perpendicular and along the optical axis.

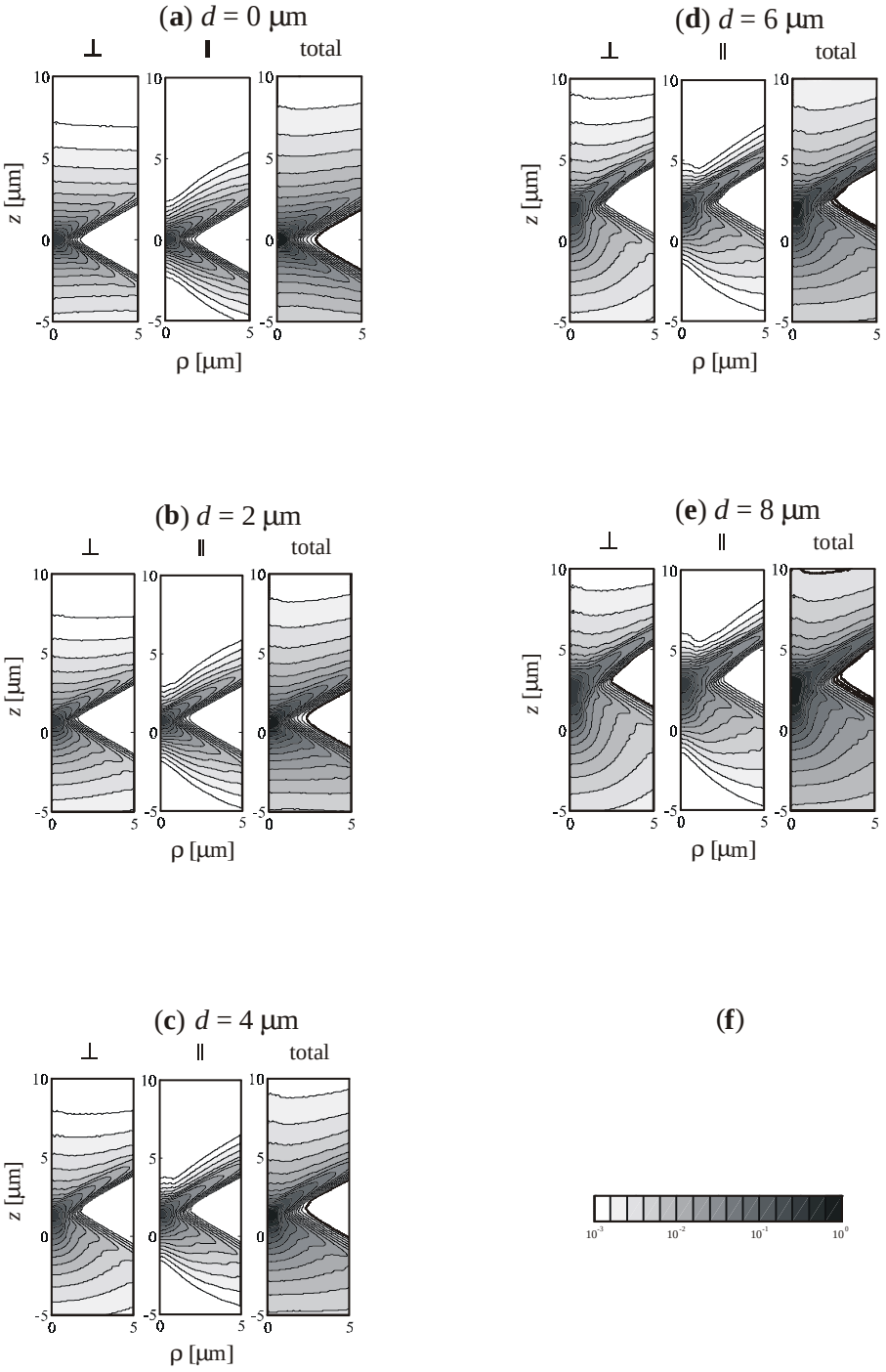

Fig.13: CEF for emitting dipoles at 680 nm emission wavelength CEF imaged by a water-immersion objective (NA = 1.2, magnification $66\frac{2}{3}$). Shown is the light collection efficiency in dependence on the dipole position (ρ, z), where ρ is the distance from the optical axis, and z the position along the optical axis. Left panel shows the CEF for dipoles oriented perpendicular to the optical axis z, middle panel that for dipoles oriented along the optical axis, and right panel that for isotropically oriented dipoles. The different subplots show the results for different cover slide-thickness deviations of (a) 0 µm, (b) 2 µm, (c) 4 µm, (d) 6 µm, and (e) 8 µm. Subplot (f) shows the corresponding grayscale coding of the CEF values. Notice the logarithmic grading of levels of equal efficiency. For every value of d, the CEFs were normalized by the maximum value of the isotropic-emitter CEF (right panel).

Fig.13 shows the results of a series of CEF calculations for a water-immersion objective, with the excess value d of the cover slide's thickness increasing from zero to eight micrometers. The results for negative values of d (i.e. the cover slide being too thin) look similar, but being reflected at the focal plane $z = 0$. The figures show the CEF in dependence of the dipole location in object space, whereas the left hand panels show the CEF for dipole orientation perpendicular to the optical axis (transversal orientation, $\perp$), the center panels that for dipole orientation along the optical axis (axial orientation, ||), and the right hind panels that for a random dipole orientation (isotropic emitter). The latter is important when studying molecules with rotational diffusion times much faster than the fluorescence decay time, whereas the first two results are important when dealing with slowly rotating molecules. Even a slight excess of the cover slide's thickness from its nominal value causes severe aberrations, which will have a strong impact on the temporal behavior and overall shape of a FCS curve.

Figs.14 show the similar results for an oil immersion objective, for values of the focus distance d above a surface increasing from 2 to 10 μm. The calculations start with a distance d of 2 μm for which evanescent modes of the dipole emission can be safely neglected. Again, aberrations start to show up or for even modest values of d.

For both the water and oil immersion objective, an interesting effect is that the maximum of the CEF for dipoles with transversal orientation is slightly shifted with respect to the maximum of the CEF for axial dipole orientations. This is important when studying molecules with rather slow rotational diffusion.

In conclusion, it should be emphasized that the presented calculations are exact for a perfectly aplanatic imaging system. In that case, the knowledge of only the numerical aperture and overall magnification of the imaging system is enough for performing the CEF calculations. Taking into account additional aberration effects inherent to the objective itself requires the knowledge of its complete structure, or the precise knowledge of its (polarization dependent) point spread function. Exact information about the structure on an objective is rarely provided by the manufacturers, and precisely measuring the point spread function of an objective is a rather difficult task. Thus, the CEF calculations presented here are a compromise between relative simplicity and maximum correctness.

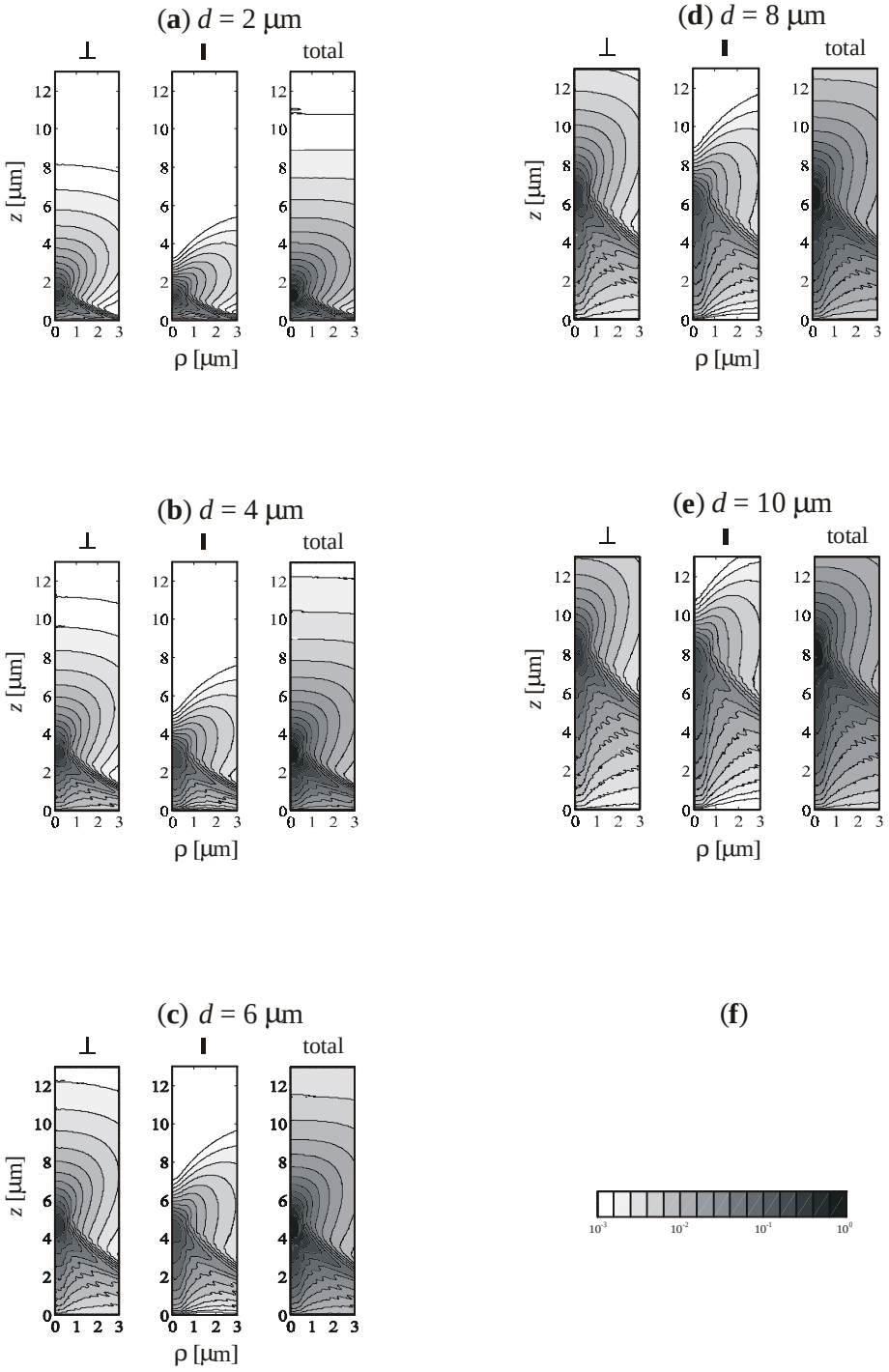

Fig.14: Same as Fig.13, but for an oil-immersion objective (NA = 1.4, magnification 100). The different subplots show the results for different values d of the focus depth of (a) 2 µm, (b) 4 µm, (c) 6 µm, (d) 8 µm, and (e) 10 µm. Grayscale coding is the same as in Fig.13f, and the CEFs were again normalized by the maximum value of the isotropic-emitter CEF (right panel).

3.4 Ab-initio modeling of fluorescence correlation spectroscopy experiments

Usually, when evaluating measured FCS data, a simplified model is applied which rests on the rather unrealistic assumption of an ellipsoidal detection volume. Although it is well-known and accepted that the ellipsoidal detection volume geometry is a rather rough approximation of the real situation, the model Eq.(3.15,3.16) remain very popular for fitting experimental FCS curves. This has two reasons: Firstly, the striking simplicity of the expressions in Eq.(3.15,3.16), and, secondly, the high fidelity (uniformly low deviation between fit and data) achievable with this simplified model. In general, this is an unnecessary assumption, because both the collection efficiency function and excitation intensity distribution can be calculated exactly as demonstrated in section 3.3. Knowing both functions, the fluorescence correlation function can be found by numerically solving a diffusion equation with special initial conditions. This approach promises (i) absolute determination of diffusion coefficients; (ii) absolute determination of analyte concentrations; (iii) complete consideration of aberrational effects.
This section presents a detailed theoretical description of this new approach, numerical results for the fluorescence correlation function and application to experimental measurements.

3.4.1 Theory

Although the model Eq.(3.15) is remarkably successful in fitting measured autocorrelation curves (see also below), the physical meaning of the parameters a and b is rather obscure, because the convolution of the actual excitation intensity distribution with the actual CEF is much more complicated than as given by Eq.(3.14). This is especially the case for oil immersion objectives with high numerical aperture, where the refractive index mismatch between the immersion oil and the sample solution can cause significant optical aberrations. However, using such oil-immersion objectives for FCS measurements is very convenient, due to their broad availability and usually excellent optical quality.
There is no necessity to use Eq.(3.14) for modeling autocorrelation functions. Both for water-immersion and oil-immersion objectives, exact wave-optical calculations of the excitation intensity distribution and the CEF are available (see section 3.3). Knowing these functions explicitly, the autocorrelation function can be calculated by using Eq.(3.10), whereby it is useful to recognize that the integral

$$F(\vec{r},t)=\int d\vec{r}_0 G(\vec{r}-\vec{r}_0,t_0)U(\vec{r}_0)E(\vec{r}_0) \tag{3.27}$$

is the solution of the diffusion equation,

$$\frac{\partial F}{\partial t}=D\Delta F\ , \tag{3.28}$$

with initial condition $F(\vec{r},0)=U(\vec{r})E(\vec{r})$. Thus, firstly, this solution at a given time t is calculated, and secondly, the time dependent part of $g(t)$ by convolving $F(\vec{r},t)$ with $F(\vec{r},0)=U(\vec{r})E(\vec{r})$ and multiplying the result by $(\phi_f\sigma)^2 c$.

If the excitation intensity distribution and the CEF are invariant with respect to rotations around the optical axis, i.e. both are functions of the variables ρ and z alone, (ρ,ϕ,z) being cylindrical coordinates with z along the optical axis, the calculation of $g(t)$ can be simplified further. Then, explicit integration over the angular variable ϕ reduces Eq.(3.27) to a two-dimensional integral,

$$F(\rho,z,t)=\exp\left[-\frac{\rho^2}{4Dt}\right]\int_0^\infty d\rho_0\,\rho_0\int_{-\infty}^{\infty}dz_0\,\frac{2\pi U(\rho_0,z_0)E(\rho_0,z_0)}{[4\pi Dt]^{3/2}}\cdot J_0\left(\frac{i\rho\rho_0}{2Dt}\right)\exp\left[-\frac{\rho_0^2-(z-z_0)^2}{4Dt}\right], \tag{3.29}$$

where J_0 is the Bessel function of the first kind and zero order, and $i=\sqrt{-1}$. Thus, one finally has

$$g(t)=(\sigma\phi_f)^2\left[c\int_0^\infty d\rho\,\rho\int_{-\infty}^{\infty}dz U(\rho,z)E(\rho,z)F(\rho,z,t)+\left[c\int_0^\infty d\rho\,\rho\int_{-\infty}^{\infty}dz U(\rho,z)E(\rho,z)\right]^2\right]. \tag{3.30}$$

3.4.2 Experimental

The experimental set-up is described in detail in part 2 (Fig.8). The TTTR mode was used for continuously and separately registering the detected photons of both SPADs with 100 ns tem-

poral resolution. From these raw data, the autocorrelation curves were calculated on a personal computer by cross-correlating photons from the two different SPADs. Such a cross-correlation procedure is necessary for preventing that SPAD afterpulsing distorts the actual autocorrelation curve at short autocorrelation times as discussed in section 3.2.
Measurement of FCS curves was repeated using confocal apertures with five different diameter values of 50, 100, 150, 200 and 300 μm. The quality and diameter value of every pinhole was checked by video-microscopy. Every FCS measurement lasted 60 seconds. As the fluorescent dye the rhodamine derivative JA167 [31][19] was chosen, being well excitable at the 635 nm wavelength of the used diode laser, and not showing any discernable triplet or other short-time photophysical dynamics. In the case of the 50 μm -pinhole, a $3 \cdot 10^{-9}$ M solution of that dye in purified water was used, a drop of which was placed on top of a cleaned cover slide (Menzel, 170 μm thickness). For all other pinhole diameters, the dye concentration was $5 \cdot 10^{-10}$ M. Vertical focus position was adjusted by firstly focusing the laser directly onto the cover slide's surface, which was checked by imaging the back-reflected laser light with a CCD-chip, and secondly moving the whole objective vertically with a piezo-actuator (PIFOC, P-731-20, Physik Instrumente). In this way, focus position was always set at 10 μm above the glass surface. For every measurement, the pinhole position was adjusted in three dimensions for obtaining maximum fluorescence signal, assuring optimum axial and image plane alignment. Laser excitation power was set to 300 μW. Assuming an excitation focus diameter of ca. 0.5 μm, and for the dye's absorption cross section of $\sim 10^{-16}\,\mathrm{cm}^2$, one estimates the excitation rate to be $\sim 10^{7}\,\mathrm{s}^{-1}$, which is more than one order of magnitude below optical saturation (fluorescence lifetime of JA167 is ~3 ns). All experiments were performed at room temperature.

3.4.3 Results and discussions

In correspondence with the experimental conditions, the CEFs for an oil immersion objective with 1.4 NA and 100× magnification and for pinhole diameters of 50, 100, 150, 200 and 300 μm were calculated, together with the excitation intensity distribution generated when focusing a laser beam through the same objective. In the calculations, it was assumed that the excitation focus was moved by 10 μm away from the cover slide's surface into the solution. Calculations were performed for an excitation wavelength of 635 nm, and a center fluorescence emission wavelength of 670 nm. The convolutions of the excitation intensity distribu-

tion with the five different CEFs are calculated according to section 3.3 (see Fig. 14). Using these convolutions, autocorrelation curves $g(t)$ were calculated according to Eqs.(3.29,3.30), whereas the diffusion coefficient *D* was arbitrarily set to a numerical value of $D_{\text{model}} = 10^{-5}\ \text{cm}^2/\text{s}$. The value of the model concentration c was chosen arbitrarily, and all calculated curves were subsequently normalized by their zero-time value g_0.

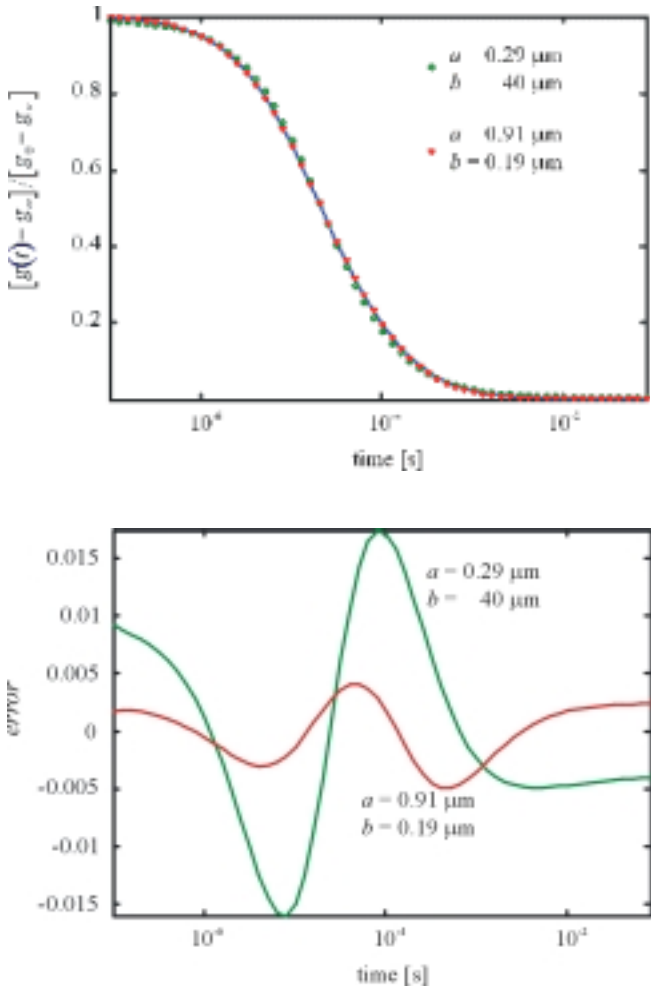

Fig. 15: (a) Result of fitting the *ab-initio* autocorrelation curve for the 100 m-pinhole with the standard model as given by Eq.(3.15). The two fitted curves correspond to a parameter ratio a/b of larger and smaller than one, respectively. (b) Deviation of the fitted curves (standard model) from the *ab initio* calculated model curve. Notice the very good fit quality in terms of small deviations between fit and model curves.

In a first step it was studied how the obtained *ab-initio* model curves are fitted by the standard model as given by Eq.(3.15). Least-square fits of the standard model, Eq.(3.15), against the calculated autocorrelation curves were performed. Because the diffusion constant is exactly

known, the fit results can be used to obtain the two parameters *a* and *b* of the standard model, and subsequently a value for the effective detection volume as $\pi^{3/2}a^2b$. The fit results are shown in Table 1, where the exact effective volume as determined by Eq.(3.13) is also given.

Table 1: Results of fitting the standard model Eq.(3.15) to the *ab initio* calculated autocorrelation curves, for different diameter values $d_{aperture}$ of the confocal pinhole. Listed are the two half-axes a and b describing the usually assumed Gaussian detection volume geometry Eq.(3.14), together with the resulting effective detection volume. The last volume lists the actual detection volume, as defined by Eq.(3.13). During the fitting, the ratio a/b was forced to stay below one, corresponding to the actual situation that the detection volume has larger extension along the optical axis than perpendicular to it.

$d_{aperture}$ [μm]	a [μm]	b [μm]	$\pi^{3/2}a^2b$ [μm^3]	v_{eff} [μm^3]
50	0.23	5.7	1.67	0.83
100	0.29	40	194	2.11
150	0.33	86	537	3.85
200	0.37	123	933	6.05
300	0.41	74	689	11.2

Fig.15a displays the calculated autocorrelation curve together with the standard-model fit for the case of the 100 μm -pinhole; the corresponding deviation between autocorrelation and fit is shown in Fig.15b. As can be seen, the standard model fits the calculated autocorrelation remarkably well, although the corresponding values of *a*, *b* and the effective volume are far from being physically reasonable. When performing the least-square fits, the value of *a* was enforced to be smaller than that of *b*, corresponding to the real physical situation that the detection volume extends farther along the optical axis than perpendicular to it. In a second series of fitting the standard model to the calculated autocorrelation curves, the ratio a/b was allowed to reverse. For the 100 μm -pinhole, the corresponding fit result is also displayed in Fig.15, and the determined parameter values *a*, *b* and $\pi^{3/2}a^2b$ are given in Table 2. Surprisingly, the fit quality for the ”wrong” parameter ratio is better than that for the physical” parameter ratio (see Fig.15b), and one obtains values of the effective volume that are much

closer to reality. However, neither the fit results for the ”physical” nor the ”wrong” parameter ratio will allow for a correct quantitative determination of actual dye concentrations and/or diffusion coefficients, although the visually excellent fit quality of the standard model is indeed alluring.

Table 2: Results similar to Table 1, but allowing the ratio a/b to become larger than one.

$d_{aperture}$ [μm]	$a\,[\mu m]$	$b\,[\mu m]$	$\pi^{3/2}a^2 b\,[\mu m^3]$	$v_{eff}\,[\mu m^3]$
50	0.55	0.16	0.28	0.83
100	0.91	0.19	0.89	2.11
150	1.42	0.20	2.27	3.85
200	2.00	0.21	4.81	6.05
300	3.32	0.23	14.3	11.2

Finally, the calculated autocorrelation curves were used for fitting the experimental measured FCS curves, which will be denoted by $y(t)$. Fitting the model curves against the experimental results is done in a straightforward way by an affinity transformation. By inspecting the r.h.s. of Eq.(3.29), it can be seen that the autocorrelation function is invariant with respect to rescaling the time axis, as long as the product Dt is kept constant. Furthermore, as already discussed in the Theory section, the difference $g(t)-g_\infty$ is directly proportional to the concentration *c*. Thus, the following fitting equation is used,

$$y(t) = A + B\frac{g(\alpha t)-g_\infty}{g_0 - g_\infty}, \tag{3.31}$$

containing the three fit parameters *A*, *B* and α. From these fit parameters, the diffusion coefficient and the dye concentration are calculated as

$$\begin{aligned} D &= D_{\text{model}}/\alpha, \\ c &= \frac{A}{v_{eff} N_A B}, \end{aligned} \tag{3.32}$$

where D_{model} is the diffusion coefficient used in the numerical model calculations ($D_{\text{model}} = 10^{-5}\,\text{cm}^2/\text{s}$), v_{eff} is determined by Eq.(3.13), and N_A denotes the Loschmidt-Avogadro number, $N_A = 6.0221367 \cdot 10^{23}$. The fit results for the five pinholes used are presented in Table 3; fitted against experimental curves are shown in Fig.16.

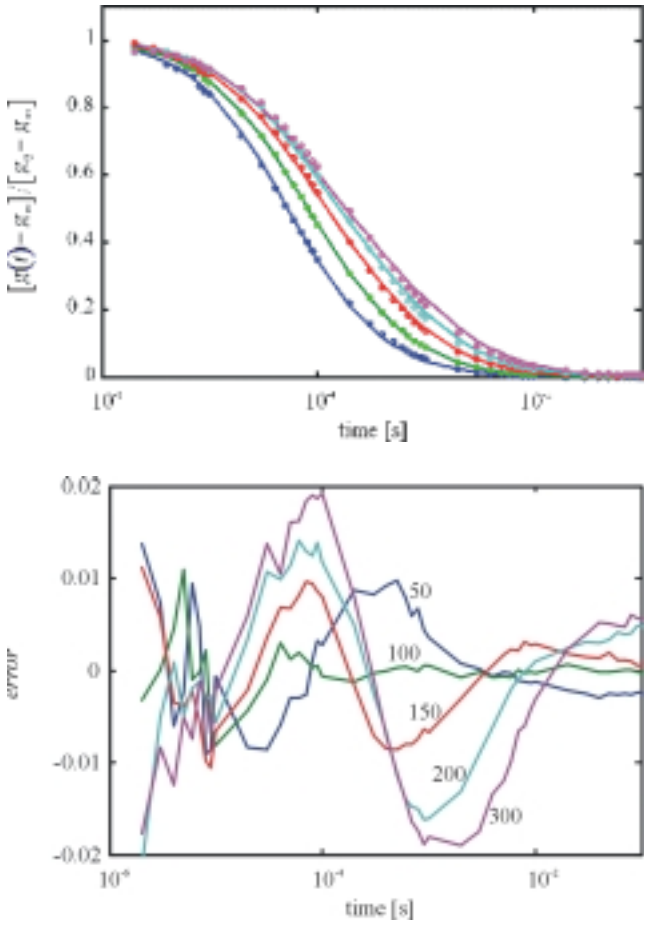

Fig.16: (a) Results of fitting the *ab initio* calculated against the experimentally measured autocorrelation curves. For better comparison, all curves are normalized by their (extrapolated) values at zero time. From left to right, curves correspond to pinhole-diameter values of 50, 100, 150, 200 and 300 μm, respectively. (b) Deviations between fit and experiment. Numbers next to the curves indicate corresponding pinhole diameter.

Experimental data are best fitted in the case of the 100 μm -pinhole, with increasing deviations for larger and smaller pinhole diameters. Also, derived concentration values are closest to the prepared values for the two smallest pinhole diameters. The derived values for the diffusion coefficient are largest for the two smallest pinhole diameters, but remaining all in a range where one would expect to find the diffusion coefficient of a rather small dye molecule in water. One reason for the decreasing quality of the fitting for larger pinhole diameters may

be the increasing influence of optical aberrations of the used objective. All optical calculations, which form the basis of the *ab-initio* fitting procedure, are relying on the core assumption that the imaging objective is perfectly aplanatic. Although modern oil-immersion objectives as the one used here come very close to that assumption, they can be perfectly corrected at only some discrete wavelengths (usually the blue and green visual region). In the present work, fluorescence excitation and detection is done at the red edge of the visible region, so that possibly optical aberrations are no longer negligible. Additionally, all calculations are only correct for perfect alignment of all optical elements of the measurement system, especially for perfect positioning of the confocal aperture. Perfect confocal alignment of the aperture becomes more and more challenging for decreasing values of aperture diameter. Thus, it may be that the aperture is not perfectly on-axis for the smallest pinhole diameter of 50 μm. Alignment of the pinholes along the optical axis was done by searching for the pinhole position yielding the highest fluorescence count rate, a method which has also a limited accuracy only. Another problem is the difficulty of preparing samples with the exact dye concentrations at the low concentration values around $10^{-10}\,\mathrm{M}$ as used in the performed experiments, although surface coating with bovine serum albumine (BSA) was applied for preventing unspecific adsorption of dye to the surfaces of the glass ware used during sample preparation.

Table 3: Results of fitting the *ab intio* calculated autocorrelation curves to the experimental ones. The second column lists the prepared dye concentration of the measured sample.

$d_{aperture}$ [μm]	Dye concentration $[10^{-9}\,\mathrm{M}]$	Measured dye concentration $[10^{-9}\,\mathrm{M}]$	Measured diffusion coefficient $[10^{-6}\,\mathrm{cm}^2/\mathrm{s}]$
50	3	2.970	2.52
100	0.5	0.527	2.62
150	0.5	0.199	2.23
200	0.5	0.293	2.05
300	0.5	0.479	2.19

The presented results have to be understood as a first attempt to apply a complete modeling of FCS experiments to the fitting of experimental data. The advantage of the method is that it does not need the adjustment of any empirical parameters, that it is applicable even to ”no-

perfect" experimental conditions such as imaging with an oil-immersion objective deep in solution, and that it directly yields absolute values of the dye's diffusion coefficient and concentration. The method can easily be generalized to include more complex photophysical behavior such as triplet state dynamics, photobleaching, or fluorescence occurring from multiple states. Also, possible misalignments of the measurement system can be taken into account. Both topics will be addressed in the future and will be presented elsewhere. It should be emphasized that, although the wave optical calculations of the excitation intensity distribution and the CEF and the subsequent calculation of the autocorrelation curves are rather complex, they have to be calculated only once for a given excitation and detection geometry. Fitting the curves to experimental data is done by a simple and very fast affinity transformation as given by Eq.(3.31). Even in the case of several fluorescent dyes, the resulting compound autocorrelation function is only a superposition of several such affinity-transformed model curves. This is very important for practical applications of the presented method.

3.5 Brightness and lifetime analysis of novel diode laser compatible fluorophores

There is growing interest in the use of fluorescent probes for the detection of biological compounds like proteins or DNA, especially because of the development of inexpensive long-wavelength excitation sources like diode lasers in the region over 630 nm, but also in context with fluorescent single molecule detection. The main advantage of using longwave light sources and labels is the decreased auto-absorption and auto-fluorescence, particularly beyond 600 nm, from cells and tissue because the optical window of blood and other biological material is in the range of 650 to 700 nm [20,21].

Cyanine dyes are widely used labels for proteins and DNA because they show valuable spectral properties like high molar absorbance, high quantum yield, and a great variety in their absorption and emission wavelengths, and because they can be tuned to the desired wavelengths by varying the heterocyclic nucleus or the number of double bonds in the polymethine chain [22-24]. The new labels characterized here belong to the class of the cyanine dyes (in the case of RB-627, RB-646, and RG-702) or to the closely related class of squaraine dyes (RB-634, RB-661, RG-667). They are water-soluble either due to the presence of (anionic) sulfo groups (like in RB-634 or RG-667), or because of being quaternized (cationic) azaheterocyclic compounds, e.g. in the case of RG-702. More details about their chemical structure and synthesis can be found in Ref. [25].

3.5.1 Fluorescence intensity distribution analysis

Long-wavelength excitable dyes are preferred in fluorescent single molecule detection (SMD) because of the lower background fluorescence of a generally weak signal and because they can be excited by diode lasers. Individual molecules can be detected at room temperature by a variety of methods including FCS and WFM. However, in confocally based detection in solution fluorescent molecules diffuse randomly in all three dimensions within the sample, e.g. each time they become visible, they do not necessarily pass through the center of the focus. In addition, if the sample consists not only of a single species the situation is even more complicated: An event in which a relatively bright molecule enters the periphery of the laser beam only briefly cannot be distinguished from an event in which a dark molecule passes through the focus, because they leave identical traces in terms of detectable photon counts. The expression bright molecule or better the *specific brightness* q of the molecule refers to a molecular quantity, which is proportional to the molecular absorption cross section and to the fluorescence quantum yield.

Nevertheless, fluorescent species with different specific brightness can be distinguished, by collecting a statistical distribution of the number of photon counts at time intervals of given length. The experimental distribution of number of photon counts at time intervals of 40 μs and data collection time of 120 s is shown in Fig. 17. In these experiments, we measured pure solutions of the different novel cyanine dyes. In order to avoid trapping of molecules into the triplet excited state the measurements were carried out under moderate excitation intensities. The goal of these experiments is to compare the different novel dye molecules with respect to the well known cyanine dye Cy5.

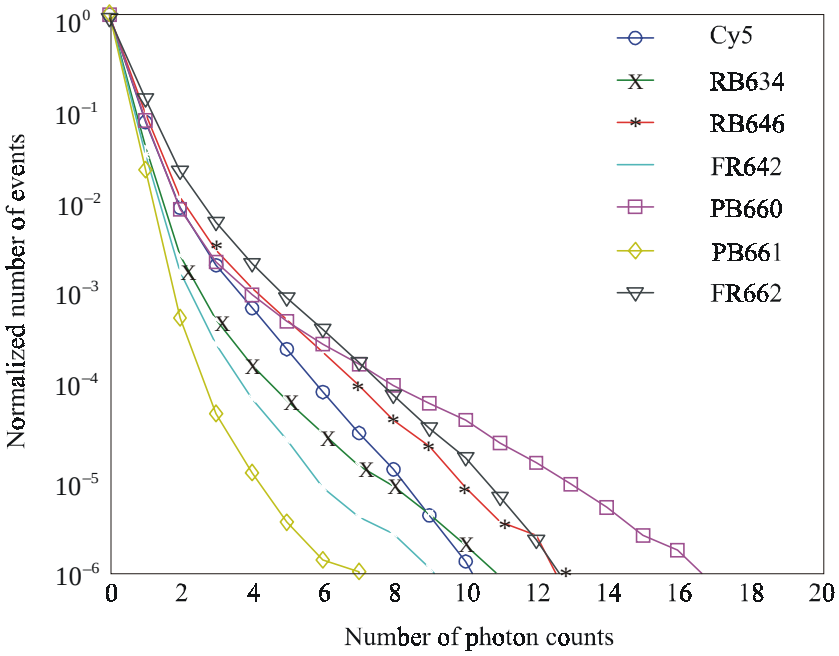

Fig.17: Experimental distributions of the number of photon counts for a time window of 40 μs . The different symbols (circles, squares, etc.) correspond to the solutions of seven different dyes.

In order to compare the performance of the novel diode laser compatible dyes in perspective of their specific brightness, the so called fluorescence-intensity distribution analysis (FIDA) can be applied [26]. The advantage to use fluorescence brightness information is that in many cases of practical interest, different sorts of fluorescing molecules have rather similar diffusion constants but differ significantly by their fluorescence emission intensities. Thus, FIDA is an interesting approach when desiring to analyze mixtures of molecules with nearly equal diffusion constants but differing values of absorption cross section times fluorescence quantum yield. The theory of FIDA is introduced in Ref. [26].

Table 4: Specific brightness of the novel dyes in the carboxylic acid form in aqueous solution.

dye	Cy5	RB634	RB646	FR642	PB660	PB661	FR662
q	1.0	1.3	1.2	0.9	1.65	0.65	1.3

The respective data of a simple fluorescence intensity distribution analysis of the seven novel diode laser compatible dyes are compiled in Table 4. The specific brightness of the dyes RB646, PB-660 and PB-662 are higher compared to the reference dye Cy5.

3.5.2 Lifetime analysis

From the beginning of SMD in liquids, the goal was not only to detect single molecules but also to distinguish between different sorts of molecules. A straightforward way for doing this is to detect not only the arrival of single photons, but to simultaneously record their physical properties. Fluorescence photons emitted by a molecule have two physical properties: The energy respectively wavelength and the time of emission after excitation.

The TCSPC instrumentation of the confocal microscope was used to determine the fluorescence lifetime of the dyes. Specifically, the traces of the decay profile of the fluorescence of dyes RB-627, RB-634, RB-646, PB-661 FR-642, PB-660, FR-662 and RG-667 have been recorded for aqueous solutions.

In TCSPC, the molecule's fluorescence is excited by a train of short laser pulses with high repetition frequency. Then, with the help of a fast single-photon detector and high-speed processing electronics, the times of detection of the fluorescence photons with respect to the times of the exciting laser pulses are measured. By repeating this single photon counting a sufficiently large number of times, a histogram of arrival times is build up.

The observed fluorescence intensity $R(t)$ at time *t* is generally given by

$$R(t) = \int_{-\infty}^{\infty} dt'\, F(t-t')K(t') \tag{3.33}$$

where $F(t)$ is the time profile of the fluorescence decay of the studied atomic or molecule system, and $K(t)$ is the so called instrumental response function (IRF), containing information about the time profile of the laser excitation and the time characteristics of the whole measurement system. It is assumed, that the integration begins from minus infinity, and that $K(t)$ is a periodic function with a period equal to the repetition time of the excitation. This takes into account the fluorescence emanating from earlier excitation pulses, which is important when dealing with decay times of the order of the repetition time between two excitation pulses.

In general, the measured values of $R(t)$ contain statistical errors, making the inversion of the integral equation an ill-posed problem.

In practice one deals with discrete numbers of photons R_i in a finite number of time channels $\{t_j - \Delta t/2, t_j + \Delta t/2\}$ with center time t_i and channel width Δt instead of a continuous function $R(t)$. For sufficiently small channel width Δt, $R(t)$ can then be rewritten as

$$R_k = \sum_{j=0}^{\infty} \sum_{i=1}^{M} \alpha_i \exp\left(-\frac{j\Delta t}{\tau_i}\right) K_{k-j} \tag{3.34}$$

where R_i and K_i are the number of counts and the instrumental response function value for the *k*th time channel, respectively. For fitting multi-exponential decay curves to experimental data, one tries to minimize a given error function. The most common error function used is the least-squares deviation χ^2,

$$\chi^2 = \sum_{k=1}^{N} \frac{1}{\sigma_k^{\,2}} \left\{ F_k - \sum_{j=-\infty}^{k} \sum_{i=1}^{M} \alpha_i \exp\left[-\frac{(k-j)\Delta t}{\tau_i}\right] K_j \right\} \tag{3.35}$$

where the summation over *k* runs over all *N* channels of the TCSPC curve, and the σ_k are the mean square deviations of the photon counts in the *k*th channel. Since this function depends non-linearly on the parameters τ_i, one normally applies non-linear minimization methods, like the Nelder-Meade simplex algorithm [27] or the Marquardt method [28]. Unfortunately, these iteration methods are very sensitive with respect to the initial guess values of the parameters, and can be very time consuming for bad initial guesses or larger numbers of exponential components. In Ref.[29] a convolved autoregressive model for the fit of multi-exponential decay curves was discussed: A quasi-quadratic dependence of the error function upon the fit parameter is derived, allowing the application of fast and powerful methods of linear squares minimization. Fig.18 gives a typical example.

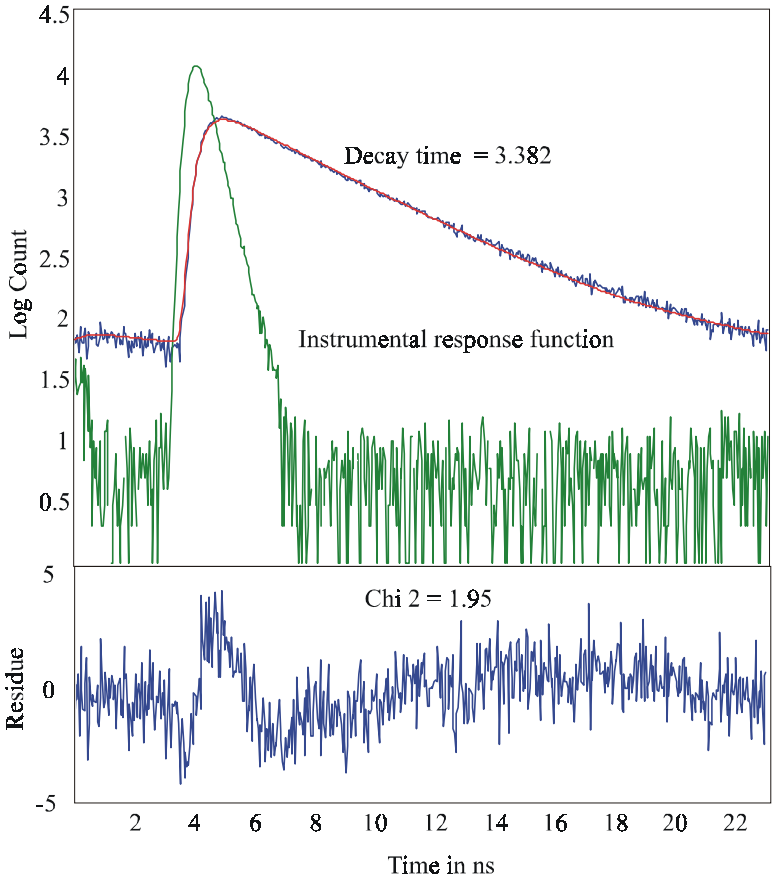

Fig. 18: Fluorescence intensity of the dye FR662 versus delay time from the excitation pulse and fit using a one-component exponential decay. In addition, the instrumental response function of the detection system is plotted. The residuals are shown in the lower panel. The total χ^2 value is 1.95.

All measurements were carried out in pure water. The dye concentration of the stock solution was checked via the absorbance of the solution. The time-resolved fluorescence decay data of the different dyes were measured at a concentration of 10 nM. Stock solutions (1 µM) were used immediately after preparation. The solutions for single-molecule experiments were prepared by diluting the stock solutions with water to the required concentration, typically as little as 100 pM. The samples then were transferred onto a microscope cover glass fixed to a microscope stage and additionally covered by a second cover glass to avoid evaporation of the sample.

Table 5: Spectral properties and fluorescence lifetime of the novel dyes in the carboxylic acid form in aqueous solution.

Dye	Abs. max. [nm]	Em. max. [nm]	ε [l/molcm]	τ [ns]	χ^2 values	Factors
Cy5	646			0.98	1.89	
RB-627	627	650	105.000	0.17, 1.4	4.73	0.87, 0.13
RB-634	634		180.000	0.51, 2.35	1.33	0.86, 0.14
RB-646	646	666	180.000	0.65, 1.6	1.05	0.70, 0.30
FR-642	642			0.58, 2.55	1.6	0.95, 0.05
PB-660	660			2.78	1.56	
PB-661	661	680	140.000	0.45, 1.7	1.13	0.74, 0.26
FR-662	662			3.38	1.95	
RG-667	667		120.000	0.95, 2.9	1.14	0.54, 0.46
RG-702	702	718	110.000			

In all cases, one or two decay times were found to describe the profiles adequately. The short-decaying components decay within typically 0.2 to 0.9 ns, with weighing factors ranging from 0.54 to 0.97. The longer components decay within 1.4 to 2.9 ns, but their relative contributions usually are much smaller. The respective data are compiled in Table 5. The decay times of PB-660 and PB-662 deserve special attention. The best fit of their decay profile is achieved with a monoexponential decay model, delivering a relatively long decay time of 2.78 and 3.4 ns respectively. In Fig.19 the TCSPC data of all detected photons for Cy5 and FR-662 were summed up and normalized. The normalized decay profiles of the dyes demonstrate that the favorable spaced lifetime of the three dyes can be exploited in time-resolved multiplex techniques.

Fluorescence bioassays have become extremely popular in the past years, since they are sensitive, selective, and versatile. Parameters that can be measured include fluorescence intensity, decay time, quenching efficiency, polarization and energy transfer. The N-hydroxysuccinimide ester form of the dyes RB-646, FR-642, PB-660, PB-661 FR-662, FR-

667 and FR-702 were conjugated to human serum albumin (HSA) or to anti-HSA in the case of RB-634, to give the labeled proteins listed in Table 6. Table 6 summarizes their spectral and decay time properties.

Table 6: Fluorescence lifetime of the conjugates with HSA and anti-HSA in aqueous solution.

Dye/Conjugate	τ [ns]	χ^2	Factors	DPR
PB-646/HSA	0.43, 1.60	1.15	0.76, 0.24	
FR-642/HSA	0.36, 1.80	1.64	0.83, 0.17	4.4
PB-660/HSA	0.44, 2.40	1.23	0.70, 0.30	1.9
PB-661/HSA	0.44, 2.40	1.32	0.80, 0.20	2.7
FR-662/HSA	0.60, 3.40	1.16	0.53, 0.47	1.5
FR-667/HSA	0.60, 2.68	1.29	0.47, 0.53	1.7
FR-702/HSA	0.49, 3.50	1.25	0.49, 0.51	1.0
RB-634/anti-HSA	0.31, 2.60	1.26	0.86, 0.14	4.4

The degree of labeling (molar dye-to-protein ratio, DPR) for each dye-protein conjugate was calculated as the molarity of dye divided by the molarity of protein. The molar mass of HSA was assumed to be 65 kD, that of anti-HSA 160 kD. The dye concentration of the conjugate was determined according to Lambert-Beer's law from the absorbance of the dye at the absorption maximum, assuming that there is no difference in the absorbance of free dye and conjugated dye.

In all cases, two decay times were found to describe the fluorescence decay profiles adequately. The short-decaying components decay within 0.31 to 0.60 ns, with weighing factors ranging from 0.47-0.86. The longer components decay within 1.60 to 3.5 ns, but their relative contributions usually are much smaller.

3.6 Combining time correlated single photon counting and fluorescence correlation spectroscopy

One drawback of the FCS is its inability to distinguish between molecules which have similar diffusion constants. The FCS curve for a mixed solution of more than a single fluorescent molecular species has a rather complex structure and does not allow for a simple extraction of e.g. the concentrations of the different species. A way out of this problem is to measure the fluorescence within several detection channels at different wavelengths. This allows not only to separately determining the FCS curves for different molecular species, but offers also the possibility to perform a cross-correlation analysis. Especially the latter has proved to be very fruitful in ultrasensitive detection and monitoring of molecular binding/unbinding processes and chemical reaction kinetics [30-36]. The disadvantage of dual- or multi-color FCS is its experimental complexity, due to the necessity of exactly aligning the femtoliter-sized excitation/detection volumes at several detection wavelengths. Ever present chromatic aberration of real optics makes this a very challenging task.
Here, a new FCS technique is theoretically proposed and experimentally demonstrated, which uses the differing fluorescence decay characteristics of different dyes for separating the FCS curves of different dyes. The method will also be applicable to cross-correlation experiments and is thus a direct alternative to the dual-color FCS technique cited above.

3.6.1 Theory

The standard theory of FCS is usually derived on the basic assumption that the fluorescence detection efficiency function $V(\vec{r})$ has an ellipsoidal shape as defined in Eq.(3.14). The values of a and b define the spatial distribution for the fluorescence collection efficiency and are determined by the degree of focusing of the exciting laser beam and the numerical aperture of the objective lens. The value of κ is determined by the overall optical throughput of the light collection and detection, and by the intensity of the excitation light. For a single molecular species with only ground state/excited state cycling (negligible triplet state dynamics, photobleaching etc.), and for excitation intensities far below optical saturation of that molecular species, the temporal autocorrelation function $g(t)$ of the fluorescence intensity $I(t)$ is given by Eq.(3.15). For simplicity, any optical background in the signal $I(t)$ was neglected. Thus, the autocorrelation function allows directly for assessing the diffusion constant D. Moreover,

by looking at the zero time and long time behavior of the autocorrelation $g(t)$ one finds Eq.(3.16) which allows for determining an absolute value of the concentration c provided the spatial extensions a and b are known, without necessitating any knowledge of the photophysical parameters of the studied molecules. Even if the assumption of Eq.(3.14) is no longer valid (and thus the factor in front of c on the r.h.s. of Eq.(3.16)), the proportionality between concentration c and the l.h.s. of Eq.(3.16) is a very general relation, allowing for *comparing* the concentrations of different solutions of the same dye. Exactly in this sense Eq.(3.16) will be used below when analyzing the experimental data.

Unfortunately, the situation becomes significantly more complicated if more than one molecular species is studied. For a mixture of N species, with corresponding parameters $\phi_f^{(i)}$, $\sigma^{(i)}$, $D^{(i)}$ and $c^{(i)}$, $i=1,\ldots,N$, the autocorrelation function reads

$$g(t)=\frac{\pi^{3/2}}{8}\kappa^2 a^2 b\left\{\sum_{i=1}^{N}\frac{\left(\phi_f^{(i)}\sigma^{(i)}\right)^2 c^{(i)}}{\left(1+4D^{(i)}t/a^2\right)\left(1+4D^{(i)}t/b^2\right)^{1/2}}+\pi^{3/2}a^2 b\left[\sum_{i=1}^{N}\phi_f^{(i)}\sigma^{(i)}c^{(i)}\right]^2\right\}. \quad (3.36)$$

Firstly, no simple relation as Eq.(3.16) exits anymore for the different species concentrations $c^{(i)}$. Secondly, if the values of the different diffusion coefficients $D^{(i)}$ are very similar, it is nearly impossible to separately monitoring changes of these values (i.e. upon binding).

The situation changes if different molecular species show different fluorescence decay behavior. For the sake of simplicity, consider two molecular species with fluorescence decay patterns $p_j^{(i)}$, $i=1,2$, where j denotes the number of the TCSPC channel, and $p_j^{(i)}$ is the (normalized) probability to measure a photon within the *j*th channel for species *i*. Any measured TCSPC curve I_j of a mixture of the two species will be a superposition of the form

$$I_j = w^{(1)}p_j^{(1)} + w^{(2)}p_j^{(2)}, \quad (3.37)$$

where the $w^{(i)}$ are the amplitudes of the photon count contributions (in number of photons) of the *i*th species. Thus, it would be useful to devise two filters $f_j^{(i)}$, $i=1,2$, with the properties

$$\left\langle \sum_{j=1}^{L} f_j^{(i)} I_j \right\rangle = w^{(i)}. \quad (3.38)$$

where L is the total number of TCSPC channels, and the brackets denote averaging over infinitely often repeated measurements. Moreover, one may ask that the $f_j^{(i)}$ have to be chosen in such a way as to minimize the relative errors

$$\left\langle \left(\sum_{j=1}^{L} f_j^{(i)} I_j - w^{(i)} \right)^2 \right\rangle . \tag{3.39}$$

It can be shown [20] that if the single photon detection follows a Poissonian statistics, the $f_j^{(i)}$ are expressed with the help of the weighted pseudoinverse of the matrix $\hat{M}$, $\hat{M}_{ij} = p_j^{(i)}$, as

$$f_j^{(i)} = \left(\left[\hat{M} \cdot \mathrm{diag} \left\langle I_j \right\rangle^{-1} \cdot \hat{M}^T \right]^{-1} \cdot \hat{M} \cdot \mathrm{diag} \left\langle I_j \right\rangle^{-1} \right)_{ij} . \tag{3.40}$$

where $\mathrm{diag}\left\langle I_j \right\rangle^{-1}$ is a $L \times L$-dimensional diagonal matrix with diagonal elements $\left\langle I_j \right\rangle^{-1}$, $j = 1, \ldots, L$, and the superscript T denotes matrix transposition. By direct calculation it can be checked that the filters $f_j^{(i)}$ and the patterns $p_j^{(i)}$ form an orthonormal system,

$$\sum_{j=1}^{L} f_j^{(i)} p_j^{(k)} = \begin{cases} 1, & i = k \\ 0, & i \neq k \end{cases} . \tag{3.41}$$

Now, the found filters $f_j^{(i)}$ can be used for obtaining the FCS curves of the two different molecular species separately. Consider the TCSPC-filtered fluorescence autocorrelation functions $g^{(i)}(t, \tau)$ as defined by:

$$g^{(i)}(t) = \left\langle \left(\sum_{j=1}^{L} f_j^{(i)} I_j(t') \right) \left(\sum_{j=1}^{L} f_j^{(i)} I_j(t' + t) \right) \right\rangle_{t'} . \tag{3.42}$$

where $I_j(t)$ is the fluorescence signal in the *j*th TCSPC channel at measurement time t. If this signal has the form of Eq.(3.37), then the orthonormality relation Eq.(3.41) ensures that the $g^{(i)}(t)$ have the average values (averaged over infinitely repeated measurements)

$$g^{(i)}(t) = \left\langle I^{(i)}(t') I^{(i)}(t'+t) \right\rangle_{t'} \qquad (3.43)$$

where $I^{(i)}$ is the fluorescence signal generated by only the *i*th molecular species (summed over all TCSPC channels). Thus, the $g^{(i)}(t)$, $i = 1,2$, reproduce the standard FCS curves of the two species separately.

3.6.2 Experiment

For the TCSPC-FCS measurements, a drop of dye solution was placed on a clean cover slip, and measurement duration was always 10 min. Excitation and detection was done at a distance of ca. 8 µm above the cover slips surface. Two dyes were used for the measurements: the commercially available dye Cy5 (Amersham), and the custom synthesized squaraine dye FR662. Firstly, for obtaining the TCPSC-patterns $p_j^{(i)}$, TCPSC measurement on pure 10^{-10} M solutions of both dyes were performed. The normalized curves are shown in Fig.19.

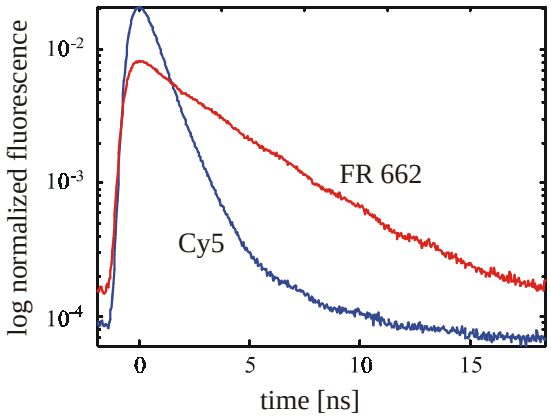

Fig. 19: Normalized TCSPC curves of pure solutions of Cy5 and FR662. These curves are used as the patterns $p_j^{(1)}$ and $p_j^{(2)}$ for constructing the filters according to Eq.(3.40).

Both dyes show monoexponential decays with ca. 1 ns decay time for Cy5 and ca. 3.5 ns decay time for FR662. For the TCSPC-FCS measurements, five mixed solutions of both dyes were prepared, with the concentration of FR662 kept constant at 10^{-10} M, and varying Cy5 concentrations $5 \cdot 10^{-11}$ M, 10^{-10} M, $2 \cdot 10^{-10}$ M, $5 \cdot 10^{-10}$ M and 10^{-9} M. For estimating the values $\langle I_j \rangle$ necessary for constructing the filters $f_j^{(i)}$, the approximation $\langle I_j \rangle \approx I_j$ was used. After

determining the $f_j^{(i)}$, the autocorrelation functions $g^{(i)}(t)$ were calculated according to Eq.(3.42). In Fig.20, the obtained and normalized $g^{(i)}(t)$ are shown for all five measured mixtures (circles), together with the autocorrelation curves of the pure solutions (solid lines).

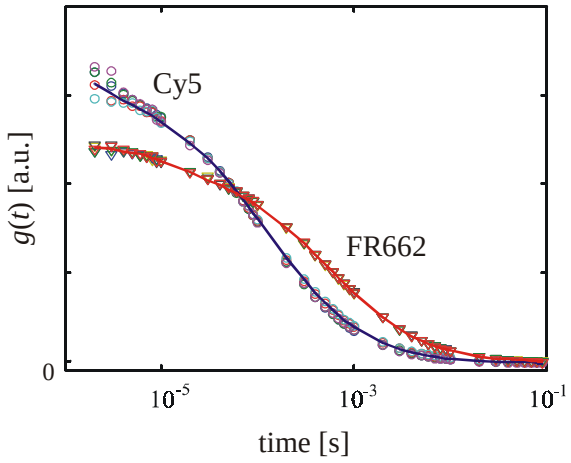

Fig. 20: Normalized TCSPC-filtered FCS curves $g^{(i)}(t)$ for the five measure dye mixtures (circles) together with normalized standard FCS-curves of pure dye solutions (solid lines).

Finally, the obtained $g^{(i)}(t)$-curves were used to separately estimate the concentrations of both dyes in the mixed solutions. For estimating the dye concentrations, Eq.(3.16) was used. To obtain the values of the $g_j^{(i)}(t)$ at zero time delay $t \to 0$, the non-normalized curves were fitted with the standard model as given in Eq.(3.15), which was however extended to include additional exponential terms to account for triplet state and isomerization effects [37,38]. The values $g_j^{(i)}(t \to 0)$ were determined by extrapolating the purely diffusional part of the fits as given by Eq.(3.15), neglecting the exponential contributions to the autocorrelation. This is necessary because Eq.(3.16) is valid only for the purely diffusional contribution to a FCS curve. The determined dye concentrations are shown in Fig.21, where the Cy5-concentrations are normalized by their maximum value for the $c_{\mathrm{Cy5}} = 10^{-9}\,\mathrm{M}$/ $c_{\mathrm{FR662}} = 10^{-10}\,\mathrm{M}$ solution, and the FR662-concentrations are normalized by their average value over all five measurements.

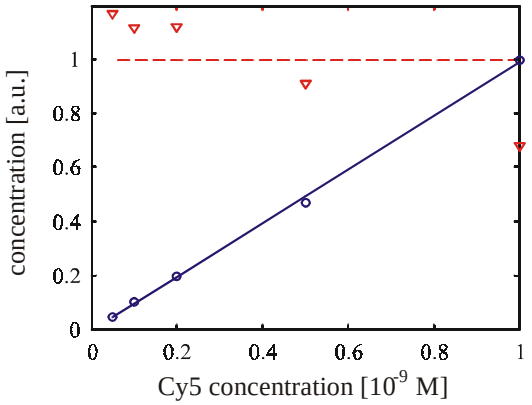

Fig.21: Relative dye concentrations of Cy5 (circles) and FR662 (triangles) as determined by Eq.(3.16). The abscissa gives the actual Cy5-concentration of the measured mixture; the FR662-concetration was kept constant at 10^{-10} M. The solid and broken lines show the theoretically expected values.

3.6.3 Discussion

Fig.20 clearly shows that TCSPC-separating the FCS curves for different dyes works excellently. For the five measured mixtures, the obtained ten autocorrelation curves $g^{(1,2)}(t)$ are basically identical toe the FCS curves of the pure solutions. Thus, TCSPC-FCS offers the possibility to separately monitor the fluorescence correlation of several molecular species simultaneously. In this sense, it is an alternative to two- or multicolor multi-channel FCS, where several detection channels and usually several excitation sources are required. The great advantage of TCSCP-FCS with respect to multi-color-FCS is that excitation and detection is done, for all dyes, with a single excitation source and within a single detection channel, avoiding any problems caused by chromatic aberrations. The method is also easily adapted to cross-correlation FCS. In the framework of TCSPC-FCS, the cross-correlation function $g^{(1\times2)}(t)$ of a two-dye sample is calculated as

$$g^{(1\times2)}(t)=\left\langle\left(\sum_{j=1}^{L} f_j^{(1)} I_j(t')\right)\left(\sum_{j=1}^{L} f_j^{(2)} I_j(t'+t)\right)\right\rangle_{t'} . \qquad (3.44)$$

(a similar relation holds for $g^{(2\times1)}(t)$). For the solutions measured in this work, the cross-correlation between Cy5- and FR662-fluorescence is flat, because there is no inherent correlation between the two fluorescence signals.

As Fig.21 shows, using the separated FCS curves $g^{(1,2)}(t)$ for determining independently the concentrations of the two dyes in the mixed solutions works excellently for Cy5, but shows rather large deviations form the supposedly flat curve for FR662. The scattering of the FR662 concentration values from the theoretically constant value was also seen when estimating the FR662-concentrations by simply deconvolving the TCSPC-curves of the mixed solutions into the two contributions of Cy5 and FR662. This indicates that the scattering of the concentration values is at least partially due to real variations of the actual FR662 concentrations.

Preparation of a solution with an exact FR662 concentration at the 10^{-10} M level is a rather difficult task, especially due to the observed high surface-adsorption affinity of that dye. Another difficulty arises from the significant isomerization/triplet state dynamics of that dye that has a strong impact on the short-time behavior of the FCS curves. This makes the extraction of the purely diffusional part of the autocorrelation more difficult and adds to the error of the concentration determination when using Eq.(3.16).

Extension of the presented TCSPC-FCS method to more than two dyes is straightforward. For obtaining the filters $f_j^{(i)}$ for more than two dyes, Eq.(3.40) can directly be used, only with index i now running from one to the number of different dyes. Finally, the method can still be combined with conventional multi-color detection setups, thus enabling the separation of FCS curves both by fluorescence decay behavior and spectrum.

3.7 References

1. D. Magde, E. Elson, and W.W. Webb, *Phys. Rev. Lett.* **29** (1972) 705.
2. W.W. Webb, *Quart. Rev. Biophys.* **9** (1976) 49.
3. N.L. Thompson, "Fluorescence correlation spectroscopy", in: *Topics in Fluorescence Spectroscopy 1*, Ed.: J.R. Lakowicz (Plenum Press, New York, 1991) 337.
4. J. Widengren and Ü. Mets, "Conceptual basis of Fluorescence Correlation Spectroscopy and related techniques as tools in bioscience", in: *Single-molecule detection in solution: methods and applications*; Eds.: J. Enderlein, C. Zander, R.A. Keller (VCH-Wiley, 2001) in press.
5. M. Eigen and R. Rigler, *Proc. Natl. Acad. Sci. USA* **91** (1994) 5740.
6. R. Rigler *J. Biotechnol.* **41** (1995) 177.
7. F. Oehlenschläger, P. Schwille, and M. Eigen *Proc. Natl. Acad. Sci. USA* **93** (1996) 12811.
8. S. Maiti, U. Haupts, and W.W. Webb, *Proc. Natl. Acad. Sci. USA* **94** (1997) 11753.
9. K.J. Moore, S. Turconi, S. Ashman, M. Ruediger, U. Haupts, V. Emerick, and A.J. Pope, *J. Biomol. Screening* **4** (1999) 335.
10. M. Auer, K.J. Moore, F.J. Meyer-Almes, R. Günther, A.J. Pope, and K.A. Stöckli, *Drug Discovery Today* **3** (1998) 457.
11. E. Overbeck, C. Sinn, I. Flammer, J. Ricka, *Rev. Sci. Instrum.* **69(10)** (1998) 3515-23.
12. Li-Qiang Li, Lloyd M. Davis, *Rev. Sci. Instrum.* **64(6)** (1993) 1524-9
13. P. Török and P. Varga *Appl. Opt.* **36**(11) (1997) 2305-12.
14. E. Wolf, *Proc. Roy. Soc. London.* **253 A** (1959) 349-57.
15. B. Richards and E. Wolf, *Proc. Roy. Soc. London.* **253 A** (1959) 358-79.
16. J. Enderlein, *Opt. Lett.* **25** (2000) 634-6.
17. M. Abramowitz, I.A. Stegun, Eds., *Handbook of mathematical functions* (Harry Deutsch, Thun, Frankfurt am Main, 1984).
18. J. Enderlein, T. Ruckstuhl, S. Seeger, *Appl. Opt.* **38** (1999) 724-32.
19. R. Müller; C. Zander; M. Sauer; M. Deimel; D.S. Ko; S. Siebert; J. Arden-Jacob; G. Deltau; N.J. Marx; K.H. Drexhage; J. Wolfrum *Chem. Phys. Lett.* **262** (1996) 716.
20. S. Akiyama (1993) *Near Infrared Luminescence Spectroscopy,* in:Schulman SG (ed.) **Molecular Luminescence Spectroscopy**, vol. 3, pp. 229-306, Wiley & Sons, New York.

21. S. Dähne, U. Resch-Genger and O. S. Wolfbeis (1998) *Near-Infrared Dyes for High Technology Applications*, NATO ASI Series vol. **53**, Kluwer Acad. Publ., Dordrecht (NL), ISBN 0-7923-5101-0.
22. J. Mama, *Adv. Colour Sci. Technol.* **2** (1999) 162-76.
23. J. Fabian, N. Nakazami, M. Matsuoka, *Chem. Rev.* **92** (1992) 1197-1226.
24. M. Matsuoka (ed.) *Infrared Absorbing Dyes*. Plenum Press, New York.
25. B. Oswald, M. Gruber, M. Böhmer, F. Lehman, M. Probst, O. S. Wolfbeis, *Photochemistry and Photobiology*, **74(2)** (2001) 237-45.
26. P. Kask, K. Palo, D. Ullmann and K. Gall, *Proc. Natl. Acad. Sci. USA*, **96** (November 23, 1999) 13756-61.
27. J. A. Nelder and R. Meade, *Comput. J.*, (1965) 308. [40]
28. D. W. Marquardt, *SIAM* **11(2)** (1963) 431.[41]
29. J. Enderlein and R. Erdmann *Optics Communications* **134** (1997) 371-8.[42]
30. P. Schwille, F.J. Meyer-Almes, and R. Rigler *Biophys. J.* **72** (1997) 1878.
31. R. Rigler, Z. Földes-Papp, F.J. Meyer-Almes, C. Sammet, M. Völcker, and A. Schnetz, *J. Biotechnol.* **63** (1998) 97.
32. U. Kettling, A. Koltermann, P. Schwille, and M. Eigen, *Proc. Nat. Acad. Sci. USA* **95** (1998) 1416.
33. A. Koltermann, U. Kettling, J. Bieschke, T. Winkler, and M. Eigen, *Proc. Nat. Acad. Sci. USA* **95** (1998) 1421.
34. T. Winkler, U. Kettling, A. Koltermann, and M. Eigen, *Proc. Nat. Acad. Sci. USA* **96** (1999) 1375.
35. K. Heinze, A. Koltermann and P. Schwille *Proc. Nat. Acad. Sci. USA* **97** (2000) 10377.
36. J. Bieschke, A. Giese, W. Schulz-Schaeffer, I. Zerr, S. Poser, M. Eigen, and H. Kretzschmar, *Proc. Nat. Acad. Sci. USA* **97** (2000) 5468.
37. J. Widengren, Ü. Mets, and R. Rigler, *J. Phys. Chem.* **99** (1995) 13368.
38. J. Widengren and P. Schwille, *J. Phys. Chem.* A **104** (2000) 6416.

4. Confocal Imaging of Single Molecules

In the following subsections, experimental results of single molecule fluorescence detection on surfaces will be reported, demonstrating the imaging capability of the system. Knowing the exact correlation between detected photons and image position, the TCSPC times of the detected photons can be used for calculating lifetime images. The resulting lifetime images clearly show the difference in lifetimes between different dyes. Additionally, it is shown how the TCSPC capabilities of the system can not only be used for lifetime imaging but also for multi-channel measurements. Intensity, polarization, and lifetime images of single molecules on surfaces are presented. It is shown how, by using a ring-like laser excitation, three-dimensional polarization measurements of single fluorescent molecules tacked on a glass substrate can be performed. Finally, an outlook is given concerning *in vivo* SMD-studies of living cells, an application that will certainly gain significant importance in the future.

4.1 Intensity imaging

Based on the recorded TTTR data, image reconstruction is a straightforward procedure. In all experimental measurements reported below, the scan driver was set to perform 500 scan steps in each direction, with a step size of 50 nm and a step time of 500 µs. The fluorescence intensity image was calculated by sorting the tagged photons into time bins of 500 µs bin width, and ordering the time bins into a 500×500 array, paying attention to the alternating scan directions of subsequent scan lines.

Although the start times of data acquisition and scan signal generation were perfectly synchronized by the scan driver, the resulting image shows a line-to-line mismatch which is caused by a delay of the motion of the piezo stage with respect to the driver signal. This delay depends on the mass of the moving part of the stage as well as on the mass of the sample, and is thus different for different samples. However, this phase shift remains constant during one scan, permitting the subsequent application of an alignment algorithm. Let $n(j)$ be the number of detected photons in the *j*th time bin of 500 µs bin width. The first time bin ($j=1$) corresponds to the start of the data acquisition/driver signal generation. Due to the delay of the

scan stage, the actual scanning starts only some p time bins later. For determining the correct value of p, a correlation function $g(p)$ is computed as

$$g(p)=\sum_{j=1}^{499}\sum_{k=1}^{500} n(p+500(j-1)+k)\cdot n(p+500(j+1)-k+1) \tag{4.1}$$

with *p* taking integer values between zero and some appropriately large value (in the experiments below, $p_{\max}=10$ proved to be sufficient). The function $g(p)$ shows a maximum for that value of *p* which corresponds to the delay of the scan stage motion. This algorithm works the better the more distinct features an image contains. Only for a purely random signal (noise), an image would not contain any correlation allowing for its correct alignment.

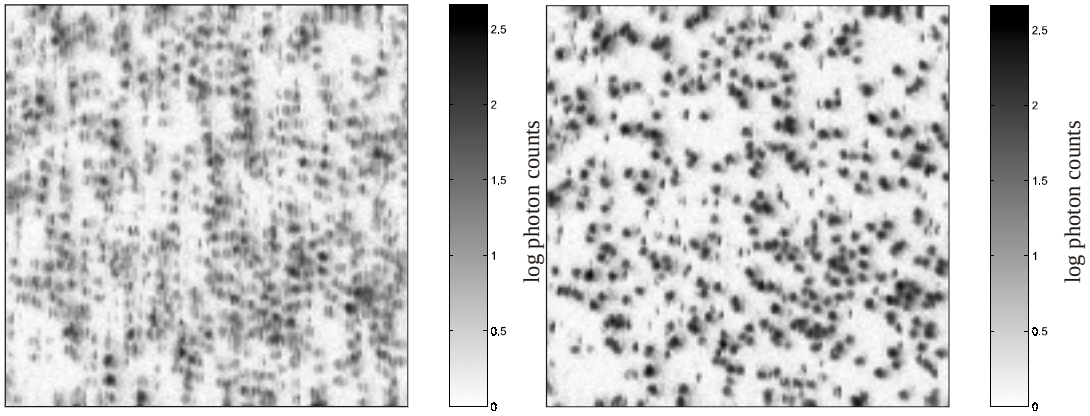

Fig22: (a) Non-aligned log fluorescence intensity image of LightCycler Red molecules on a glass surface. The gray scale visualizes the decadic logarithm of photon number per pixel. Main scan direction is up/down, scanning line by line from left to right. Axes labels on the image give pixel number, one pixel has 50×50 nm^2. Due to the delay of the scan stage, every second scan line is vertically shifted with respect to the previous one. (b)Same as the previous image, but after applying the alignment algorithm. Single molecules are discernible as highly fluorescent circular spots. Single vertical streaks represent molecules diffusing towards and away from the surface during the scan, thus appearing only in one single scan line. Blinking of single molecules (temporary transition of molecules into a non-fluorescent state) can also be seen as white vertical streaks within the dark shapes of single molecule spots. Small residual line-to-line misalignment effects are also discernable in some molecule images, due to the limited precision of the table positioning at high scan speeds.

Figs.22a,b show individual molecules of the rhodamine dye LightCycler Red (Roche Molecular Biochemicals), immobilized on a glass coverslip. In Fig.22a, the non aligned image is shown, and Fig.22b shows the same image after alignment. The gray value of every pixel

gives the decadic logarithm of the number of detected photons per pixel (coding is shown by the gray scale bar on the right side of the figures). Scan direction is the vertical direction, and the image is build up line by line from left to right. Every dark circular spot corresponds, on average, to a single molecule. Some of the dark spots show a semicircular shape, with a cut-off half side. These images correspond to sudden photobleaching of the observed molecules. Also, bright vertical streaks within the dark images of single molecules reflect the photophysical dynamics of the observed molecules (intermittent non-fluorescent dark states). Careful inspection of the molecule images show slight dark shadows around every spot. These shadowy regions are caused by the secondary intensity maximum of the diffraction limited laser focus.

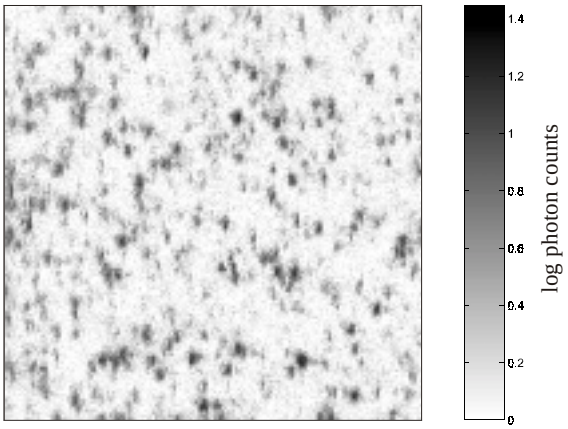

Fig.23: Fluorescence intensity image of LightCycler Red molecules on a glass surface, detected with a PMT instead with a SPAD. A confocal pinhole of 100 µm diameter was used.

For the sample studied, the maximum photon count number per pixel reaches values of ca. 500 photons. For comparison between the detection efficiencies of a SPAD and a PMT, a similar sample was scanned with a PMT (H6240-02, Hamamatsu) as detector. The result is shown in Fig.23: the maximum number of photons per pixel reaches 26 photons, thus giving a roughly 20fold less sensitivity of the PMT detection compared with the SPAD detection.

4.2 Lifetime image reconstruction

Knowing the exact correlation between detected photons and image position, the TCSPC times of the photons can be used for calculating lifetime images. Although one can try to calculate one or several fluorescence decay time values (depending on whether one assumes an

mono- or multiexponential fluorescence decay) for every pixel of the image, a more reasonable method for the low intensity data of single molecule experiments is to estimate the ”lifetime” of an image pixel by simply calculating an average lifetime value of all the photons falling into that pixel, taking into account only photons arriving within a given time window *after* the exciting laser pulse (for dark count suppression). Alternatively, single molecules can be localized from the intensity image, and all fluorescence photons for a given molecule can be used for calculating its lifetime characteristics. However, the details of such procedures are beyond the scope of the present paper, but see e.g. Ref.[1-3].

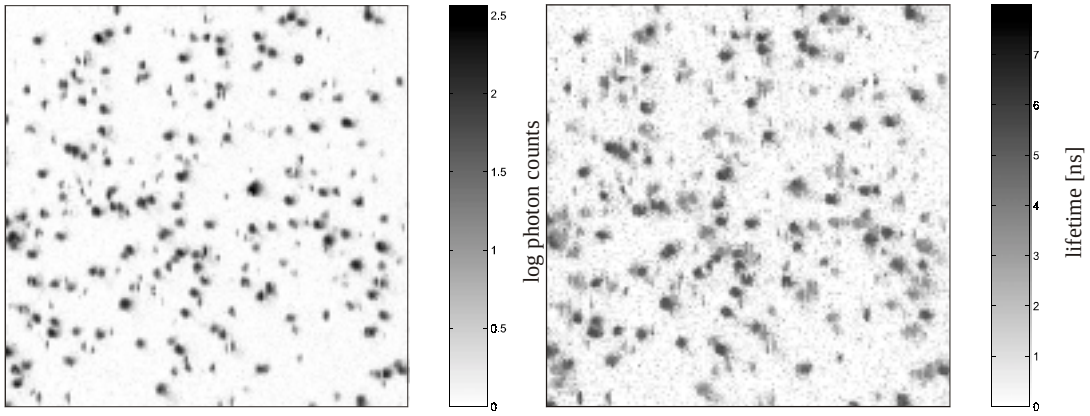

Fig.24: (a) Log intensity image of a mixture of LightCycler Red and Cy5 molecules on glass. Scanning procedure and image properties are the same as in Fig. 22. (b) Lifetime image, corresponding to the intensity image in (a). The gray scale visualizes the average lifetime per pixel in nanoseconds. Two populations of molecules are discernable: dark spots correspond to LightCycler Red molecules with ~ 4 ns lifetime, whereas bright spots are Cy5 molecules with ~ 1 ns lifetime.

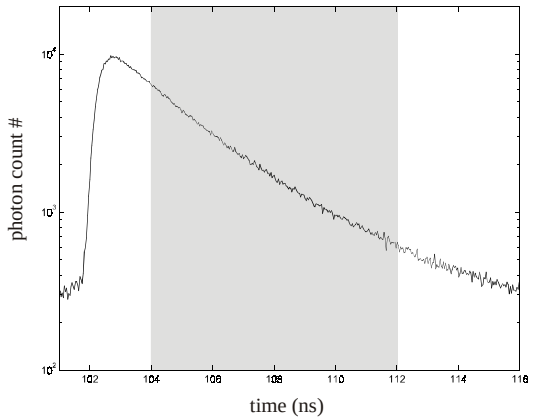

Fig.24c: TCSPC histogram of all photons detected during the scan. The gray area depicts the time window that is used for obtaining average lifetime values per pixel in the lifetime image, Fig.24b.

For the test sample, both the rhodamine dye LightCycler Red and a cyanine dye Cy5 (Amersham) were immobilized on the coverslip. Fig.24a shows the intensity image, where single molecule spots can be seen, but no discernable difference between LightCycler Red and Cy5 molecules. Fig.24c shows the TCSPC histogram of all photons detected during the complete scan. The lifetime image was calculated by averaging, pixel by pixel, the TCSPC times of the detected photons that are falling into channels in the gray area of Fig.24c. The resulting lifetime image (Fig.24b) clearly shows the difference in lifetimes between the LightCycler Red (~ 4 ns) and the Cy5 molecules (~ 1 ns). More sophisticated data evaluation techniques allow even for distinguishing between these two molecular species with nearly 100 % certainty [1-3], which allows to simultaneously monitoring different molecular species without the necessity of using several excitation and detection channels.

4.3 Time-windowed detection: Polarization imaging

In many applications, it is important to gain information about the fluorescence polarization. In the simplest approach, fluorescence polarization is measured by a two-channel detection setup, the two channels recording the fluorescence in the two possible polarization directions. In the measurement setup presented here, an important peculiarity of the two-channel detection is that the signals of *both* SPADs are fed into the same *single* input channel of the TCSPC electronics. This is due to the fact that the older version of the TimeHarp 200 electronics which was used in the setup applying the scanner driver, is capable of processing data of only one input channel (meanwhile, newer versions of the card are available which are fully capable of multichannel signal processing). For achieving dual channel signal recording, pulses from one detector are delayed in time with respect to those of the other by roughly half the time interval between two laser pulses. For this purpose, a coax transmission line of necessary length is used as a delay. Then, photons from different detectors can be distinguished by their falling into different time windows with respect to the exciting laser pulse train. This is shown by the TCSPC histogram in Fig.25, showing the decay time histogram of all photons of a scanned image. The sample consisted LightCycler Red molecules. As described above, the signal of the second SPAD was delayed by ~ 12 ns. Assuming that all photons arriving later than 12 ns after the exciting laser pulse belong to the second detector and those arriving earlier than 12 ns to the first, a virtual two-channel measurement can be done. Of course, this assumption is only justified if the fluorescence decays sufficiently fast with respect to the width of the set time-windows. For a dye with 3 ns decay time, the remaining fluorescence

after 12 ns is ca. $\exp(-4) \approx 0.02$, thus giving rise to a crosstalk between the two virtual channels of ca. 2 %. For many practical applications, this is a tolerable value.

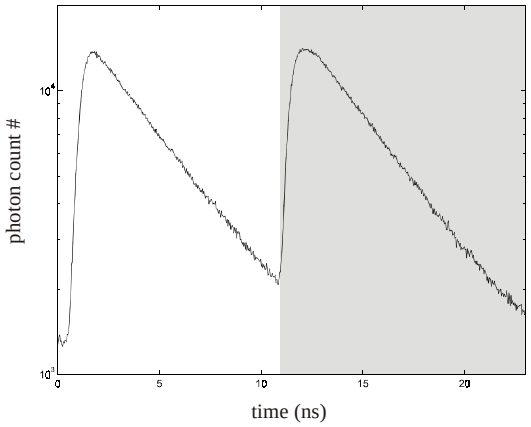

Fig.25:- TCSPC histogram of all photons of a scanned image detected with two SPAD detectors in two detection channels. Photons falling into the left time window (non-shaded region) are attributed to the first detector, and photons falling into the right time window (shaded region) are attributed to the second detector.

The exciting laser beam was linearly polarized with a direction diagonal to the image edges, as shown on Fig.26. For a sample, two measurements with two different excitation polarization directions were made, thus resulting in four different images corresponding to the four panels of Fig.26.

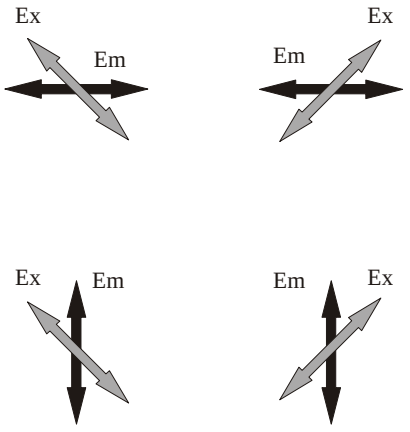

Fig.26: Geometry of excitation and detection polarization. Ex indicates excitation polarization, Em indicates emission polarization. Left two panels corresponds to a first two-channel scan, right two panels to a second scan, with excitation polarization rotated by 90° .

This approach allows one to determine the molecules' excitation dipole orientation in a unique manner. Assuming that the excitation dipole axis of the molecule forms, within the surface plane of the sample, an angle ψ with the horizontal image axis, the four detectable fluorescence intensities I_{jk}, $j=1,2$ and $k=a,b$, corresponding to the four excitation/detection polarization geometries of Fig.24, are given by

$$\begin{aligned} I_{1a}(\phi) &= I_{\perp} + I_{\parallel}\cos^2(\psi-\pi/4)\cos^2\psi \\ I_{2a}(\phi) &= I_{\perp} + I_{\parallel}\cos^2(\psi-\pi/4)\sin^2\psi \\ I_{1b}(\phi) &= I_{\perp} + I_{\parallel}\cos^2(\psi+\pi/4)\cos^2\psi \\ I_{2b}(\phi) &= I_{\perp} + I_{\parallel}\cos^2(\psi+\pi/4)\sin^2\psi \end{aligned} \qquad (4.2)$$

where $I_{\perp}$ and $I_{\parallel}$ are the fluorescence signal contributions from the vertical and horizontal component of the molecule's dipole; the numerical index corresponds to the detection polarization orientation (1 is horizontal, 2 is vertical orientation), and the indices *a,b* to the excitation polarization orientation (*a* for upper left to lower right polarization, *b* for lower left to upper right). The above relations can be transformed into

$$\begin{aligned} I_{1a} + I_{2a} - I_{1b} - I_{2b} &= I_{\parallel}\sin 2\psi \\ I_{1a} - I_{2a} + I_{1b} - I_{2b} &= I_{\parallel}\cos 2\psi \end{aligned} \qquad (4.3)$$

uniquely determining the angle ψ by the four intensity values on the l.h.s.

An experimental example is shown in Fig.27a,b. Fig.27a shows the intensity image of LightCycler Red molecules on a glass coverslip, and Fig.27b gives the corresponding dipole orientation angles ψ as determined by the above relations. The analysis was performed pixel by pixel, thus resulting in arbitrary ψ-values for regions were no molecule is present. However, the roughly non-changing value of ψ across a given molecule image shows the consistency of the chosen approach, and that the molecules do not reorient during the scans (although some exceptions are discernible).

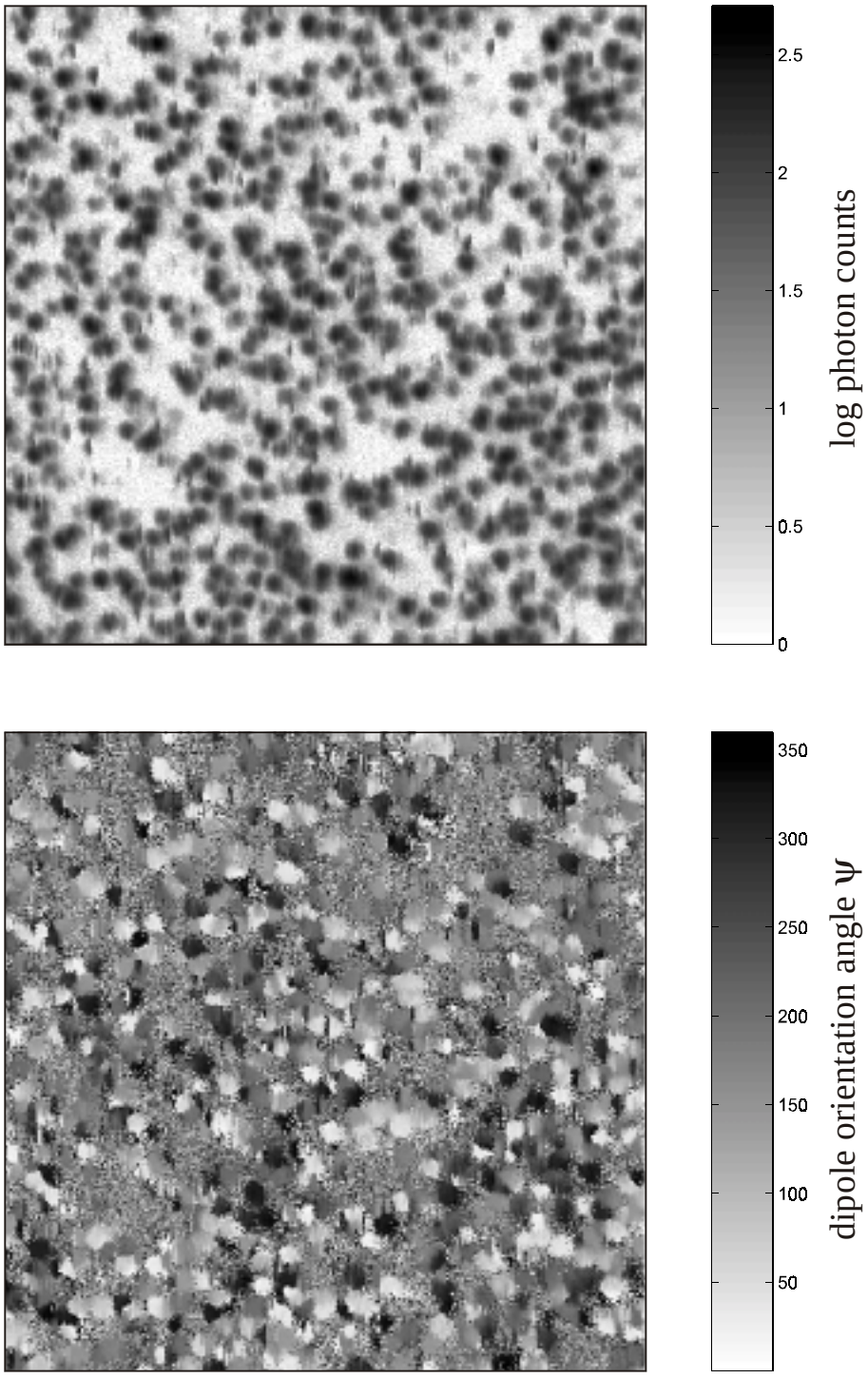

Fig.27: (a) Log intensity image of LightCycler Red molecules on glass, detected with the two-channel setup. Photons of both channels are summed to obtain this intensity image. (b) Polarization image showing the value of ψ for every pixel. Single molecules are discernible as regions with relatively homogenous value of ψ, compare with the corresponding intensity image of the previous figure.

In the above analysis, it was always assumed that excitation and emission dipole axes of the molecules are collinear. If this is not the case, one has to perform more measurements with different excitation polarization orientations, favorably by continuously rotating the excitation polarization with a rotating polarizer. Then, by evaluating the resulting fluorescence intensity modulation, complete and independent information about both excitation and emission dipole orientation can be obtained, see e.g. [4-6].

4.4 Ring excitation: three-dimensional molecule orientation

Theoretically, based on the relations of the last subsection, one could try to extract from the four intensity images not only the in-plane angle ψ, but as well the relative intensities $I_{\perp}$ and $I_{\parallel}$, being related to the dipole components vertical and parallel to the sample's surface. However, due to the relatively low intensity of the vertical electric field component of the exciting laser light, the value of $I_{\perp}$ will always be very small compared with the value of $I_{\parallel}$. Moreover, the analysis would be very sensitive to shot-noise variations of the measured photon count numbers.

The relation between vertical and parallel electric field component of the exciting laser field can be much increased by a special mode of illumination (see also [7]): instead coupling a collimated laser beam into the input aperture of the objective, a ring of light is coupled in by blocking the central part of the laser beam with an opaque aperture (see Fig. 28). This annular illumination has the effect that mostly light rays with high incidence angle contribute to the excitation light at the focal point, leading to a particularly high relation of vertical to parallel electric field intensity.

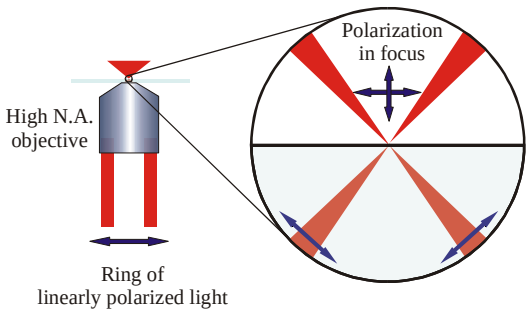

Fig.28: Geometry of the annular aperture illumination, visualizing the enhanced vertical electric field component within the focal region (enlarged image on the right).

The resulting distributions of electric field amplitudes for the three possible directions are shown in Fig.29, as the result of an exact wave optical calculation under annular illumination.

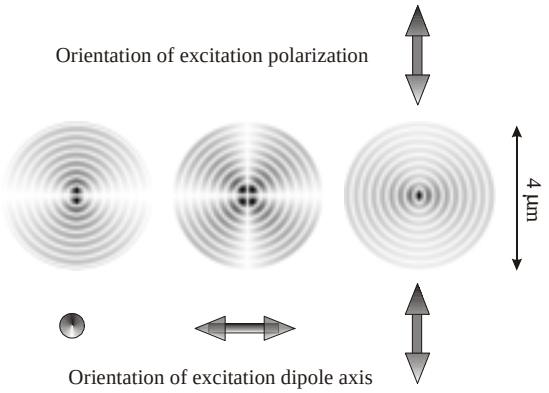

Fig.29: Results of wave optical calculations of the electric field amplitude distributions for the three possible field orientations: within sample surface parallel to incident laser beam (above), within sample surface perpendicular to incident laser beam (middle), perpendicular to sample surface (bottom).

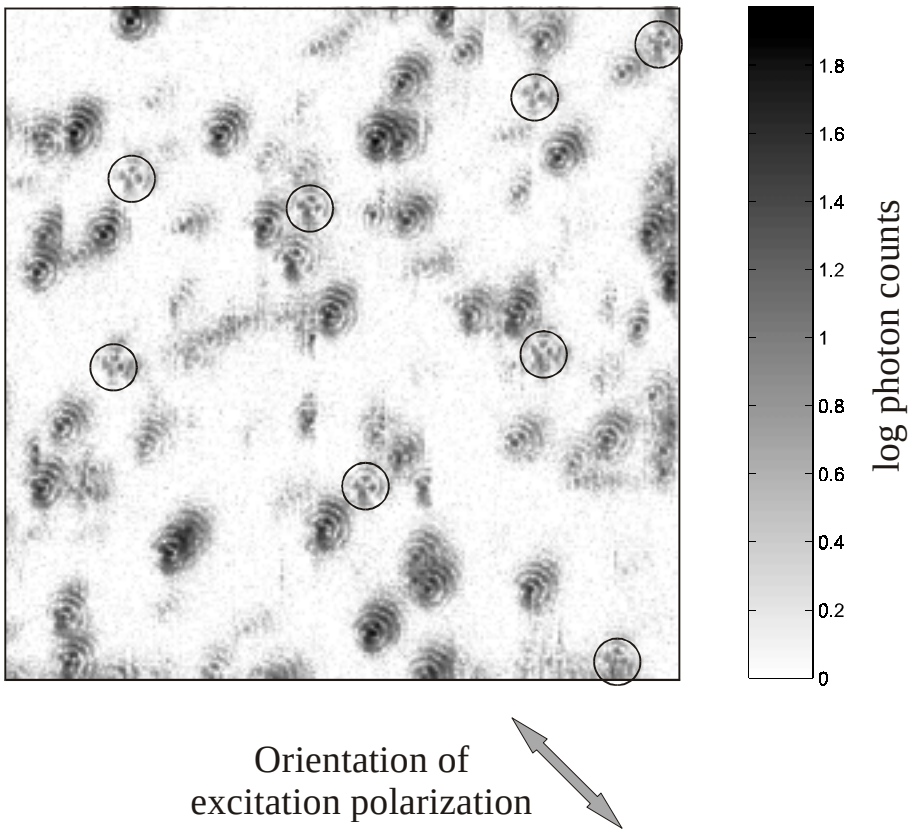

Fig.30: Log intensity image of LightCycler Red molecules on glass under annular excitation. Circles enclose images of single molecules having their excitation dipole parallel to the surface and nearly perpendicular to the polarization of the incident laser beam.

The three different electric field orientations show distinct intensity patterns, which can be used to evaluate the three dimensional orientation of a molecule's excitation dipole. Using such a pattern recognition approach to the dipole orientation has the advantage that it is much less sensitive to shot-noise variations than directly using the intensity values themselves.
An example of a scanned image under annular illumination is shown in Fig.30 (LightCycler Red on glass coverslip). Annular illumination was achieved by blocking around half the entry aperture diameter of the objective. Circles enclose images of molecules with excitation dipoles nearly perpendicular to the polarization of the incident light ring (compare with the second panel of Fig.29). In the image of Fig.30, no purely vertical oriented dipole can be clearly discerned, which is due to the fact almost all molecule on the sample are with their dipoles nearly parallel to the sample surface. However, the shown molecule images clearly demonstrate the possibility to extract three-dimensional dipole orientation information from fluorescence intensity patterns under annular illumination.

4.5 Outlook

In the present part, the basic components of a SMD capable CLSM were described in detail, and experimental SMD results were presented. Particularly, we have demonstrated the capabilities of a CLSM in obtaining information about the major fluorescence properties intensity, lifetime, and polarization. Extension of the described system is straightforward, for example the incorporation of more than one laser excitation source for multi-wavelength fluorescence excitation.

Another important application of a SMD CLSM is the study of living cells and tissues, adding to the exceptional high contrast and 3D sectioning capability of a CLSM the sensitivity of SMD. A major restriction of the CLSM, compared with imaging wide field microscopy SMD, is the relatively slow rate of image acquisition. This can be seen in Fig.31, which shows the sectioning of a human endometrial cancer (HEC-1B) cell. The cell was cultivated on a cover slip and embedded within a solution containing fluorescently labeled (Cy5) neuropeptides binding to its neuropeptide hNPY Y_5 receptors[8].

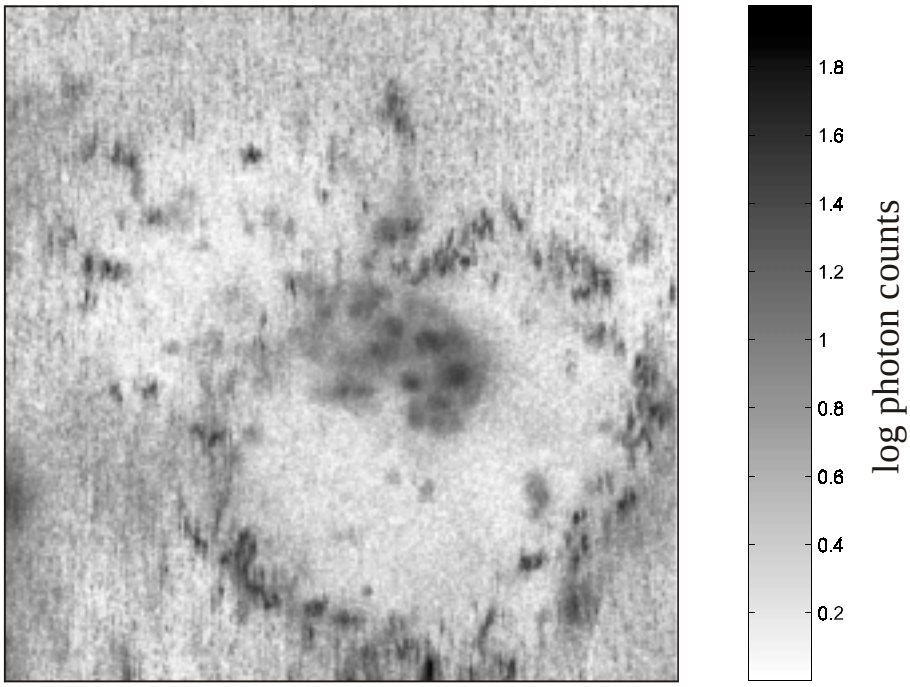

Fig.31: Image of a horizontal section of a human endometrial cancer (HEC-1B) cell on a glass cover slip. The cell is embedded within a solution containing Cy5-labeled neuropeptide binding to its human neuropeptide hNPY Y_5 receptors.

An interesting property of the CLSM is that although the Cy5-labeled neuropeptide concentration was high outside the cell ($5 \cdot 10^{-10}$ M), single molecules can still be discerned within the cell's membrane, due to its exceptionally strong suppression of out-of-focus fluorescence. These single molecules occur as rather diffuse spots due to their diffusion during the time of one image scan. However, the advantages of the CLSM are its ability to follow, at least at a given position of detection, very fast processes, down to a nanosecond level, which may be important if one would like to monitor e.g. fast molecule rotations, or fluorescence lifetimes. In this respect, the SMD CLSM is an ideal complementation to wide field microscopy SMD.

4.6 References

1. M. Köllner, P. Fischer, J. Arden-Jacob, K.-H. Drexhage, R. Müller, S. Seeger, J. Wolfrum, *Chem. Phys. Lett.* **250** (1996) 355-60.
2. J. Enderlein, P.M. Goodwin, Orden A. Van, W.P. Ambrose, R. Erdmann, R.A. Keller, *Chem. Phys. Lett.* **270** (1997) 464-70.
3. J. Enderlein, M. Sauer, *J. Phys. Chem. A.* **105** (2001) 48-53.
4. T. Ha, T. Enderle, D.S. Chemla, P.R. Selvin, S. Weiss, *Phys. Rev. Lett.* **77** (1996) 3979-82.
5. T. Ha, J. Glass, T. Enderle, D.S. Chemla, S. Weiss, *Phys. Rev. Lett.* **80** (1998) 2093-7.
6. T. Ha, T.A. Laurence, D.S. Chemla, S. Weiss, *J. Phys. Chem. B* **103** (1999) 6839-50.
7. B. Sick, B. Hecht, L. Novotny, *Phys. Rev. Lett.* **85** (2000) 4482-5.
8. C. Moser, G. Bernhardt, J. Michel, H. Schwarz, and A. Buschauer, *Can. J. Physiol. Pharmacol.* **78** (2000) 134-42.

5. Summary

This thesis describes the development and construction of an advanced, time-resolved confocal laser-scanning microscope for ultrasensitive fluorescence detection in solution and on surfaces. The realized system is capable of monitoring single molecules in liquids and on surfaces, capable of performing emission and/or polarization spectroscopy, time-resolved spectroscopy with picosecond temporal resolution, and FCS with sub-microsecond temporal resolution. Moreover, it allows ultrafast scanning of surfaces thus allowing wavelength, polarization and lifetime imaging of immobilized molecules and samples (e.g. cells, tissue). Thus, the realized system is at present one of the most advanced systems world wide. With the help of this measurement system, several novel theoretical concepts of SMD could be experimentally realized and tested.

In part 1 an introduction to the field of single molecule detection at ambient temperature under special consideration to confocal microscopy is given. The advantages and disadvantages of confocal single molecule detection in comparison to wide field microscopy is discussed, followed by a review of confocal single molecule detection in historical order.

Part 2 describes in detail the individual components of the built measurement system as well as its optical design. The system employs compact electronics for time-correlated single-photon counting, allowing for measuring fluorescence lifetime with 40 ps temporal resolution, and for continuously recording photon arrival times with 100 ns resolution. A central feature of the system is its asynchronous data acquisition mode (time-tagged time-resolved photon counting), assuring minimum data load and maximum versatility in spectroscopic evaluation of the measured data. Additionally, an especially developed driver electronics serve for synchronization of scanning and data acquisition, which is significant for achieving high spatial image resolution.

In part 3, advanced techniques of single molecule spectroscopy in solution are presented and applied. FCS is an important measurement technique for obtaining information about diffusion coefficients and concentrations of fluorescent analyte molecules in solution. Usually, when evaluating measured fluorescence correlation data, a simplified model is applied which rests on the rather unrealistic assumption of an ellipsoidal detection volume. There is no prin-

cipal difficulty in modeling FCS curves based on the knowledge of the exact excitation intensity distribution and collection efficiency function.

In section 3.4, it is shown how experimental data can be analyzed by an exact *ab initio* modeling of a FCS experiment, taking into account both the exact spatial light intensity profile within the focus of the exciting laser beam, and the collection efficiency function of the light sampling optics. Both functions are obtained by exact wave optics calculations of the excitation and detection optics as outlined in section 3.3. The computed fluorescence correlation spectroscopy model curves are directly compared with measured fluorescence correlation spectroscopy curves for different geometric configurations of the optical system. The important role of an exact mechano-optical adjustment of the whole measurement setup, and the critical influence of different kinds of misalignments on the measured fluorescence correlation curves are shown.

The presented method of fluorescence correlation data evaluation bears the great potential of providing a way for an *absolute* determination of diffusion coefficients *and* analyte concentrations, without involving any empirical fit parameter or ad-hoc assumptions. Moreover, the numerical effort of the analysis is only slightly larger than that of the conventional fluorescence correlation analysis. Thus, it is hoped that the presented approach to fluorescence correlation data analysis will be of great use for anybody interested in exact fluorescence correlation data evaluation.

There is growing demand in the use of fluorescent probes for the detection of biological compounds like proteins. The main advantage of using long-wavelength light sources and labels is the decreased auto-absorption and auto-fluorescence, particularly beyond 600 nm, from cells and tissue because the optical window of blood and other biological material is in the range of 650 to 700 nm. Therefore, new labels belonging to the class of the cyanine dyes or to the closely related class of squaraine dyes were characterized with respect to their specific brightness and fluorescence lifetime.

By combining TCSPC with FCS measurements, a new method for performing TCSPC-FCS measurements on mixtures of several fluorescent molecular species is introduced. It uses time-resolved fluorescence detection for separating the different FCS contributions of the different species. This allows for simultaneously and independently monitoring the diffusion of several molecular species in one sample, or for performing multi-label cross-correlation measurements. In this sense, it is an alternative to standard two- or multicolor multi-channel FCS, where several detection channels and usually several excitation sources are required. The great advantage of TCSCP-FCS with respect to multi-color-FCS is that excitation and detection is done, for all dyes, with a single excitation source and within a single detection

channel, avoiding any problems caused by chromatic aberrations. The method is also easily adapted to cross-correlation FCS. In this thesis the theoretical basis and experimental results of this new method are introduced. Extension of the presented TCSPC-FCS method to more than two dyes is straightforward. Finally, the method can still be combined with conventional multi-color detection setups, thus enabling the separation of FCS curves both by fluorescence decay behavior and spectrum.

In part 4 the imaging capability of the system is demonstrated on imaging single molecules immobilized on glass substrates. Although the start times of data acquisition and scan signal generation were perfectly synchronized by the scan driver, the resulting image shows a line-to-line mismatch which is caused by a delay of the motion of the piezo stage with respect to the driver signal. This delay depends on the mass of the moving part of the stage. However, this phase shift remains constant during one scan, permitting the subsequent application of an alignment algorithm. Knowing the exact correlation between detected photons and image position, the time correlated single photon counting times of the photons can be used for calculating lifetime images. The resulting lifetime images clearly show the difference in lifetimes between the LightCycler Red (~ 4 ns) and the Cy5 molecules (~ 1 ns). More sophisticated data evaluation techniques allow even for distinguishing between these two molecular species with nearly 100 % certainty, which allows to simultaneously monitoring different molecular species without the necessity of using several excitation and detection channels.
Among others, it is shown how the time-correlated single photon counting capabilities of the system can be used not only for lifetime imaging but also for multi-channel measurements. In particular, intensity, polarization, and lifetime images of single molecules immobilized on surfaces are presented. It is shown how, by using a ring-like laser excitation, three-dimensional polarization measurements of single fluorescent molecules tacked on a glass substrate can be performed. The relation between vertical and parallel electric field component of the exciting laser field can be much increased by this mode of illumination: instead coupling a collimated laser beam into the input aperture of the objective, a ring of light is coupled in by blocking the central part of the laser beam with an opaque aperture. This annular illumination has the effect that mostly light rays with high incidence angle contribute to the excitation light at the focal point, leading to a particularly high relation of vertical to parallel electric field intensity.
The three different electric field orientations show distinct intensity patterns, which can be used to evaluate the three dimensional orientation of a molecule’s excitation dipole. Using

such a pattern recognition approach to the dipole orientation has the advantage that it is much less sensitive to shot-noise variations than directly using the intensity values themselves.

Finally, section 4.5 gives an outlook to in vivo studies in living cells, an application that will certainly gain significant importance in the future. Living human endometrial cancer cells were cultivated on a glass substrate and embedded within a solution containing fluorescently labeled neuropeptides binding to its neuropeptide hNPY Y_5 receptors. Due to their membrane bound diffusion during the time of one image scan these single neuropeptide receptor complexes appear as diffuse bright spots in the intensity image.

6. Bibliography

6.1 Publications

Ruckstuhl, T.; Enderlein, J.; Löscher, F; Böhmer, M; Seeger, S.; " Comparison between a conventional epifluorescence microscope and a new highly efficient evanescent wave detector in single molecule spectroscopic applications" Proceedings of SPIE, Vol. 3602, Advances in Fluorescence Sensing Technology IV, p. 94-101,1999

Böhmer, Martin; Enderlein, Jörg; Seeger, Stefan; " Quantitative Fluorescence Spectroscopy of Single Molecules on Surfaces", Proceedings of SPIE, Vol. 3922, Scanning and Force Microscopies for Biomedical Applications II, 2000

Böhmer, M. and Enderlein, J., "Single molecule detection on surfaces with the confocal laser scanning micorscope", in: *Single-molecule detection in solution: methods and applications*; *Eds.: J. Enderlein, C. Zander, R.A. Keller (VCH-Wiley, 2001) in press*.

Oswald, B.; Arbter, M.; Böhmer, M.; Lehmann, F.; Probst, M.; Wolfbeis, O. S.; " Novel Diode Laser-Compatible Fluorophores, and their Application to Single Molecule Detection, Protein Labelling, and Fluorescence Resonance Energy Transfer Immunoassay", *Photochemistry and Photobiology, Vol. 74, No. 2, p. 237, 2001*

Böhmer, Martin.; Pampaloni, Francesco; Wahl, Michael; Rahn, Hans-Jürgen; Erdmann, Rainer; Enderlein, Jörg; " Time-Resolved Confocal Scanning Device for Ultrasensitive Fluorescence Detection", *Rev. Sci. Inst. Vol. 72(11), pp. 4145-52, November 2001*.

Wolfbeis, Otto. S.; Böhmer, Martin; Dürkop, Axel; Enderlein, Jörg; Gruber, Michaela; Klimant, Ingo; Krause, Christian; Kürner, Jens; Liebsch, Gregor; Lin, Zhihong; Oswald, Bernhard; Wu, Meng; "Advanced Luminescent Labels, Probes, and Beads, and their Application to Luminescence Bioassay and Imaging", *in: New Trends in Fluorescence Spectroscopy: Ed. R. Kraayenhof (Springer Verlag, 2001) in press.*

Böhmer, Martin.; Wahl, Michael; Rahn, Hans-Jürgen; Erdmann, Rainer; Enderlein, Jörg; ”Time-Resolved Fluorescence Correlation Spectroscopy”, *In press: Chem. Phys. Lett.*

Enderlein, Jörg; Böhmer, Martin; ”Calculation of the light collection efficiency function in fluorescence correlation spectroscopy”; *Submitted to J. Opt. Soc. Am. A.*.

Böhmer, Martin; Enderlein, Jörg; ”Ab-initio modeling of fluorescence correlation spectroscopy experiments”; *Submitted to J. Phys. Chem.* A

Böhmer, Martin; Pampaloni, Francesco; *Patent:* “ Compact optical tweezers”,*in preparation.*

6.2 Presentations

Enderlein, J.; Böhmer, M.; Seeger, S.(1999) “ Quantification of single molecule fluorescence on surfaces” *Presentation: Workshop on “Single-molecule Spectroscopy and Molecular Motors” at the Leiden Centre for the Physics and Chemistry of Life Processes, Lozentz Center, Leiden University.*

Enderlein, Jörg; Böhmer, Martin; Seeger, Stefan (1999) “ Quantificative fluorescence detection of single molecules on surfaces”. *I. International Symposium on: “New Trends in Physics, Chemistry, and Biology with Single Molecules”, Wiesbaden, 14-16. July (Germany).*

Böhmer, Martin; Enderlein, Jörg; Seeger, Stefan (2000) “ Quantitative Fluorescence Spectroscopy of Single Molecules on Surfaces”, *International Symposium on Biomedical Optics 2000, Scanning and Force Microscopies for Biomedical Applications II, San Jose, California (USA).*

Böhmer, Martin; Raab, David; Enderlein, Jörg (2000) “ Multiple Analyte Quantification by Combining FCS with TCSPC”. *Presentation: 6th workshop on ”Single Molecule Detection and Ultrasensitive Analysis in Life Sciences”, PicoQuant (Germany).*

Pampaloni, Francesco; Böhmer, Martin; Enderlein, Jörg (2000) “ Monitoring the Brownian Motion of Optically Trapped Microbeads”. *Presentation: 6th workshop on ”Single Molecule Detection and Ultrasensitive Analysis in Life Sciences”, PicoQuant (Germany).*

Wahl, M.; Rahn, H.-J.; Erdmann; R., Böhmer M.; Enderlein, J. (2000) ”Fluorescence Lifetime Imaging with nm-Resolution and Single Molecule Sensitivity”. *Presentation: 6th workshop on ”Single Molecule Detection and Ultrasensitive Analysis in Life Sciences”, PicoQuant (Germany)*.

Erdmann, Rainer, Böhmer, Martin; Wahl, Michael, Enderlein, Jörg (2001) ”Time Resolved Fluorescence Detection of Single Molecules ”. *Invited speaker*: *III. Annual Linz Winter Workshop on: ”Single Molecule Techniques in Biophysics and Drug Discovery”, Linz University (Austria).*

Böhmer, Martin; Raab, David; Pampaloni, Francesco; Enderlein, Jörg (2001) ”Excitation Dipole Orientation and Lifetime Measurements of Single Molecules on Surfaces”. *Presentation: III. Annual Linz Winter Workshop on: ”Single Molecule Techniques in Biophysics and Drug Discovery”, Linz University (Austria).*

Pampaloni, Francesco; Böhmer, Martin; Raab, David; Enderlein, Jörg (2001) ”Photonic Force Microscope with Backscattered Ligth Feedback Control and Simultaneous Fluorescence Detection ”. *Presentation: III. Annual Linz Winter Workshop on: ”Single Molecule Techniques in Biophysics and Drug Discovery”, Linz University (Austria).*

Böhmer, Martin; Raab, David; Pampaloni, Francesco; Enderlein, Jörg (2001) ”Excitation Dipole Orientation of Single Molecules on Surfaces”. *Presentation: II. International Symposium on: ”Physics, Chemistry and Biology with Single Molecules”, Banz (Germany)).*

Böhmer, Martin; Enderlein, Jörg (2001) “ Ab-Initio Modelling of Fluorescence Correlation Spectroscopy”. *Presentation: 7th workshop on ”Single Molecule Detection and Ultrasensitive Analysis in Life Sciences”, PicoQuant (Germany)*.

Mein Dank gilt

Herrn Priv.-Doz. Dr. Jörg Enderlein, für die außerordentlich gute Betreuung der Arbeit und für viele Berechnungen und Analysen, die für die Durchführung der Arbeit unersetzlich gewesen sind. Darüber hinaus bedanke ich mich für viele Anregungen zu Themen des Fachgebietes und die freundschaftliche und kreative Zusammenarbeit auch unter schwierigen äußeren Bedingungen.

Herrn Francesco Pampaloni und Herrn David Raab, für viele anregende Diskussionen und die freundschaftliche Zusammenarbeit, durch die manches Problem aufgeklärt und beseitigt werden konnte und die meinen Laboralltag immer bereichert haben.

Herrn Dr. Michael Wahl, Herrn Dr. Hans-Jürgen Rahn und Herrn Rainer Erdmann, für die sehr gute und stets motivierende Zusammenarbeit bei der Entwicklung von wesentlichen elektronischen Komponenten der Meßapparatur.

Frau Michaela Gruber, Herrn Dr. Bernhard Oswald und Herrn Prof. Dr. Otto S. Wolfbeis, für die praktischen Hinweise bei der Präparation der Proben und die Bereitstellung der neuen diodenlaserkompatiblen Fluoreszenz-Farbstoffe.

Herrn Matthias Mayer, Herrn Dr. Günter Bernhardt und Herrn Prof. Dr. A. Buschhauer, für die Bereitstellung des fluoreszenzmarkierten Neuropeptids und der Zellkulturen.

Ganz besonders möchte ich mich bei Sabse und meiner Tochter Rahel, für das andauernde Verständnis und die liebevolle Unterstützung sowie bei meinen Eltern, Inge und Hans-Dieter Böhmer, bedanken.